

HIGH RESOLUTION TECHNIQUES FOR
QUANTIFYING LATTICE STRAINS IN
POLYCRYSTALLINE SOLIDS DURING
MECHANICAL LOADING USING X-RAY
DIFFRACTION

A Dissertation

Presented to the Faculty of the Graduate School
of Cornell University

in Partial Fulfillment of the Requirements for the Degree of
Doctor of Philosophy

by

Jay Cameron Schuren

May 2011

© 2011 Jay Cameron Schuren

ALL RIGHTS RESERVED

HIGH RESOLUTION TECHNIQUES FOR QUANTIFYING LATTICE
STRAINS IN POLYCRYSTALLINE SOLIDS DURING MECHANICAL
LOADING USING X-RAY DIFFRACTION

Jay Cameron Schuren, Ph.D.

Cornell University 2011

Understanding the conditions that drive phenomena like fatigue crack initiation in polycrystalline samples requires knowledge of the stress state at the crystal scale. Even during uniaxial tensile loading, the stress state at the crystal scale is often complicated due to anisotropic single crystal properties and the arrangement of neighboring grains. Instead of manufacturing specimens on the size scale of the microstructure, diffraction of synchrotron x-rays with *in situ* mechanical loading provides the means to probe the micromechanical response within deforming polycrystals. Measurement of lattice Strain Pole Figures (SPFs) is a robust technique for quantifying the three dimensional micromechanical state within a polycrystalline sample. The focus of this work was to bring the SPF experiment to the level of a measurement capability as opposed to a one-off style experiment. This dissertation is composed of three related studies, each of which is presented as a chapter that can be read independently.

Chapter 1 contains a manuscript which was provisionally accepted for publication in *Experimental Mechanics* [56]. The work investigates the interconnected nature of the SPF coverage and the regions of orientation space probed by each diffraction measurement. The major contribution is a new technique for quantifying how well a set of lattice strain measurements (SPFs) probes each crystal orientation. The orientation space sampling matrix, defined $\mathbf{\Gamma}(\mathbf{R})$, repre-

sents the set of lattice strain measurements that interrogate each crystal orientation. The rank of $\Gamma(\mathbf{R})$ can be used to quantitatively compare different experimental configurations. The net result is a new tool for selecting experimental conditions to produce optimal sets of SPF data.

Chapter 2 is a second manuscript that was provisionally accepted for publication in the Journal of Strain Analysis for Engineering Design [55]. The focus of this effort was the development of an expression for the lattice strain uncertainty that delineates the contributing factors into terms that vary independently: (i) the contribution from the instrument and (ii) the contribution from the material under investigation. The instrument portion of the lattice strain uncertainty is explored and modeled using a calibrant powder method (diffraction from an unstrained material with high precision lattice constants).

Chapter 3 focuses on quantifying the evolution of lattice strains due to cyclic mechanical loading. To interpret the cycle-by-cycle variation in the lattice strains as experimental fluctuations or material evolution a new methodology was developed that combines x-ray diffraction experiments with *in situ* mechanical loading and crystal-based finite element simulations. Merging what can be measured at grain scale with a simulation of the deforming polycrystal provides a robust tool for studying micromechanical behavior. A key finding of the work is that the lattice strain evolution due to cyclic loading occurs rapidly during the earliest portion of the samples fatigue life, and slows as the sample approaches failure.

BIOGRAPHICAL SKETCH

Jay Schuren was born to Peter and Lea Schuren on August 20, 1981 in Leominster, MA. He spent his childhood in Lunenburg, MA and was surrounded by close friends and family. He attended both Ithaca College and Cornell University and received two undergraduate degrees in 2005. He majored in Physics and minored in Mathematics at Ithaca College. He majored in Mechanical Engineering at Cornell University. He began his graduate work at Cornell University in January 2006.

To my family.

ACKNOWLEDGEMENTS

The financial support for this work was provided by the Air Force Office of Scientific Research (AFOSR) under Grant No. FA9550-06-1-0168, Dr. Jaimie Tiley program manager and by Dr. Todd J. Turner of the Materials Directorate, Air Force Research Laboratory (AFRL).

I am extremely grateful for the help and guidance of Matthew Miller, Paul Dawson, and Joel Brock. In particular, the conversations with Matt and Paul have shaped my view of the field of mechanics of materials and helped me plot my career. Your time and effort has been greatly appreciated.

I would also like to thank all of the members of the Deformation Processes Laboratory: in particular Su Leen Wong for her insight and friendship. Jun-Sang Park for his help, both before and after graduating. Donald Boyce for his patience and expertise.

I would like to thank the staff and the scientists at the Cornell High Energy Synchrotron Source. Special thanks to Alexander Kazimirov, Chris Conolly, and Ernie Fontes.

I could not have completed this work without the support of my friends and family. To my friends from Cornell, I could not have hoped for better. Shane and Mike, my oldest friends, I have asked more of you than anyone should. Thanks again. Alyssa and Paul, our conversations have always left me feeling restored - thank you. To my parents, your kindness and work ethic has truly been an inspiration to me. I can't thank you enough.

Tara Simpson, your endless support and patience has been incredible. I owe you so much (0-1). Thank you.

TABLE OF CONTENTS

Biographical Sketch	iii
Dedication	iv
Acknowledgements	v
Table of Contents	vi
List of Tables	viii
List of Figures	ix
1 A Mechanical Testing Capability for Measuring the Microscale Deformation Behavior of Structural Materials	1
1.1 Introduction	1
1.2 Measuring Microscale Material Response in Deforming Polycrystals	3
1.2.1 Methods for Probing Microscale Deformation Behaviors	4
1.2.2 Micromechanical Testing Using High Energy X-ray Diffraction	5
1.2.3 Powder Diffraction Methods	8
1.2.4 The Lattice Strain Pole Figure (SPF) Experiment	10
1.2.5 Crystal Orientations and Fibers Through Orientation Space	13
1.2.6 The Lattice Strain Distribution Function (LSDF)	18
1.3 Measuring SPFs at CHESS Experimental Station A2	19
1.3.1 Material and Specimen Design	20
1.3.2 Experiment Conditions	21
1.4 Orientation Space Sampling	23
1.4.1 The Orientation Space Sampling Matrix, $\Gamma(\mathbf{R})$	26
1.5 SPF Experiment on LSHR	35
1.6 Discussion	36
1.6.1 The Number of Potential Fibers that Probe Each Orientation	39
1.6.2 Limited SPF Coverage	39
1.6.3 The Link Between SPF Data and the LSDF	41
1.7 Summary/Conclusions	42
Acknowledgements	44
2 Quantifying the Uncertainty of Synchrotron-based Lattice Strain Measurements	46
2.1 Introduction	46
2.2 Background	48
2.2.1 The Lattice Strain Pole Figure (SPF) Experiment	49
2.2.2 Diffraction Data	52
2.3 Lattice Strain Uncertainty	57
2.3.1 Instrument Contribution (U_{ells}^i)	59
2.3.2 Model for U_{hkl}^i	72
2.4 Results	75

2.5	Discussion	79
2.6	Summary/Conclusions	83
2.7	Acknowledgments	85
3	Quantifying the Evolution of Crystal Level Stresses Due to Cyclic Loading in AA7075-T6	86
3.1	Introduction	86
3.2	Background	88
3.2.1	Crystal Orientations and Diffraction Measurements	89
3.2.2	Rodrigues Parameterization and the Orientation Distribution Function	91
3.2.3	Lattice Strain Measurements	92
3.2.4	Crystal-based Finite Element Simulation	97
3.3	Measuring/Simulating SPFs for AA7075-T6	99
3.3.1	Material Characterization	100
3.3.2	Diffraction Experiment Details	102
3.3.3	Simulation Details	104
3.3.4	Measured and Simulated SPFs During the Monotonic Response	106
3.4	Lattice Strain Uncertainty	107
3.4.1	Estimating the Uncertainty Contribution from the Instrument, $U_{\text{c ls}}^i$	109
3.4.2	Estimating the Uncertainty Contribution from the Material, $U_{\text{c ls}}^m$, for AA7075-T6	111
3.4.3	Lattice Strain Uncertainty Results	119
3.5	Cyclic Lattice Strain Results	123
3.6	Discussion	128
3.6.1	Cyclic Lattice Strain Evolution	129
3.6.2	Integrating the Experiment and Simulation	130
3.7	Summary /Conclusions	133
3.8	Acknowledgments	135
4	Summary	136

LIST OF TABLES

1.1	Multiplicity values for an FCC material.	26
1.2	SPF experiment configurations investigated.	32
2.1	The experimental conditions used in the two experiments.	60
2.2	The characteristics of the area detectors employed.	60
2.3	Parameters for the distortion correction for the GE 41RT detector published in [40].	67
2.4	The resulting parameters for Equation 3.7 are presented for both experiments.	75
3.1	Multiplicity values for the $\{hkl\}_s$ considered.	117

LIST OF FIGURES

1.1	Two dimensional schematic showing the relationship between the specimen, detector and a single scattering vector, \mathbf{s} . The Bragg angle is $2\theta_{c s}$. At high energies, Bragg's law is satisfied when \mathbf{s} is almost perpendicular to the incoming beam; this corresponds to small $2\theta_{c s}$ angles. The opposite scattering vector, $-\mathbf{s}$, probes the same group of crystals as \mathbf{s} . The laboratory coordinate system is shown.	7
1.2	(a) A typical diffraction pattern for a Low Solvus High Refractory (LSHR) nickel base superalloy with a calibrant powder (CeO_2) applied to the surface of the specimen. Each concentric Debye ring corresponds to diffraction from a particular family of crystallographic planes ($\{hkl\}$ s) from either the LSHR or the CeO_2 . (b) A section of the diffraction spectra corresponding to an azimuthal bin at angle, η . To create a spectrum the intensity is integrated over an azimuthal segment, $\Delta\eta$, from (a). The shift in the $\{200\}$ LSHR peak towards smaller 2θ is consistent with a tensile strain. The $\{220\}$ peak from the calibrant powder is shown on the left and has no change during loading.	11
1.3	The cubic fundamental zone in Rodrigues space parametrized with finite elements. The mesh has 600 independent nodes and is composed of tetrahedral elements. Here the axes indicate the sample loading direction (LD), transverse direction (TD), and normal direction (ND).	16
1.4	The $\{111\} LD$, $\{200\} LD$, $\{220\} LD$, and $\{311\} LD$ fibers, going left to right are plotted in the fundamental zone.	17
1.5	Schematic showing the relevant components in the x-ray beam path at CHESS A2 for the SPF experiment.	22
1.6	Loadframe/diffractometer employed for the SPFs experiments depicting the relevant components.	23
1.7	(a) Results from three different diffraction patterns are shown on both the SPFs and in the fundamental zone. The results correspond to the $\{111\}$, $\{200\}$, $\{220\}$, and $\{311\}$ going left to right. The shading varies from gray to black along a single band to allow for identification of each point. The fibers shown in (b), (c) and (d) are each from a single band of data indicated in (a). . . .	25
1.8	SPF coverage for the experiment configurations described in Table 1.2. For configurations 2 to 5 the measurement positions on the SPF correspond to the $\{111\}$. The measurement positions for the remaining $\{hkl\}$ s differ from the $\{111\}$ by less than a few degrees.	33

1.9	The number of unique fibers that pass through each orientation for the configurations described in Table 1.2 are shown in the fundamental zone. The top row shows the outer surface of the fundamental zone and the bottom row shows three interior orthogonal plane sections of the same region. The upper limit for the $\{hkl\}_s$ measured is 25 fibers per orientation. Due to incomplete SPF coverage for the different configurations the most fibers to pass through a single orientation is 17 for (5).	34
1.10	The rank of the orientation space sampling matrix over orientation space for each of the configurations described in Table 1.2. By moving from (1) to (5) the inversion problem becomes over constrained.	34
1.11	(a) Macroscopic engineering stress vs. engineering strain curve for the LSHR in the as forged state. (b) Stress and strain plotted vs. time for the LSHR specimen. To mitigate creep effects the load is decreased to 90% during the diffraction measurements. During the periods where the load is held constant, the sample is rotated to allow additional unique scattering vectors to be measured. For scale our load hold period is approximately an hour using the MAR345 area detector.	36
1.12	SPFs for $\{111\}$, $\{200\}$, $\{220\}$, and $\{311\}$ going left to right. Top to bottom corresponds to the SPFs measured at a macroscopic stress of (a) 225 MPa, (b) 450 MPa, and (c) 720 MPa in tension. . .	37
2.1	Schematic of a diffraction experiment experiment conducted in transmission. Here D and ρ are the sample to detector distance and the radial distance on the detector, respectively.	49
2.2	The $\{200\}$ lattice SPF measured at a uniaxial macroscopic stress of 720 MPa for a nickel-based superalloy - Low Solvus High Refractory (LSHR). The coordinate system is relative to the sample and the directions are the Loading Direction (LD), the Transverse Direction (TD), and the Normal Direction (ND) [56].	51
2.3	Schematic of the components that make up the x-ray beam path for the experiment conducted at CHESS. The monochromator isolates a single x-ray energy to within 50 eV, the slits define the cross section of the incoming x-ray beams, and the flight chamber and the collimator are used to minimize the scatter from sources other than the sample. The experiment conducted at the APS employed a similar arrangement of components along the x-ray beam path.	51

2.4	(a) Typical diffraction pattern measured with the MAR345 area detector at CHESS for an aluminum sample with a CeO ₂ calibrant insert fixed to the sample. (b) The array of radial positions versus intensities for the highlighted azimuthal bin in (a). A region of the array is selected to indicate the similar characteristics of the calibrant and aluminum peaks.	53
2.5	(a) Schematic of an area detector with four radial and eighteen azimuthal bins overlaid. (b) Two triangular elements defined by four pixels. The intensity value at any point 'A' within the element can be calculated using the neighboring nodal point values and the linear interpolation functions.	55
2.6	Schematic of a grid of square pixels is shown with a single azimuthal bin defined with triangular elements overlaid.	55
2.7	CeO ₂ lattice strain distributions are shown for each $\{hkl\}$ for the experiment conducted at CHESS. Though each measurement pertains to a specific $c s$ combination, to investigate the instrument portion of the uncertainty data for each $\{hkl\}$ are grouped together.	61
2.8	CeO ₂ lattice strain distributions are shown for each $\{hkl\}$ for the experiment conducted at the APS.	62
2.9	The measured lattice strain uncertainty for each CeO ₂ $\{hkl\}$ are shown for the experiments conducted at (a) CHESS and the (b) APS. Each data point corresponds to the $\{hkl\}$ indicated at the top of the figure.	64
2.10	The minimum resolvable lattice strain for three $\delta\rho_{min}$ values show a characteristic decline in the minimum lattice strain value with increasing 2θ values.	69
2.11	(a) The radial peak position of four aluminum $\{hkl\}$ s are shown for varying x-ray energies at a fixed sample to detector distance of 650 mm. (b) The minimum lattice strain for $\delta\rho_{min} = 3.5\mu m$ is shown to increase with increasing x-ray energy for the radial positions in (a).	70
2.12	(a) For a fixed x-ray energy the radial positional of the diffracted peaks increases linearly with the sample to detector distance. (b) The minimum resolvable lattice strains are shown for a peak shift of $\delta\rho_{min} = 3.5\mu m$	71
2.13	The measured uncertainty and the average intensity scaling factor for each CeO ₂ $\{hkl\}$ is show for both the (a) CHESS and the (b) APS experiment. The difference in the magnitude of the measured intensities between the detectors is due to the difference in maximum allowable intensity values.	74

2.14	The calculated lattice strain uncertainties are shown overlaid on the measured values for both the (a) CHESS and the (b) APS experiments. Each component of the uncertainty from Equation 2.19 is also shown independently.	76
2.15	(a) The (a) U_{hkl}^i and (b) intensity values are shown for two measurements made in succession with different exposure times shows using the CHESS experimental configuration. As expected, the uncertainty increases as the intensity decreases. . . .	77
2.16	The change in the pattern center position is shown with increasing time by the data points ranging from black (first image) to gray for both the (a) CHESS and the (b) APS experiments.	78
3.1	Schematic of the relevant length scales for studying elastoplastic deformation in polycrystalline alloys.	89
3.2	The transmission diffraction geometry is shown. Here D is the distance between sample and the area detector and ρ is the radial position of the diffracted x-ray on the detector.	91
3.3	(a) One quarter of the surface of an area detector displaying a typical diffraction pattern for the AA7075-T6 sample with a 5° azimuthal bin ($\Delta\eta$) indicated. (b) Spectrum for the highlighted bin with the same aluminum peaks indicated.	95
3.4	EBSD data for AA7075-T6 are shown for the plane defined by the sheet rolling direction (L) and the long transverse direction (LT). An arbitrary color is overlaid for each grain.	101
3.5	The ODF for the AA7075-T6 calculated from the diffraction data using MAUD [44]. The colorbar is in Multiples of a Uniform Distribution (MUD)	101
3.6	Experiment and simulation macroscopic stress-strain curves are shown for the monotonic portion of the deformation. The points indicate where the SPFs were measured. The circled points indicate the stress levels associated with the SPFs shown in Figure 3.9, Figure 3.10, Figure 3.11, and Figure 3.12.	102
3.7	The loadframe/diffractometer is shown with key components labeled [57].	103
3.8	The relationship between the specimen and the virtual specimen is shown schematically. The color of the grains making up the virtual specimen corresponds to the orientation. The x-ray beam size of $0.5\text{mm} \times 0.5\text{mm}$ is also indicated.	105
3.9	The measured (exp.) and the simulated (sim.) SPFs are shown at 0 MPa. The simulation assumes the initial lattice strains to be zero.	107
3.10	(a) The measured and the simulated SPFs at 135 MPa. The difference is shown in (b).	108
3.11	(a) The measured and the simulated SPFs at 400 MPa. The difference is provided in (b)	109

3.12	(a) The measured and the simulated SPFs at 515 MPa. (b) The difference is more pronounced than in the previous SPFS.	110
3.13	The relationship between a patch on the {200} SPF and the corresponding region of orientation space interrogated is shown for (a) a point aligned with LD, (b) a $0.3^\circ \times 15^\circ$ patch centered about LD, and a $5^\circ \times 5^\circ$ patch centered about LD.	115
3.14	The scattering vectors for the AA7075-T6 {111} lattice strain measurements due to rocking by (a) $\omega = \pm 10^\circ, \chi = 0^\circ$, (b) $\omega = 0^\circ, \chi = \pm 10^\circ$, and (c) the result of rocking by (a) and (b) in series.	116
3.15	(a) The probable number of grains that contribute to each measurement and (b) the number of elements contributing to each simulated lattice strain are shown for each {hkl}.	118
3.16	The standard deviation of the simulated lattice strains are shown at (a) 0 MPa, (b) 135 MPa, (c) 400 MPa, and (d) 515 MPa.	120
3.17	(a) The experimental lattice strain uncertainty is plotted for each measurement. The region with the highest uncertainty occurs on the {200} SPF below TD. (b) The lattice strain uncertainty for the simulated results was determined using Equation 3.9.	122
3.18	(a) The mean of the measured lattice strains at 515MPa within a 5° radius circle about each glyph. (b) The number of measurements included in each grouping is shown. (c) The uncertainties for the mean lattice strain results are shown for the same points presented in (a) and (b).	124
3.19	The macroscopic stress-strain curve for the AA7075-T6 sample. The sample was cycled between 0 and 572 MPa. The sample failed after 1588 cycles.	125
3.20	The cyclic lattice strains for each {hkl} are shown as a difference between the cycle of interest and cycle zero at 515 MPa. The difference SPFs are shown for cycles 1-0, 10-0, and 100-0, respectively.	126
3.21	The cyclic lattice strains in Figure 3.20 are presented after grouping the results within 5° regions. The grouped difference SPFs are shown for 1-0, 10-0, and 100-0, respectively.	127
3.22	The SPF RMS is shown with increasing cycles. The sample failed after 1588 cycles. The insert shows the SPF RMS for the first 100 cycles.	128

CHAPTER 1
A MECHANICAL TESTING CAPABILITY FOR MEASURING THE
MICROSCALE DEFORMATION BEHAVIOR OF STRUCTURAL
MATERIALS

1.1 Introduction

Mechanical testing - broadly defined as measuring the response of an engineering material subjected to external loads - has evolved immensely over the past several decades. Some of the obvious advances – including computer-driven digital machine controllers, innovative multiaxial load actuation and complex control of specimen temperature and environment – have produced unprecedented improvements in our understanding of engineering material behavior under some of the most demanding service and processing conditions imaginable. Mechanical testing's most important contribution to mechanical design has been the production of validation and calibration data for high fidelity material models. The most useful interaction between experiments and simulations occurs when the resolution, accuracy and precision of both simulated and experimental data are well understood. So, while scientific excitement and an innate drive towards discovery are crucial for the creation of a new experimental measurement, the important work of creating a mechanical testing **capability** - which consists of establishing resolution, accuracy and a standardization of best practices - begins *after* that first measurement is made. This paper describes such a standardization process for an important new micromechanical testing methodology.

In the lattice Strain Pole Figure (SPF) experiment, *in situ* loading and high

energy x-ray diffraction are used to monitor the distortion of crystals within a deforming polycrystalline aggregate [5, 6, 48, 51]. The loaded specimen is re-oriented relative to the x-ray beam so that every crystal within the diffraction volume is interrogated. Using a methodology motivated by quantitative texture analysis [2, 7] the lattice strain tensor (elastic) at each crystal orientation - referred to here as the Lattice Strain Distribution Function (LSDF) can be quantified from the SPF data [4]. The single crystal elastic moduli can then be employed to produce the full stress tensor at each orientation within the aggregate [3, 4, 49, 66]. Previous efforts have shown that there are appreciable variations in the average stress tensor for different crystallographic orientations within a polycrystal even when subjected to simple uniaxial tension [5, 49].

The SPF experiment utilizes components that are common to every mechanical testing laboratory. The loads are applied with an actuator and a conventional load cell and strain gages are used to monitor the macroscopic deformation behavior of the specimen. Other aspects of the SPF experiment are less familiar to the experimental mechanics community. As described in detail in the other publications listed above as well as in later sections of this paper, the lattice strains themselves - which are similar to the normal strains indicated by a resistance strain gage during elastic deformation - are manifest as shifts in diffraction peaks. The goal of the SPF experiment is to quantify the crystal scale mechanical response. In terms of establishing a standard set of experimental practices that will produce “optimal” sets of SPF data, therefore, a few basic questions must be addressed. (i) To what extent do diffraction measurements made during an SPF micromechanical experiment probe each crystal orientation? (ii) Can the selection of diffraction measurements be optimized to interrogate **all** orientations within the aggregate?

By carefully addressing these two questions, the SPF experiment can be elevated from the status of a one-off experiment or “heroic effort” to a true measurement **capability** with a comprehensive metric for quantifying how well each crystallographic orientation is interrogated. In the following sections we present a brief overview of the classes of mechanical tests that explicitly probe the micromechanical material response of polycrystalline samples. We quickly move to an overview of high energy x-ray diffraction methods. We describe in detail our method for measuring lattice SPF data – along with a careful description of our specimen loading/orientation system or diffractometer, which resides within the A2 experimental station of the Cornell High Energy Synchrotron Source (CHESS). The overview focuses on characterization of micromechanical material response – with a specific emphasis on the role of diffraction experiments. We then describe the SPF experimental setup at CHESS including short primers on high energy x-ray diffraction and a description of crystal orientations. Using SPF measurements on Low Solvus High Refractory (LSHR) nickel base superalloy, we introduce the rank of the orientation space sampling matrix, $\Gamma(\mathbf{R})$, as a means to quantify the influence of each diffraction measurement – with particular emphasis on the role of pole figure coverage and the lattice planes measured in sampling orientation space.

1.2 Measuring Microscale Material Response in Deforming Polycrystals

Within the field of mechanics of materials there is an expanding need for experiments designed to probe the mechanical response of a polycrystalline aggregate

at the size scale of individual grains (crystals). Microscale stress-strain data are creating new understanding of grain scale deformation processes and driving new discoveries on their own right. However, the need for reliable crystal scale data has been driven in large part by the down-scale migration of mechanical design and analysis. Validation and calibration of microscale material models cannot be reliably accomplished with macroscopic data - there are many ways to mistakenly “predict” macroscopic stress-strain data using microscale state variables. Understanding the material response at the grain scale enables an understanding of the boundary value problem that drives important processes such as microplasticity and fatigue crack initiation. Micromechanical testing methods, which utilize *in situ* mechanical loading, provide critical insight into the complicated relationship between orientation-dependent single crystal properties and the material response at the grain and subgrain level within a deforming polycrystal.

1.2.1 Methods for Probing Microscale Deformation Behaviors

There are two basic methods for probing material behavior at the scale of the individual grain within a polycrystal.

- (i) The first involves extracting miniature grain scale test samples, which are deformed using microscale loading machines [31, 33, 59, 62]. The predominance of these efforts investigate the influence of sample dimensions on the mechanical properties, often in concert with the formation and propagation of dislocations [58, 61]. Theoretically, grain scale properties can be extracted from such experiments under closely controlled loading condi-

tions. Using post-mortem microstructural interrogation techniques such as Transmission Electron Microscopy (TEM), indirect connections can be made to dislocation processes. An example of such an experiment that allows for real time observation of dislocation nucleation and motion is the work of Robertson [54]. The advantage of this experiment is the ability to monitor structure evolution *in situ* .

- (ii) The second category of micromechanical tests employs standard size specimens but uses diffraction of high energy x-rays or neutrons to observe changes in the crystalline structure of engineering alloys at the grain scale during *in situ* loading conditions [12, 15, 23, 45, 48, 52, 67]. This is the class of experiments described in this paper. These tests provide a direct link between the forces and strains measured at the macroscale and relevant structure evolution, which is quantified in real time using x-rays. We begin by describing the various types of high energy x-ray diffraction experiments below.

1.2.2 Micromechanical Testing Using High Energy X-ray Diffraction

The general approach for these experiments is to load the specimen to a prescribed macroscopic stress level then measure the strain pole figures. Upon completion of the diffraction measurements the load is increased; or in a related experiment, additional cycles are applied. Then the load is stabilized and the diffraction procedure is repeated. The object of these experiments is to understand the way stress is redistributed within the aggregate as the specimen state

is evolved by either the addition of increased tensile stress or by the addition of loading cycles. Advancements in x-ray detector technologies combined with the penetration power of synchrotron x-rays and *in situ* loading have produced a set of high energy x-ray diffraction capabilities that are unparalleled and prove to be an incredible resource for high fidelity diffraction experiments on bulk samples. Use of area detectors and the immense brilliance at current synchrotron facilities lead to the rapid completion of diffraction measurements.

There are three relevant coordinate systems for diffraction experiments. The coordinate systems are defined relative to the laboratory frame, the sample frame, and the crystal frame. The schematic shown in Figure 1.1 depicts the transmission diffraction geometry highlighting the relationship between the incoming x-rays, the sample, the diffracted beam of x-rays, and the detector. The scattering vector, \mathbf{s} , bisects the incoming and diffracted beam of x-rays. Each scattering vector is normal to the family of crystallographic planes ($\{hkl\}$) that satisfy Bragg's Law:

$$n\lambda = 2d_{\mathbf{c}||\mathbf{s}} \sin \theta_{\mathbf{c}||\mathbf{s}} \quad (1.1)$$

Here n is an integer, λ is the x-ray wavelength, $d_{\mathbf{c}||\mathbf{s}}$ is the lattice spacing, and $2\theta_{\mathbf{c}||\mathbf{s}}$ is the angle between the transmitted and the diffracted beams [17]. The subscript $\mathbf{c}||\mathbf{s}$ indicates each diffraction measurement by the normal to the family of crystallographic planes in the crystal frame, \mathbf{c} , which is parallel to the scattering vector, \mathbf{s} . The centroid of the diffracted intensity distribution represents the average crystallographic plane spacing from crystals satisfying Bragg's law. As the sample is loaded, the lattice plane spacing changes. This loading-induced change is manifest as a change in the Bragg angle, $2\theta_{\mathbf{c}||\mathbf{s}}$, which enables the crystal lattice itself to act literally as an 'elastic strain gage'. For an individual crystal within the aggregate, diffraction measurements of lattice strains

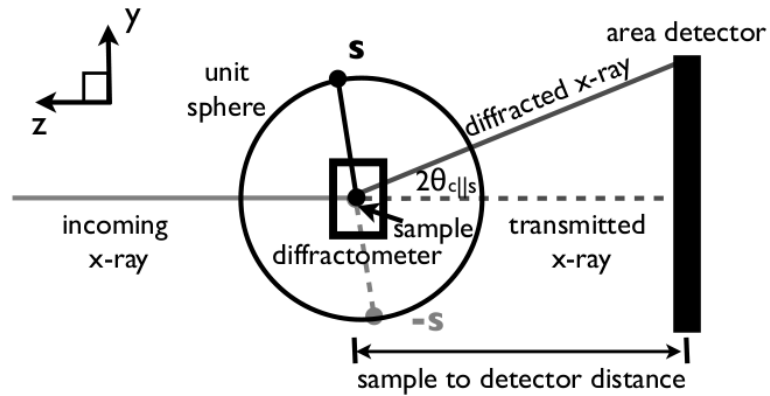


Figure 1.1: Two dimensional schematic showing the relationship between the specimen, detector and a single scattering vector, s . The Bragg angle is $2\theta_{c||s}$. At high energies, Bragg's law is satisfied when s is almost perpendicular to the incoming beam; this corresponds to small $2\theta_{c||s}$ angles. The opposite scattering vector, $-s$, probes the same group of crystals as s . The laboratory coordinate system is shown.

represent the projection of the elastic strain tensor in the direction of the scattering vector, s . With a sufficient number of measurements in different directions, similar to using a strain gage rosette, the elastic strain tensor for the crystal can be obtained. Significant advances have been made in the area of individual crystal lattice strain measurement during *in situ* loading including the pioneering 3DXRD work done by Risoe at the European Synchrotron Research Facility (ESRF) [45, 52] and the High Energy Diffraction Microscopy (HEDM) suite of experiments developed at the Advanced Photon Source (APS) beamline 1-ID-C [1, 26, 41, 42]. Obtaining strain information from enough individual crystals to approach statistical significance however, is problematic. The lattice Strain Pole Figure (SPF) method is an alternative that sacrifices grain-by-grain spatial correlation but utilizes aggregate or powder data to determine the *most likely* strain tensor for each crystal orientation.

1.2.3 Powder Diffraction Methods

Instead of measuring crystal-by-crystal lattice strains as is done in the 3DXRD or HEDM methods, powder diffraction methods for lattice strains yield distributions of strain behavior based on crystal orientation - similar to the Orientation Distribution Function (ODF) from Quantitative Texture Analysis (QTA) [11, 37, 68]. Instead of spots, ideal powder diffraction data are complete Debye rings. Robust powder diffraction techniques can be applied to determine average lattice strains for groups of crystals that satisfy Equation 1.1 [5, 6, 48]. The goal of the powder experiment for lattice strain is to understand the orientation dependent deformation behavior within a “material point” in the sample. In addition to directly investigating the material response, these experiments produce much needed micromechanical data for corroboration with crystal-based constitutive models [13, 19, 49]. Through comparing the average lattice strain values for groups of crystals that satisfy the diffraction condition (Bragg’s Law in Equation 1.1) in both the experiment and the simulation, the micromechanical response can be investigated to develop a deeper understanding of the material behavior [53, 70].

With the analogy between a peak shift and a normal strain obtained with a resistance type strain gage, rotation of the sample with respect to the x-ray corresponds to placing gages in multiple orientations. The positioning equipment used in these experiments (diffractometer) is integral in the measurement of lattice strains in polycrystalline alloys. Each reorientation allows for different subsets of crystals, with different orientations, to be interrogated - producing additional unique lattice strain measurements. These measurements can be depicted on lattice Strain Pole Figures (SPFs), which are analogous to traditional

orientation pole figures, however with normal strain values plotted rather than pole densities [48]. Following the approach of QTA, we utilize several SPFs (which are basically two dimensional strain projections) to obtain the average lattice (elastic) strain tensor for each crystallographic orientation, referred to as the Lattice Strain Distribution Function (LSDF) [3, 4, 65, 66]. As in QTA, this process is referred to as pole figure inversion and different lattice strain inversion techniques have been used [4, 65]. Once the LSDF, $\underline{\epsilon}(\mathbf{R})$, is obtained, the stress as a function of crystallographic orientation, $\underline{\sigma}(\mathbf{R})$, can be determined through Hooke's law and the single crystal elastic moduli. For the case of limited measurements several constraint conditions, such as a self consistent stress field [66] or a smoothing constraint on the strain and dilation fields over orientation space [4], have been imposed to make the problem tractable.

Due to anisotropic single crystal properties and the inherent inhomogeneity of the deformation at the crystal scale, the stress state at each orientation will not be equivalent to the applied macroscopic stress [60]. The average stress for each orientation can be compared with simulations directly or through a spherical harmonic decomposition [49]. Through such rigorous comparisons, confidence in both the experiments and simulations is gained; providing a new framework to investigate phenomena like fatigue due to cyclic loading. One of the most consistent results that have been obtained from both the single crystal experiments as well as the powder tests, is the variation in stress state that exists within the deforming aggregate [41, 49]

The ability to obtain the average elastic strain tensor for all possible crystal orientations from diffraction data is governed by the number and direction of the lattice strain measurements and the method used to reconstruct the LSDF

from these projections. The relative weight of each measurement is coupled to the set of orientations interrogated and the direction of the measurement in a manner similar to selecting the number and direction of strain gages applied to a sample. As will be developed in later sections, the set of lattice strain measurements that probe each orientation can be represented by the orientation space sampling matrix, $\mathbf{\Gamma}(\mathbf{R})$. The major contribution of this paper is the development of a new metric, the rank of $\mathbf{\Gamma}(\mathbf{R})$, for quantifying how well a set of diffraction measurements probe the micromechanical state.

1.2.4 The Lattice Strain Pole Figure (SPF) Experiment

Building an SPF begins with Bragg's Law as depicted in Equation 1.1. The diffracted intensity from a typical polycrystalline sample (powder) is presented in Figure 1.2(a). Each ring in the pattern is due to diffraction from a specific family of crystallographic planes. Rings closer to the center of the detector have smaller Bragg angles or, as indicated by Equation 1.1, larger average lattice plane spacing, $d_{\mathbf{c}||\mathbf{s}}$. During a monochromatic diffraction experiment (fixed λ), only a subset of crystals within the irradiated volume satisfies the Bragg condition for a particular $\mathbf{c}||\mathbf{s}$ combination. These crystals are typically distributed throughout the irradiated volume, but share the same orientation to within an arbitrary rotation about the scattering vector, \mathbf{s} . Due to anisotropy of the single crystal properties, and variations in the orientation of neighboring grains, each of the participating crystals may experience different boundary conditions and a complicated local stress state [30].

The overlay of the reference diffraction pattern (initial state) and a strained

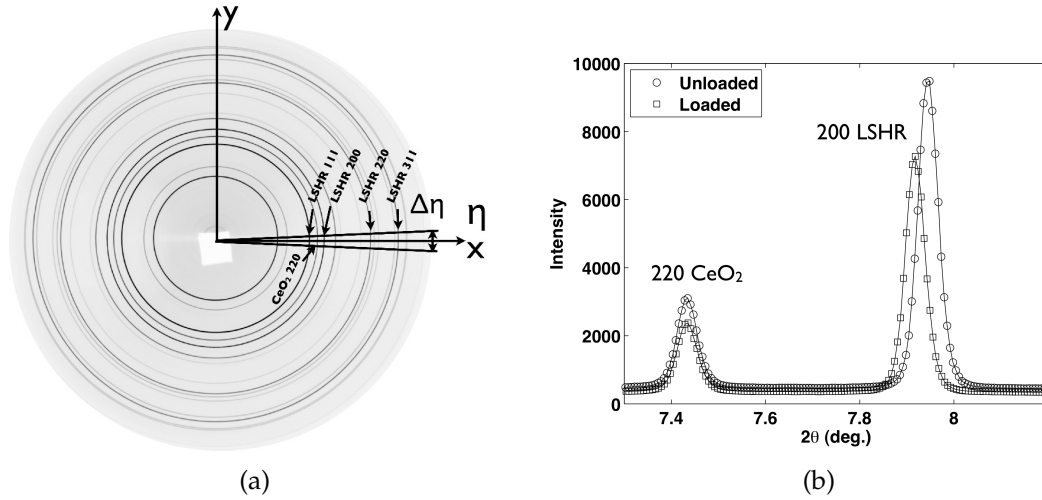


Figure 1.2: (a) A typical diffraction pattern for a Low Solvus High Refractory (LSHR) nickel base superalloy with a calibrant powder (CeO_2) applied to the surface of the specimen. Each concentric Debye ring corresponds to diffraction from a particular family of crystallographic planes ($\{hkl\}$ s) from either the LSHR or the CeO_2 . (b) A section of the diffraction spectra corresponding to an azimuthal bin at angle, η . To create a spectrum the intensity is integrated over an azimuthal segment, $\Delta\eta$, from (a). The shift in the $\{200\}$ LSHR peak towards smaller 2θ is consistent with a tensile strain. The $\{220\}$ peak from the calibrant powder is shown on the left and has no change during loading.

diffraction pattern for a portion of the same azimuthal bin ($\Delta\eta$) is shown in Figure 1.2(b), highlighting the shift of the LSHR $\{200\}$ peak. Shift in the peaks create distortions of the Debye rings shown in Figure 1.2(a). At a point in the deformation history, each peak shift corresponds to a particular $c\|s$ combination. The stationary peak in Figure 1.2(b) is from an unstrained cerium dioxide (CeO_2) calibrant powder. The calibrant powder is used to verify instrument parameters such as the sample to detector distance, the pattern center, and the detector tilts [5, 48]. More specific information on the reduction of diffraction data for the SPF experiment appears in [5]. By changing the sample orientation, normal strain

measurements at different crystal orientations can be made for each new $\mathbf{c}||\mathbf{s}$. To build an SPF, the strain for a particular $\{hkl\}$ is plotted at the intersection of the scattering vector and a reference sphere. This sphere represents the pole figure surface and a point on the sphere is defined relative to the sample coordinate system. Rotation of the sample using the diffractometer, labeled in Figure 1.1, allows more unique measurements to be obtained. A detailed description of basic SPF determination from loaded samples can be found in [48]. Once the lattice spacing in the loaded state is determined, the calculation of lattice strain is analogous to conventional engineering strain:

$$\epsilon_{\mathbf{c}||\mathbf{s}} = \frac{d_{\mathbf{c}||\mathbf{s}} - d_{\mathbf{c}||\mathbf{s}}^0}{d_{\mathbf{c}||\mathbf{s}}^0} \quad (1.2)$$

where $\epsilon_{\mathbf{c}||\mathbf{s}}$ is the normal strain for the particular $\mathbf{c}||\mathbf{s}$ combination and $d_{\mathbf{c}||\mathbf{s}}^0$ is the reference plane spacing. Due to the typically small magnitude of lattice strains in metallic alloys, the use of a simple engineering strain as defined in Equation 1.2 is satisfactory. If large elastic strains and rotations are anticipated a finite strain formulation describing the distortion of the unit cell might be warranted.

There are two common methods for defining the initial plane spacing $d_{\mathbf{c}||\mathbf{s}}^0$. First, if the material has well characterized lattice parameters, they can be used to unequivocally calculate $d_{\mathbf{c}||\mathbf{s}}^0$. This approach produces a single reference spacing for each $\{hkl\}$ that is unchanged by the measurement direction. Using this definition, the residual lattice strain in the material can be determined by comparing to the measured peak positions at zero macroscopic load. The second method merely employs the plane spacing at zero load for each scattering vector. This method is independent of any prior knowledge of the lattice parameters and, as such, is insensitive to residual lattice strains in the material. For a sample with no residual lattice strain, the two methods would obviously produce equivalent results.

1.2.5 Crystal Orientations and Fibers Through Orientation Space

There are many methods for describing the orientation of a single crystal relative to a fixed sample coordinate system. One of the most intuitive methods is to represent a crystal orientation by the rotation matrix, \mathbf{R} , that maps a vector from the crystal coordinate system to the sample coordinate system, $\mathbf{v}_{sam} = \mathbf{R}\mathbf{v}_{crys}$. Here both \mathbf{v}_{sam} and \mathbf{v}_{crys} are defined in Cartesian coordinate systems with orthonormal basis vectors. As described in Figure 1.1, diffraction occurs when the normal of a candidate set of crystallographic planes defined in the crystal coordinate system, \mathbf{c} , is parallel to the scattering vector, \mathbf{s} , which is written in the sample coordinate system. The crystal orientations, therefore, that satisfy these conditions are defined by:

$$\mathbf{R}\mathbf{c} = \pm\mathbf{s} \quad \forall\mathbf{R} \quad (1.3)$$

The subset of orientations that diffract are unchanged by the sign of the measurement direction and result in antipodal symmetry on the SPFs.

The scattering vector is defined by the unit vector $\mathbf{s} = [u \ v \ w]$. The basis vectors for the sample coordinate system are defined relative to the flat tensile sample as the loading direction (LD), the long dimension in the cross-section, referred to as the transverse direction (TD), and the short transverse or normal direction (ND). The sample and laboratory coordinate systems are aligned when ND is aligned with incoming x-ray and TD is aligned with the vertical direction (labeled y in Figure 1.1) in the laboratory frame.

The relationship between the basis vectors for the crystal coordinate system

and the Miller indices ($\{hkl\}$) is more complicated. The basis vectors for the crystal frame are referred to as lattice vectors ($\mathbf{a}_1, \mathbf{a}_2, \mathbf{a}_3$) and are selected to represent the periodicity of the lattice. The lattice vectors are said to be primitive when the unit cell defined by the lattice vectors has the minimum possible volume. For the common cubic metallic systems, face centered cubic (FCC) and body centered cubic (BCC), it is conventional to forgo the use of the primitive lattice vectors and to define the crystal basis vectors to be aligned with the $\{100\}$ cube plane normals. For cubic materials, therefore, $\mathbf{c} = \frac{1}{\sqrt{h^2+k^2+l^2}}[h \ k \ l]$ where $h, k,$ and l are the Miller indices $\{hkl\}$. The definition of \mathbf{c} for a general crystal structure requires a change of the basis vectors to an orthonormal set for use in Equation 1.3. This change of basis vectors is simplified by the use of the reciprocal lattice. Each point in the reciprocal lattice represents an $\{hkl\}$ and is commonly used to describe diffraction. An introduction to the reciprocal lattice can be found in [35], but a brief overview will be provided here.

The basis vectors for the reciprocal lattice are defined relative to the lattice vectors, \mathbf{a}_i , as:

$$\mathbf{b}_1 = 2\pi \frac{\mathbf{a}_2 \times \mathbf{a}_3}{\mathbf{a}_1 \cdot (\mathbf{a}_2 \times \mathbf{a}_3)} \quad (1.4)$$

$$\mathbf{b}_2 = 2\pi \frac{\mathbf{a}_3 \times \mathbf{a}_1}{\mathbf{a}_1 \cdot (\mathbf{a}_2 \times \mathbf{a}_3)} \quad (1.5)$$

$$\mathbf{b}_3 = 2\pi \frac{\mathbf{a}_1 \times \mathbf{a}_2}{\mathbf{a}_1 \cdot (\mathbf{a}_2 \times \mathbf{a}_3)} \quad (1.6)$$

A vector that is normal to the set of diffracting planes is defined in reciprocal space by [35]:

$$\mathbf{G} = h\mathbf{b}_1 + k\mathbf{b}_2 + l\mathbf{b}_3 \quad (1.7)$$

Using the reciprocal lattice we map each $\{hkl\}$ to an orthonormal set of basis vectors and normalize \mathbf{G} to define the relevant crystal direction for use in Equ-

tion 1.3:

$$\mathbf{c} = \frac{\mathbf{G}}{\|\mathbf{G}\|} \quad (1.8)$$

In addition to the rotation matrix \mathbf{R} , there are a number of ways to parameterize orientations. Perhaps the most useful for computing within orientation space and for graphical depiction is the Rodrigues parameterization [27]. The direction of a Rodrigues orientation vector from the origin of the space defines a rotation axis, and the magnitude of the vector is related to the rotation angle:

$$\mathbf{r} = \mathbf{n} \tan\left(\frac{\phi}{2}\right) \quad (1.9)$$

where \mathbf{n} is the axis of rotation and ϕ is the angle of rotation about the axis [27, 39, 50]. The relationship between the Rodrigues vector and the orientation matrix \mathbf{R} is:

$$\mathbf{R} = \frac{\mathbf{1}}{\mathbf{1} + \mathbf{r} \cdot \mathbf{r}} (\mathbf{I}(\mathbf{1} - \mathbf{r} \cdot \mathbf{r}) + 2(\mathbf{r} \otimes \mathbf{r} + \mathbf{I} \times \mathbf{r})) \quad (1.10)$$

where \mathbf{I} is the identity tensor, and \cdot , \otimes , and $\mathbf{I} \times \mathbf{r}$ indicates the dot product, the dyad, and the skew tensor from \mathbf{r} , respectively [39, 50].

A single diffraction measurement corresponds to a point on the detector and, as described previously, is defined by both a crystal and sample direction. The orientations participating in a single diffraction measurement share a common plane normal and form a straight line in Rodrigues space. This line is known as a crystallographic **fiber**. When crystal symmetries are accounted for, the space comprised of all possible Rodrigues vectors is bounded for many crystal types, and referred to as the fundamental zone [27, 32, 39]. Any segment of a fiber that extends beyond the boundary of the fundamental zone can be remapped back to

an equivalent location within the fundamental zone resulting in the fiber being broken into many segments constituting the set of crystal orientations represented by a rotation of 2π about the scattering vector. For an introduction to Rodrigues space and calculations over the fundamental zone, the authors recommend [2, 27, 32, 39]. The fundamental zone for a cubic material is shown in Figure 1.3 with a finite element mesh overlaid [39]. Any point in the fundamental zone specifies a crystal rotation with respect to the sample axes shown. The point in the center of the region corresponds to the identity matrix (no rotation). The FEM discretization of the fundamental zone, first introduced in [39], allows us to fully represent field quantities in Rodrigues space such as the ODF and the lattice strain distribution function defined in the next section. More on the fundamental zone for crystal symmetries other than cubic can be found in [32].

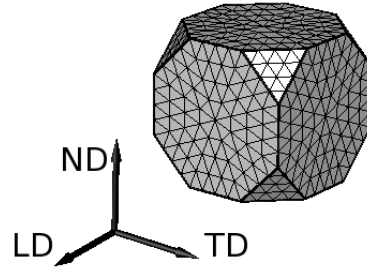


Figure 1.3: The cubic fundamental zone in Rodrigues space parametrized with finite elements. The mesh has 600 independent nodes and is composed of tetrahedral elements. Here the axes indicate the sample loading direction (LD), transverse direction (TD), and normal direction (ND).

As discussed, each lattice strain measurement is the average normal strain from all the crystal orientations satisfying the diffraction condition. To design a diffraction experiment that fully probes orientation space, and to understand the regions of orientation space probed by each measurement, let us first consider the results from the azimuthal bin highlighted in Figure 1.2(a). The scat-

tering vectors associated with each $\{hkl\}$ in the η bin shown in Figure 1.2(a) are nominally in the sample loading direction - differing between the $\{111\}$ and the $\{311\}$ by only 3° (for $\lambda = 0.2480 \text{ \AA}$). However, due to the differences in the crystal directions, the fibers associated each $\{hkl\}$ are significantly different. These fibers are shown in Figure 1.4. Recall from Equation 1.3, these are the crystallographic orientations that can contribute intensity for each $\{hkl\}$ for a scattering vector near LD. With the exception of the $\{200\}||\text{LD}$ fiber, the configuration of these lines in orientation space are not especially intuitive. The striking differences between the fibers are due to the cubic symmetry of the LSHR crystal and the resulting difference in the number of equivalent planes within each $\{hkl\}$ family - a property known as multiplicity [17].

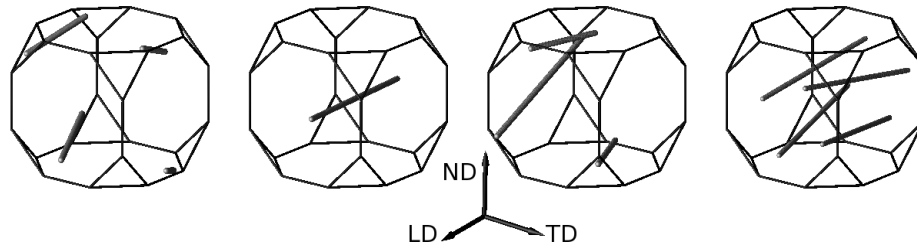


Figure 1.4: The $\{111\}||\text{LD}$, $\{200\}||\text{LD}$, $\{220\}||\text{LD}$, and $\{311\}||\text{LD}$ fibers, going left to right are plotted in the fundamental zone.

The quality of orientation pole figures is often linked to pole figure coverage [68]. From Figure 1.4, it is clear that for micromechanical testing especially, it is also necessary to consider the section of orientation space being sampled during each measurement. Specifically, for identical pole figure coverage, different regions of orientation space are sampled for each $\{hkl\}$. Probing a wide range of orientation space is essential for determining the lattice strain tensor at each orientation - the LSDF. Each measurement contains information about the weighted projection of the orientation-averaged strain tensors that fall along

the fiber. The influence of each lattice strain measurement, or point on the pole figure, on the determination of the LSDF (Inversion) is coupled to the region and direction of the corresponding crystallographic fiber. Mapping peak shifts (lattice strains) from diffraction measurements back to individual orientations is the fundamental challenge of the SPF inversion. The hope for a solution lies in multiple lattice strain measurements that involve each crystal orientation. Obtaining the greatest amount of lattice strain information from each orientation during an SPF experiment improves our ability to determine the LSDF.

1.2.6 The Lattice Strain Distribution Function (LSDF)

The Lattice Strain Distribution Function (LSDF) is the lattice strain tensor at each orientation, $\underline{\epsilon}(\mathbf{R})$. In a powder sample, the intensity for each diffracted peak comes from the crystals along the fiber defined by $\mathbf{c}||\mathbf{s}$. The peak shift on the detector is due to the orientation averaged projection of the LSDF along the fiber in the direction of the scattering vector, \mathbf{s} :

$$\epsilon_{\mathbf{c}||\mathbf{s}} = \frac{d_{\mathbf{c}||\mathbf{s}} - d_{\mathbf{c}||\mathbf{s}}^0}{d_{\mathbf{c}||\mathbf{s}}^0} = \frac{\int_{\mathbf{c}||\mathbf{s}} \mathbf{s}\underline{\epsilon}(\mathbf{R})\mathbf{s}^T f(\mathbf{R})d\mathbf{R}}{\int_{\mathbf{c}||\mathbf{s}} f(\mathbf{R})d\mathbf{R}} \quad (1.11)$$

where T indicates the transpose. Here, $f(\mathbf{R})$ is the Orientation Distribution Function (ODF) [3] defined as:

$$\frac{dV_{\beta}}{V_{\beta}} \equiv \frac{1}{V_{\Omega}} f(\mathbf{R})d\mathbf{R}. \quad (1.12)$$

Here V_{β} is the volume of the real material, V_{Ω} is the associated volume in orientation space. Additionally, the integral of the ODF over the orientation space, Ω , must equal one and $f(\mathbf{R}) \geq 0$.

The LSDF is often the objective of the powder experiments and can be used with Hooke's law and the single crystal elastic constants, $\underline{\mathbf{C}}$, to obtain the average stress for each crystal orientation [4–6, 49]:

$$\underline{\sigma}(\mathbf{R}) = \underline{\mathbf{C}}\underline{\epsilon}(\mathbf{R}) \quad (1.13)$$

The inversion process presented in [4] seeks to determine the LSDF using the finite element discretization shown in Figure 1.3. The LSDF can be represented with a finite element discretization over the fundamental zone. The LSDF is defined within an element in orientation space as,

$$\underline{\epsilon}(\mathbf{R}) = [N(\mathbf{R})]\{\epsilon\} \quad (1.14)$$

where $\{\epsilon\}$ is the vector of nodal point values of the LSDF and $[N(\mathbf{R})]$ are shape functions defined in orientation space. The 600 node finite element mesh shown in Figure 1.3, combined with the six components of the LSDF, results in 3600 degrees of freedom (number of nodes \times the six components of the LSDF) necessary for the inversion process. The SPF experiment can now be described from the standpoint of defining the LSDF at each node in orientation space.

1.3 Measuring SPFs at CHESS Experimental Station A2

The $\{hkl\}$ s that produce diffracted intensity are governed by the crystal structure and lattice parameters of the sample, x-ray wavelength, and the experiment geometry. Similar to increasing the distance between a projector and a screen, an increase in the sample to detector distance while holding the material and wavelength fixed will result in fewer diffracted $\{hkl\}$ s captured by the detector.

However, the shift of a peak results in a larger physical distance on the detector which improves the strain resolution. Clearly, experiment conditions should be optimized to produce the maximum number of $\{hkl\}$ s while still maintaining adequate sensitivity for peak shifts measured on the detector.

1.3.1 Material and Specimen Design

The SPF experiments we describe were conducted on the nickel base superalloy LSHR, which was developed by NASA as a new high temperature turbine disk alloy that can be heat treated to produce fine or coarse grains to vary the mechanical performance [28]. The LSHR material had an average grain size of approximately $3\mu\text{m}$ and the x-ray intensities measured indicate a near uniform ODF. The specimen geometry for the LSHR corresponded to a flat sample with a gage length of 36.83 mm and a cross section of 1 mm x 1.25 mm (ND x TD). For diffraction experiments in transmission, the allowable specimen thickness is governed by the penetration depth of the x-rays, which is determined from the absorption characteristics of the material and the x-ray energy [48]. The LSHR sample thickness was designed specifically for the 50 keV x-rays at CHESS A2.

To build reliable SPFs and to quantify the LSDF, the material grain size and x-ray beam size must be coordinated so the diffraction volume contains “enough” grains to satisfactorily represent a distribution. Each measurement must constitute the response from a material point (in the continuum sense). If the number of participating crystals decreases, so that the lattice strain response can be significantly changed by the addition of several crystals to the diffraction volume, the general concept of a material point is violated. The azimuthal bin size is also

linked to the number of crystals interrogated. The complete LSHR Debye rings shown in Figure 1.2(a), and the relatively small grain size of the LSHR, indicate that idea of material point is satisfied with each diffraction pattern divided into 72, 5° azimuthal bins (η).

1.3.2 Experiment Conditions

The SPF experiment was conducted in transmission with 49.989 keV ($\lambda = 0.2480 \text{ \AA}$) x-rays in the A2 experimental station at the Cornell High Energy Synchrotron Source (CHESS). The flux at this energy for a 5.3GeV synchrotron is approximately 5.52×10^{11} photons/mm²/second, which is orders of magnitude greater than a typical rotating anode laboratory source at the same energy. The beam path for the x-ray experiment can be seen in the schematic in Figure 1.5. The A2 hutch is approximately $4 \times 2 \text{ m}^2$ and is located 35.5 m downstream from the wiggler (series of magnets with alternating polarity) where the x-rays are produced [69]. The x-ray beam from the wiggler contains a wide range of energies. A silicon {111} double-crystal monochromator is used to select a single energy to within a bandwidth of 50 eV. The cross-section of the incoming beam is set to $0.5 \times 0.5 \text{ mm}^2$ by two sets of tungsten slits. The flight chamber (helium filled chamber to minimize x-ray interaction with air) and a collimator (lead cylinder to minimize x-ray scattering along the beam path) are used to minimize the amount of spurious x-rays. After leaving the collimator, the x-ray strikes the sample mounted within the diffractometer. A MAR345 area detector was placed 645 mm from the sample. The detector has $100\mu\text{m}$ square pixels and a diameter of 345 mm. For these experiment conditions the $\{hkl\}_s$ considered are the {111}, {200}, {220}, and {311} as shown in Figure 1.2.

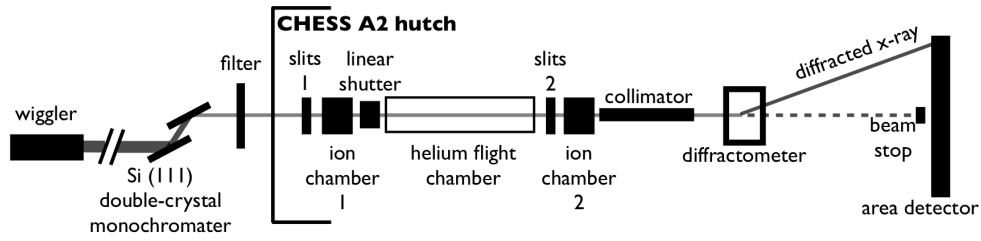


Figure 1.5: Schematic showing the relevant components in the x-ray beam path at CHESS A2 for the SPF experiment.

The diffractometer, labeled in Figure 1.5 and pictured in Figure 1.6, allows for the reorientation of the loaded sample [57]. Traditional diffractometers can precisely reorient small samples, but do not offer *in situ* loading capabilities [17]. The addition of the loadframe, labeled G in Figure 1.6, drastically increases the amount of rotated mass and the need for substantial structural members to resist deflection. Two rotational axes are used to reorient the specimen relative to the x-ray beam. For sample symmetry considerations, the specimen loading direction (LD) was chosen as one rotational axis (χ) and the vertical axis perpendicular to the beam as the second (ω). The most important attribute for our diffractometer is the ability to reorient a specimen during loading with minimal changes to the position of the specimen centroid with respect to the incoming x-ray beam. The loadframe is capable of holding a constant load while being rotated and can apply and maintain loads of up to ± 2250 N in tension or compression at a frequency of up to 100 Hz. We typically conduct load control experiments due to the strong dependence of lattice strain on the applied load [51].

The experimental procedure using the system shown in Figure 1.6 consists of a sequence of diffraction measurements and sample rotations [48]. At $\omega = \chi = 0^\circ$ the sample ND is aligned with the direct beam. The angular range for the rota-

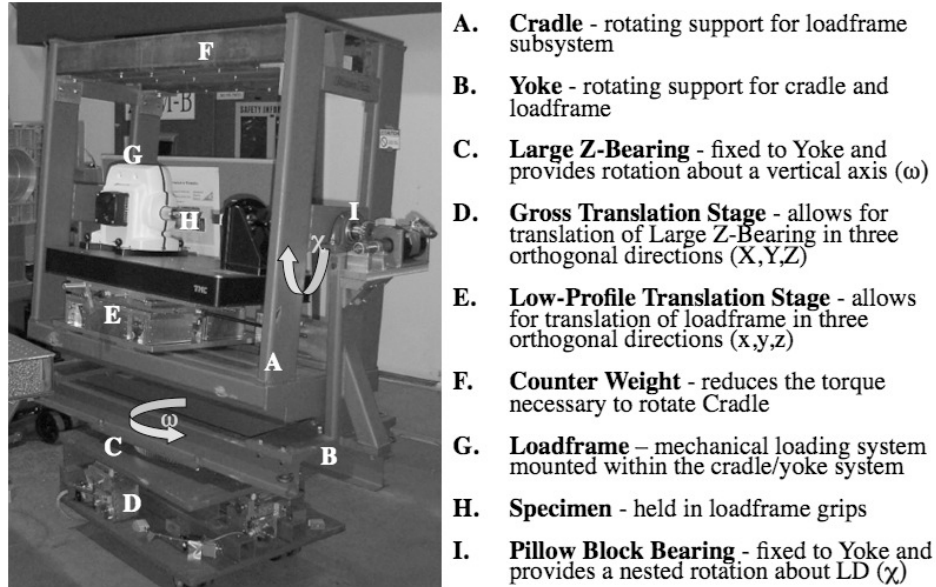


Figure 1.6: Loadframe/diffractometer employed for the SPFs experiments depicting the relevant components.

tions are from $\omega = [-40^\circ \text{ to } 35^\circ]$ and $\chi = [0^\circ \text{ to } 25^\circ]$. Once the desired point in the load history is attained the load is reduced to a constant value at 90% of the peak value to reduce the effect of creep during the diffraction measurements [18]. A complete *in situ* tension test contains many hold periods in the load history (in both the elastic and elastic-plastic regimes) to measure SPFs at specific points [5, 6, 48, 51].

1.4 Orientation Space Sampling

In this section we derive an explicit relationship between the sample orientations that are possible at each load step, the set of $\{hkl\}$ s observed and the crystal orientations interrogated during each diffraction measurement. Due to the limited set of crystallographic planes that diffract and the nature of Bragg's law, for

a given experimental setup there are a fixed number of crystallographic fibers (diffraction measurements) that can pass through a point in orientation space. Optimal design of a diffraction experiment comes from a recognition of the connection between sample orientations relative to the x-ray beam and the nature of the relationship between $\{hkl\}$ s and potential fiber directions. An understanding of how each diffraction measurement probes orientation space and the selection of key measurement directions can be used to optimize an investigation of the crystal scale mechanical response.

To illustrate the problem, let us consider three sample orientations used on the LSHR material: $(\omega, \chi) = (-40^\circ, 0^\circ)$, $(0^\circ, 0^\circ)$, and $(35^\circ, 0^\circ)$. In Figure 1.7 the SPF coverage is shown with the corresponding fibers in orientation space. As expected, plotting many fibers produces a completely intractable figure, therefore to allow for each fiber to be identified, the fibers are shaded from black to gray with every other azimuthal bin omitted. The relationship between all of these fibers and a single crystal orientation is complex. From Figure 1.7 we can see that the challenge of determining the impact of these measurements at each crystal orientation is nontrivial.

Our focus is on defining a technique for quantifying the extent to which each crystal orientation is interrogated during a diffraction experiment. Presentation of the technique will be shown for a range of SPF coverage using the crystal structure of the LSHR and the experiment conditions presented in Sect. 1.3.2. The experiment configurations considered are: diffraction measurements in the LD and TD directions only (typical neutron experiment), a single diffraction pattern ($\omega = \chi = 0^\circ$), and three results achieved using different ranges of ω and χ .

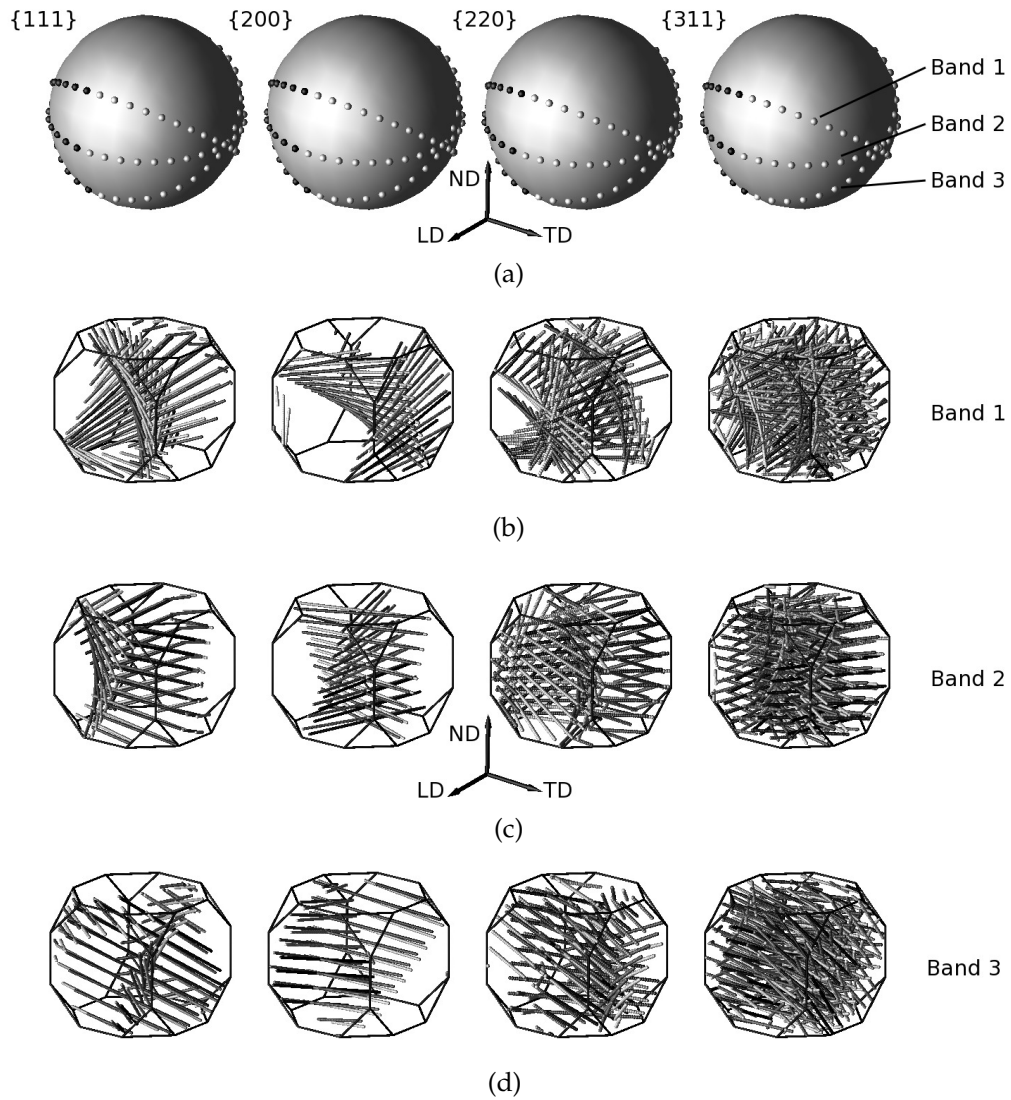


Figure 1.7: (a) Results from three different diffraction patterns are shown on both the SPFs and in the fundamental zone. The results correspond to the $\{111\}$, $\{200\}$, $\{220\}$, and $\{311\}$ going left to right. The shading varies from gray to black along a single band to allow for identification of each point. The fibers shown in (b), (c) and (d) are each from a single band of data indicated in (a).

Table 1.1: Multiplicity values for an FCC material.

$\{hkl\}_s$	$\{111\}$	$\{200\}$	$\{220\}$	$\{311\}$
Multiplicity (M)	8	6	12	24

1.4.1 The Orientation Space Sampling Matrix, $\Gamma(\mathbf{R})$

To quantify the relationship between the experimental conditions and the regions and directions in orientation space that each fiber probes we consider a single orientation \mathbf{R}_i , with an elastic strain tensor $\underline{\epsilon}(\mathbf{R}_i)$. As defined in Equation 1.3 for a given crystal vector, \mathbf{c} , we can unequivocally define a scattering vector, \mathbf{s} , such that a crystallographic fiber will pass through \mathbf{R}_i . The maximum set of fibers that interrogate \mathbf{R}_i is fixed by two things: 1) the $\{hkl\}_s$ that can be measured in the diffraction experiment and 2) their crystallographic multiplicities. In the LSHR experiment we collect data for the $\{111\}$, $\{200\}$, $\{220\}$, and $\{311\}$ planes. The multiplicity of an $\{hkl\}$ depends on the crystal system and is defined as the number of unique crystallographic planes within a unit cell that have different orientations but share a common plane spacing [17]. LSHR is FCC and the multiplicities for the observed $\{hkl\}_s$ are shown in Table 1.1. To quantify the set of fibers that probe \mathbf{R}_i , the multiplicities for each $\{hkl\}$ are combined with Equation 1.3 to generate a list of $\mathbf{c}||\mathbf{s}$ combinations. For instance the scattering vectors required to produce all six possible $\{200\}$ fibers correspond to $\mathbf{R}_i\mathbf{c}$ where $\mathbf{c} = \frac{1}{2} [2\ 0\ 0]$, $\frac{1}{2} [-2\ 0\ 0]$, $\frac{1}{2} [0\ 2\ 0]$, $\frac{1}{2} [0\ -2\ 0]$, $\frac{1}{2} [0\ 0\ 2]$, and $\frac{1}{2} [0\ 0\ -2]$.

Due to the antipodal symmetry of pole figure data ($\pm\mathbf{s}$), the potential number of measurement directions is halved. For each $\{hkl\}$ considered, the number of possible measurement directions that probe \mathbf{R}_i is one-half the multiplicity. For

the four $\{hkl\}_s$ in Table 1.1, the total number of unique fibers that probe each orientation is limited to 25. Therefore, at an orientation \mathbf{R}_i , there are 25 possible lattice strain measurements that can probe $\underline{\epsilon}(\mathbf{R}_i)$.

Single Crystal Measurements

To illustrate the importance of measuring lattice strains in many directions, let us consider a single crystal i of the LSHR, with an orientation \mathbf{R}_i subjected to an elastic strain state $\underline{\epsilon}(\mathbf{R}_i)$. Each lattice strain measurement constitutes a projection of the tensor in the measurement direction:

$$\epsilon_{c||s} = \mathbf{s}\underline{\epsilon}(\mathbf{R}_i)\mathbf{s}^T \quad (1.15)$$

By expressing $\underline{\epsilon}(\mathbf{R}_i)$ as a vector this expression can be rearranged as [34]:

$$\epsilon_{c||s} = [u^2 \ v^2 \ w^2 \ 2vw \ 2uw \ 2uv] \left\{ \begin{array}{l} \epsilon_{11}(\mathbf{R}_i) \\ \epsilon_{22}(\mathbf{R}_i) \\ \epsilon_{33}(\mathbf{R}_i) \\ \epsilon_{23}(\mathbf{R}_i) \\ \epsilon_{13}(\mathbf{R}_i) \\ \epsilon_{12}(\mathbf{R}_i) \end{array} \right\} \quad (1.16)$$

with the unit scattering vector, \mathbf{s} , previously defined as $\mathbf{s} = [u \ v \ w]$. For m measurements (scattering vectors) of the same crystal i , Equation 1.16 can be written in matrix form as:

$$[\epsilon_{c||s}] = \mathbf{\Gamma}(\mathbf{R}_i)\{\epsilon(\mathbf{R}_i)\} \quad (1.17)$$

where $\{\epsilon(\mathbf{R}_i)\} = \{\epsilon_{11}(\mathbf{R}_i) \ \epsilon_{22}(\mathbf{R}_i) \ \epsilon_{33}(\mathbf{R}_i) \ \epsilon_{23}(\mathbf{R}_i) \ \epsilon_{13}(\mathbf{R}_i) \ \epsilon_{12}(\mathbf{R}_i)\}^T$, $[\epsilon_{c||s}]$ is the list of measured lattice strains for the m measurements, and the orientation space sam-

pling matrix, $\Gamma(\mathbf{R}_i)$, is defined:

$$\Gamma(\mathbf{R}_i) = \begin{bmatrix} u_1^2 & v_1^2 & w_1^2 & 2v_1w_1 & 2u_1w_1 & 2u_1v_1 \\ u_2^2 & v_2^2 & w_2^2 & 2v_2w_2 & 2u_2w_2 & 2u_2v_2 \\ & & & \cdot & & \\ & & & \cdot & & \\ & & & \cdot & & \\ u_m^2 & v_m^2 & w_m^2 & 2v_mw_m & 2u_mw_m & 2u_mv_m \end{bmatrix} \quad (1.18)$$

where m can be at most the number of unique fibers for each orientation, 25 for a single crystal of LSHR using the experiment conditions presented in Sect. 1.3.2. Additional measurements beyond the 25 unique fibers would be replicants and could be used to minimize the influence of experimental fluctuations. To determine the lattice strain tensor for a single crystal i , $\Gamma(\mathbf{R}_i)$ must contain six linearly independent rows. The rank of a matrix is defined as the number of linearly independent rows. For $\Gamma(\mathbf{R}_i)$ the maximum rank is equal to the number of independent strain components, six. So if $\Gamma(\mathbf{R}_i)$ spans \mathcal{R}^6 , a six-dimensional space of real numbers, then the strain tensor for the crystal i can be determined from the lattice strain measurements. If additional measurements are made the problem of determining the lattice strain tensor becomes one of linear least squares. From linear algebra, we know that six measurements (rows of $\Gamma(\mathbf{R}_i)$) do not ensure that $\Gamma(\mathbf{R}_i)$ spans \mathcal{R}^6 .

Orientation Space Sampling Matrix for a Polycrystal

For a polycrystal, each lattice strain measurement comes from many crystal orientations along individual fibers. To quantify the orientation space matrix, $\Gamma(\mathbf{R})$, for each orientation, we restrict our investigation to the orientations defined by

the nodes of the finite element discretization described previously, Figure 1.3. Recall that for each orientation, there exists a finite set of potential scattering vectors defined by $\mathbf{R}_i \mathbf{c}$. For the LSHR and the experiment conditions presented in Sect. 1.3.2, this set of scattering vectors is limited to 25. To discern whether a measurement probes a given orientation, a tolerance of 2.5° between the measured scattering vector and the set of potential scattering vectors for the orientation is employed.

Using this criteria, the orientation space sampling matrix, $\mathbf{\Gamma}(\mathbf{R})$, can be calculated for each orientation (node), and the extent to which each orientation is interrogated can be quantified. The rank of $\mathbf{\Gamma}(\mathbf{R})$ for each crystal orientation can be used to generate a field over orientation space that indicates how well each orientation is sampled by a set of SPF data. Again, the maximum possible rank of $\mathbf{\Gamma}(\mathbf{R})$ is equal to the number of independent strain components, six. So if the orientation space sampling matrix spans $\mathcal{R}6$ at each orientation, then the inversion process simplifies to a matrix operation.

The relationship between the LSDF and the SPFs can be expressed using nodal point values. Here the LSDF for each node is defined as a vector:

$$\{\epsilon\} = \{\epsilon_{11}(\mathbf{R}_1) \dots \epsilon_{11}(\mathbf{R}_n) \epsilon_{22}(\mathbf{R}_1) \dots \epsilon_{22}(\mathbf{R}_n) \epsilon_{33}(\mathbf{R}_1) \dots \epsilon_{33}(\mathbf{R}_n) \epsilon_{23}(\mathbf{R}_1) \dots \epsilon_{23}(\mathbf{R}_n) \epsilon_{13}(\mathbf{R}_1) \dots \epsilon_{13}(\mathbf{R}_n) \epsilon_{12}(\mathbf{R}_1) \dots \epsilon_{12}(\mathbf{R}_n)\}^T, \quad (1.19)$$

where n equals 600 and is the total number of nodes in the fundamental zone shown in Figure 1.3. For p measurements the set of lattice strains is expressed

as:

$$[\epsilon_{\mathbf{c}||\mathbf{s}}] = \begin{bmatrix} \epsilon_1 \\ \cdot \\ \cdot \\ \cdot \\ \epsilon_p \end{bmatrix} \quad (1.20)$$

where the subscript $\mathbf{c}||\mathbf{s}$ for each lattice strain measurement is replaced with an index that ranges from 1 to p . In an analogous manner to that of the single crystal example, the relationship between the LSDF and the SPFs is defined:

$$[\epsilon_{\mathbf{c}||\mathbf{s}}] = \mathbf{\Gamma}^* \{\epsilon\} \quad (1.21)$$

where $\mathbf{\Gamma}^*$ is the polycrystal sampling matrix. The polycrystal sampling matrix combines information from the scattering vector with a weight for the contribution of each orientation to the lattice strain measurement. The subset of orientations that contribute to a single measurement is indicated by a characteristic function defined:

$$\{B_{\mathbf{c}||\mathbf{s}}\} = \{B(\mathbf{R}_1) \dots B(\mathbf{R}_n)\} \quad (1.22)$$

where $\{B_{\mathbf{c}||\mathbf{s}}\}$ is defined for each node in orientation space to be one if the orientation contributes to the measurement, and zero if it does not. The ODF is defined for each node as:

$$\{f\} = \{f(\mathbf{R}_1) \dots f(\mathbf{R}_n)\}. \quad (1.23)$$

Using both $\{B_{\mathbf{c}||\mathbf{s}}\}$ and $\{f\}$, the contribution of each orientation to a single lattice strain measurement is defined:

$$\{F_{\mathbf{c}||\mathbf{s}}\} = \frac{\{f(\mathbf{R}_1)B(\mathbf{R}_1) \dots f(\mathbf{R}_n)B(\mathbf{R}_n)\}}{\{f\}\{B_{\mathbf{c}||\mathbf{s}}\}^T}. \quad (1.24)$$

Here $\{F_{\mathbf{c}||\mathbf{s}}\}$ is a vector containing normalized weights such that the components sum to one. Using $\{F_{\mathbf{c}||\mathbf{s}}\}$ and the scattering vector, \mathbf{s} , the polycrystal sampling

matrix is defined:

$$\mathbf{\Gamma}^* = \begin{bmatrix} u_1^2\{F_1\} & v_1^2\{F_1\} & w_1^2\{F_1\} & 2v_1w_1\{F_1\} & 2u_1w_1\{F_1\} & 2u_1v_1\{F_1\} \\ & & & \cdot & & \\ & & & \cdot & & \\ & & & \cdot & & \\ u_p^2\{F_p\} & v_p^2\{F_p\} & w_p^2\{F_p\} & 2v_pw_p\{F_p\} & 2u_pw_p\{F_p\} & 2u_pv_p\{F_p\} \end{bmatrix} \quad (1.25)$$

where the subscript $c|s$ for each $\{F_{c|s}\}$ is replaced with an index that ranges from 1 to p to indicate each measurement.

To solve Equation 1.21 for the LSDF using matrix operations requires the rank of $\mathbf{\Gamma}^*$ to be 3600 (the number of nodes \times the six degrees of freedom in the LSDF). When the rank of $\mathbf{\Gamma}^*$ is 3600, the rank of the orientation space sampling matrix, $\mathbf{\Gamma}(\mathbf{R})$, is six for all nodes in the mesh. It is beneficial to measure as many of the 25 potential fibers at each orientation as possible. Measurements in addition to the six linearly independent required for $\mathbf{\Gamma}(\mathbf{R})$ to span \mathcal{R}^6 for each orientation ($p > n$), act to minimize the influence of experimental error and enables the use of least squares for determining the LSDF. Once the LSDF is determined for each node, the LSDF value for an arbitrary orientation can be determined with Equation 1.14 using the finite element shape functions. It is worth noting that the LSDF obtained by solving Equation 1.21 is influenced by experimental errors and additional constraints may be needed depending on the quality of the lattice strain data.

When the rank of $\mathbf{\Gamma}^*$ is less than 3600, additional constraints are necessary to find a unique solution to the inversion process [4, 66]. The orientation space sampling matrix, $\mathbf{\Gamma}(\mathbf{R})$, can be used to identify the orientations that are poorly sampled. Using both the orientations where $\mathbf{\Gamma}(\mathbf{R})$ is rank deficient and the set of 25 potential fibers for each orientation, measurements that produce linearly

Table 1.2: SPF experiment configurations investigated.

Configuration	Description
1	Measurements in the LD and TD directions only (conventional neutron diffraction experiment)
2	Single diffraction pattern ($\omega = \chi = 0^\circ$)
3	Configuration presented in Figure 1.7
4	Rotations about the vertical axis ($\omega = -40^\circ$ to 35° in nine increments with $\chi = 0^\circ$) using the diffractometer shown in Figure 1.6
5	SPF coverage used in the LSHR experiments ($\omega = -40^\circ$ to 35° in nine increments with $\chi = 0^\circ$ and $\chi = 12.5^\circ$ and $\omega = -25^\circ$ to 25° in six increments with $\chi = 25^\circ$)

independent rows of Γ^* can be identified.

The orientation space sampling matrix is explored using a range of experimental configurations. The SPF coverage investigated is shown for the $\{111\}$ SPF in Figure 1.8, where each SPF corresponds to one of the experiment configurations defined in Table 1.2. The five configurations were selected to demonstrate the orientation space sampling matrix for common diffraction experiments where configuration (1) represents a typical neutron experiment, (2) represents a single sample orientation using an area detector, and (3) to (5) represent increasing amounts of SPF coverage obtained with the diffractometer shown in Figure 1.6.

The number of fibers that pass through each orientation is shown over the

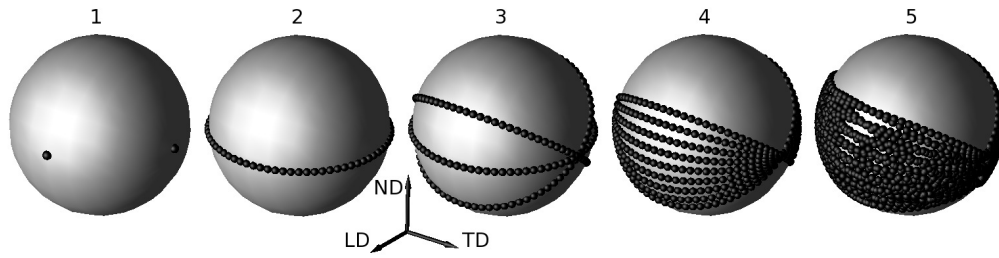


Figure 1.8: SPF coverage for the experiment configurations described in Table 1.2. For configurations 2 to 5 the measurement positions on the SPF correspond to the $\{111\}$. The measurement positions for the remaining $\{hkl\}$ s differ from the $\{111\}$ by less than a few degrees.

fundamental zone for the different experiment configurations in Figure 1.9. For the set of $\{hkl\}$ s measured there exists at most 25 independent fibers that can pass through a single orientation. The total number of unique measurements, increases from left to right in Figure 1.9. For (5) a minimum of 10 fibers pass through each orientation.

The rank of the orientation space sampling matrix, $\mathbf{\Gamma}(\mathbf{R})$, for each of the experiment configurations is plotted over orientation space in Figure 1.10. The results show a drastic increase in the rank of the orientation space sampling matrix at each orientation with increasing SPF coverage, left to right in Figure 1.8. For SPF configuration (4), 588 of the 600 nodes in the finite element mesh are of rank six. If necessary the rank deficient nodes could be isolated and additional measurements prescribed from the set of 25 potential fibers to increase the rank of $\mathbf{\Gamma}(\mathbf{R})$ for the specific orientations. For (5), the SPF coverage used in the LSHR experiment, the rank of the orientation space sampling matrix has a uniform value of six over orientation space.

We motivated our effort to quantify how well a set of SPF data probes ori-

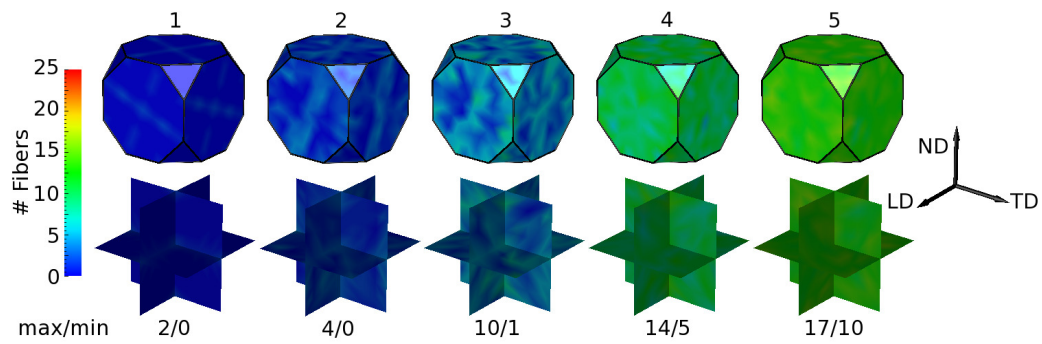


Figure 1.9: The number of unique fibers that pass through each orientation for the configurations described in Table 1.2 are shown in the fundamental zone. The top row shows the outer surface of the fundamental zone and the bottom row shows three interior orthogonal plane sections of the same region. The upper limit for the $\{hkl\}$ s measured is 25 fibers per orientation. Due to incomplete SPF coverage for the different configurations the most fibers to pass through a single orientation is 17 for (5).

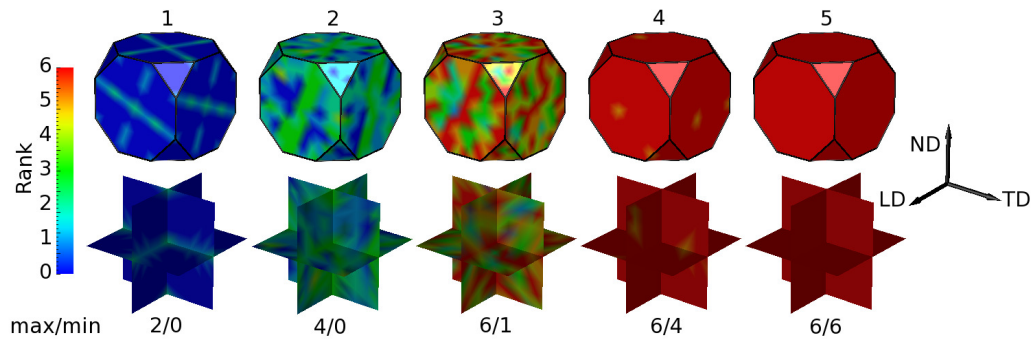


Figure 1.10: The rank of the orientation space sampling matrix over orientation space for each of the configurations described in Table 1.2. By moving from (1) to (5) the inversion problem becomes over constrained.

entation space with (3), and the corresponding fibers shown in Figure 1.7. By shifting the focus from all the fibers in the fundamental zone, to the subset of fibers that probe each orientation, we are able to quantitatively investigate the orientation space coverage as shown by Figure 1.9 and Figure 1.10 .

1.5 SPF Experiment on LSHR

The macroscopic behavior of a LSHR specimen subjected to a uniaxial stress state is shown in Figure 1.11(a). Diffraction measurements of LSHR were made while the load was held at 225 MPa, 450 MPa, and 720 MPa in uniaxial tension. The SPF experiment is not limited to the elastic regime [5, 48, 49], but since the focus of this paper is on developing an understanding of diffractometer configuration, pole figure coverage, and potential rank of the orientation space sampling matrix for each crystal orientation, we focus on three loads in the elastic regime. The load history for the experiment is shown in Figure 1.11(b) where both stress and strain are plotted versus time. SPFs were measured for the four $\{hkl\}_s$ at the three different load steps. Each SPF combines lattice strain data from 24 different sample orientations. Each diffraction pattern was divided into 72 azimuthal bins leading to 1728 unique lattice strain measurements per $\{hkl\}$. The SPFs are presented in Figure 1.12 and for plotting purposes lattice strains are shown both for $\pm s$.

The SPF for each $\{hkl\}$ shows that for the *in situ* conditions, the largest tensile lattice strains are nominally in LD and most compressive in TD from the Poisson effect. The magnitude of the lattice strains in LD between the different $\{hkl\}_s$ follows the general trends consistent with the single crystal elastic anisotropy of

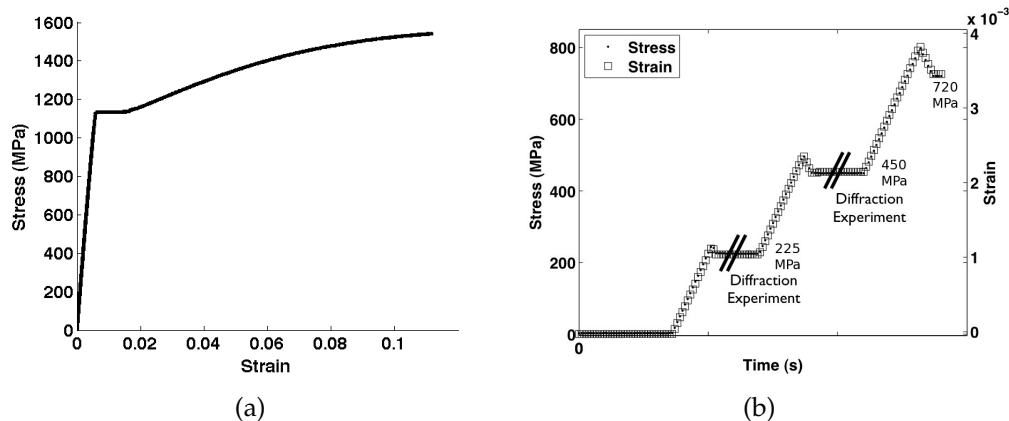


Figure 1.11: (a) Macroscopic engineering stress vs. engineering strain curve for the LSHR in the as forged state. (b) Stress and strain plotted vs. time for the LSHR specimen. To mitigate creep effects the load is decreased to 90% during the diffraction measurements. During the periods where the load is held constant, the sample is rotated to allow additional unique scattering vectors to be measured. For scale our load hold period is approximately an hour using the MAR345 area detector.

the material where the $\{200\}$ is the most compliant (largest lattice strain magnitude) and the $\{111\}$ is the stiffest in uniaxial tension. Variation in the lattice strain values between neighboring points on an SPF are not expected to vary significantly over a few degrees. The lattice strain uncertainty that is commonly quoted for these experiments is approximately $\pm 1 \times 10^{-4}$ [5]. This value is consistent with our experimental data.

1.6 Discussion

Upon initial examination, designing a measurement **capability** that would conceivably interrogate every orientation within a deforming polycrystalline aggregate feels like a daunting task. However, the geometric predictability that

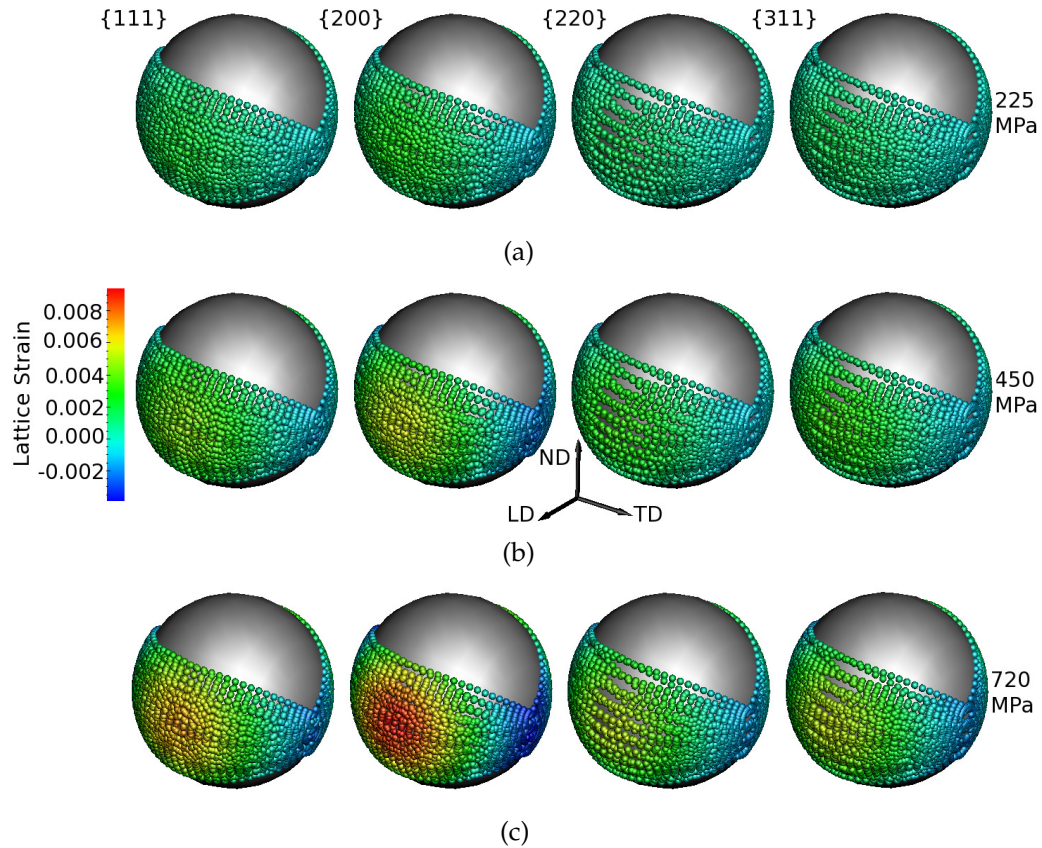


Figure 1.12: SPFs for $\{111\}$, $\{200\}$, $\{220\}$, and $\{311\}$ going left to right. Top to bottom corresponds to the SPFs measured at a macroscopic stress of (a) 225 MPa, (b) 450 MPa, and (c) 720 MPa in tension.

accompanies crystal symmetries and the enormous number of diffraction measurements that are possible with high energy x-rays and area detectors have made it possible to define and easily quantify the orientation space sampling matrix, $\Gamma(\mathbf{R})$, for each crystal orientation. Experiment design then becomes a matter of understanding the effect that each experimental parameter (x-ray energy, sample to detector distance, number, orientation, and angle range of specimen rotation axes) has on the rank of $\Gamma(\mathbf{R})$ at each crystal orientation. Understanding the rank of $\Gamma(\mathbf{R})$ allows us to judge the quality of a set of SPFs in a more meaningful and quantitative manner than pole figure coverage. Whether

our ultimate intent is to compare measured SPFs to simulation results or to invert a set of SPFs for the LSDF and eventually the average stress for each orientation ($\underline{\sigma}(\mathbf{R})$); understanding of the orientation space sampling matrix can be used to select experiment conditions, govern the design of new apparatus like a diffractometer, and determine the $\{hkl\}$ s and scattering vectors to best probe the material response - particularly for the case of limited measurements and materials with strong textures. The definition of $\mathbf{\Gamma}(\mathbf{R})$ now allows us to declare a set of SPFs as good, better or best.

Time at synchrotron facilities is a valuable resource. Understanding the relationship between each diffraction measurement and the LSDF elevates the SPF micromechanical testing techniques to a point where the experiment can be optimized prior to making a measurement. The material characteristics, the x-ray wavelength, the sample to detector distance, the detector size, and the diffractometer design dictate the SPF coverage. The SPF coverage and the $\{hkl\}$ s measured can be used to identify the independent fibers that probe each orientation, and which are accessible to a given experimental setup. Generally speaking, the quality of the information about the three dimensional deformation state of the polycrystalline aggregate improves with increased SPF coverage. The degree to which the results improve can be quantified by the rank of $\mathbf{\Gamma}(\mathbf{R})$ for each orientation and the number of fibers measured. The discussion will focus on three topics: the maximum number of fibers that probe a single orientation, the impact of limited SPF coverage, and the use of $\mathbf{\Gamma}(\mathbf{R})$ to investigate relationship between SPFs and the LSDF.

1.6.1 The Number of Potential Fibers that Probe Each Orientation

The maximum number of fibers that probe a single orientation is fixed by the $\{hkl\}$ s measured and their corresponding multiplicities. The addition of each independent $\{hkl\}$ increases the maximum number of fibers that can probe each orientation by one-half the multiplicity. The addition of $\{hkl\}$ s at higher Bragg angles is often limited by the size of the detector and the experimental conditions. For the LSHR and the experimental conditions employed, the maximum number of fiber the probe each orientation was 25.

It is worth noting that for an orientation, \mathbf{R}_i , measurement of additional higher order planes, such as the $\{111\}$ and the $\{222\}$ does not increase the maximum number of potential fibers that can interrogate each orientation. Since each fiber is defined by Equation 1.3, where for cubic materials $\mathbf{c} = \frac{1}{\sqrt{h^2+k^2+l^2}}[h \ k \ l]$, then for a fixed scattering vector the $\{111\}$ and $\{222\}$ fibers are identical. When diffraction from the $\{111\}$ and $\{222\}$ peaks is measured with an area detector, the scattering vectors are slightly different (different s 's), and the result is analogous to more $\{111\}$ measurement directions.

1.6.2 Limited SPF Coverage

While the maximum number of fibers that probe each orientation for the LSHR using the experiment conditions presented in Sect. 1.3.2 is 25, the number of diffraction measurements made depends on the experimental configuration. Using the rank of $\mathbf{\Gamma}(\mathbf{R})$ as a metric, the impact of limited SPF coverage due to

interference between x-rays and the experimental apparatus during the rotation of the sample (referred to as shadowing) can be quantified. Given a desire for the orientation space sampling matrix to be of rank 6 for all orientations, the minimum allowable SPF coverage can be established and used to constrain the experiment design. For the case where only limited measurements are possible, due to time or shadowing constraints, the orientation space sampling matrix can be used with the ODF to maximize the volume of the material interrogated. For a material with a strong texture, the subset of orientations that represent the largest volume fraction of the material can be used to prescribe measurement directions that most effectively interrogate the material response. Additionally, the quality of an experimental design can be assessed and adapted if crucial regions of orientation space are not adequately sampled.

As the number of measurements decreases, the impact of which $\{hkl\}$ s are measured increases. Though the SPF coverage will be similar for different $\{hkl\}$ s, the variation in the amount of orientation space probed is appreciable. As shown by the the four fibers in Figure 1.4, the range of orientations that are encompassed by a single fiber scales with the multiplicity. As a result, a single $\{200\}$ measurement probes significantly fewer orientations than a $\{311\}$ measurement. It is important to note that though the $\{200\}$ fibers constitute the minimal amount of orientation space sampling, if an experiment was designed such that all possible $\{200\}$ fibers were accessible, the orientation space sampling matrix for each orientation would only span \mathcal{R}^3 . Measurement of several $\{hkl\}$ s greatly improves the rank of the orientation space sampling matrix for similar SPF coverage. Moreover, due to anisotropic single crystal properties, the lattice strains for each $\{hkl\}$ shown in Figure 1.12 can be different. Depending on the nature of the investigation, it may be valuable to measure certain $\{hkl\}$ s

that correspond to extreme values of the single crystal elastic response, rather than maximizing orientation space coverage.

1.6.3 The Link Between SPF Data and the LSDF

The polycrystal projection matrix, $\mathbf{\Gamma}^*$, links the experimentally measured lattice strains (SPFs) to the average strain tensor experienced by each crystal orientation within the diffraction volume (LSDF). Each lattice strain measurement represents a row in $\mathbf{\Gamma}^*$, and for Equation 1.21 to be solved directly there must be at least as many linearly independent rows in $\mathbf{\Gamma}^*$ as there are degrees of freedom in the LSDF (3600 for the mesh shown in Figure 1.3). When the rank of $\mathbf{\Gamma}^*$ is insufficient to determine the LSDF directly, additional constraints can be applied to obtain a unique solution. Such is the case for configurations 1-4 in Figure 1.8. From an experiment design perspective, the rank of $\mathbf{\Gamma}(\mathbf{R})$ can be used to identify orientations that are insufficiently probed (rank less than 6), and new measurements that interrogate the rank deficient orientations can be prescribed to generate additional linearly independent rows in $\mathbf{\Gamma}^*$. When it is not possible to make additional measurements to improve the inversion process, it is conceivable to use the rank of each orientation space sampling matrix as a confidence measure for inversion results. Additional measurements beyond the set required for $\mathbf{\Gamma}(\mathbf{R})$ to span $\mathcal{R}6$ at each orientation can be used to suppress experimental fluctuations.

As with any matrix inversion, the experimental error for the lattice strain measurements influences the inversion of SPF data for the LSDF. Investigation of the rank of $\mathbf{\Gamma}(\mathbf{R})$ focuses on the mapping between the LSDF and the SPF data,

and should be used as a guide to determine which measurement directions best probe orientation space. If sufficient measurements are made for the rank of $\Gamma(\mathbf{R})$ to be six for each orientation, the validity of the inversion results will still be directly linked to the experimental error for each measurement.

1.7 Summary/Conclusions

Investigations of the manner in which the stress is distributed over the orientations within a loaded aggregate, and the microscale elastic-plastic deformation in general, have the potential to advance our understanding of crystal scale material response. Instead of manufacturing test specimens on the size scale of the microstructure, our approach has been to “observe” mechanical tests with high energy x-rays. Measurement of lattice Strain Pole Figures (SPFs) provides a robust technique for quantifying the three dimensional micromechanical state within a polycrystalline sample. The penetration of high energy x-rays combined with the availability of x-ray area detectors enables the collection of enormous volumes of lattice strain data from specimens loaded *in situ*. Conventional approaches developed for the limited number of scattering vectors used in neutron diffraction experiments do not utilize these potentially massive data sets that can be generated. With access to more independent lattice strain measurements, developing the means to quantitatively compare sets of lattice strain data is paramount. Therefore, the focus of this work was to bring the SPF experiment to the level of a measurement capability as opposed to a one-off style experiment. Exploration of the experimental technique employed results for a nickel base superalloy, Low Solvus High Refractory (LSHR).

The interconnected nature of the SPF coverage and the regions of orientation space probed were discussed following the analogy of applying resistance type strain gages to a sample; where each measurement represents the orientation averaged normal strain in the direction of the crystallographic fiber. Key findings include:

- Each data point on an SPF corresponds to the peak shift from an individual x-ray diffraction experiment. The set of orientations within a polycrystalline aggregate that are interrogated by each measurement are predictable from the details of the x-ray experiment configuration, the x-ray wavelength, and the material characteristics. These orientations lie along a crystallographic fiber in orientation space. A fiber is defined by a sample direction, relative to LD, TD, and ND, and a crystal direction indicated by the lattice plane normal ($\{hkl\}$).
- Due to crystal symmetries and the set of $\{hkl\}$ s observed, the maximum number of potential fibers that can interrogate each orientation within a polycrystal is finite. For the FCC LSHR, we observed the $\{111\}$, $\{200\}$, $\{220\}$, and $\{311\}$ lattice planes and the total number of fibers that can probe each orientation is equal to one-half the sum of multiplicity for each $\{hkl\}$. This results in a maximum of 25 fibers per orientation. Measurement of several $\{hkl\}$ s for the same SPF coverage greatly increases the number of independent fibers that interrogate each orientation.
- A finite element discretization of orientation space provided a list of orientations at which the fibers, produced from the SPF data, could be investigated. The actual number of fibers accessible for each orientation depends on the SPF coverage, which, in turn depends on the experimental configuration. The orientation space sampling matrix, $\mathbf{\Gamma}(\mathbf{R})$, comprises the di-

rection information for each fiber that probes an orientation, \mathbf{R} . The rank of $\mathbf{\Gamma}(\mathbf{R})$, which also varies over orientation space, is an important quantity related to SPF inversion. If the rank of $\mathbf{\Gamma}(\mathbf{R})$ is six at every orientation, SPFs can be inverted directly for the lattice strain distribution function.

- The rank of $\mathbf{\Gamma}(\mathbf{R})$ can be used to optimize the selection of diffraction measurements for the SPF experiment and prescribe experiment conditions. Sets of lattice strain measurements can be quantitatively compared, allowing for the SPF micromechanical experiment to be optimized prior to making a measurement at the x-ray beam line. In particular, the rank of $\mathbf{\Gamma}(\mathbf{R})$ can be used in the selection of SPF coverage and the $\{hkl\}$ s that best probe orientation space.
- SPFs from LSHR depict lattice strains that are consistent with the relative stiffness between $\{hkl\}$ s for measurements in the loading direction. SPF data fill a critical role in corroborating crystal-based mechanics simulations and bolster investigations of the mechanical response at the crystal scale. This work represents an important step in the process of standardizing the SPF experiment in order to better understand the ‘quality’ of the data.

ACKNOWLEDGEMENTS

The financial support for this work was provided by the Air Force Office of Scientific Research (AFOSR) under Grant No. FA9550-06-1-0168, Dr. Jaimie Tiley program manager. The diffractometer/loadframe was funded by the Defense University Research Instrumentation Program (DURIP) under Grant No. F49620-03-1-0322, Dr. Craig Hartley program manager. The LSHR material was provided by Dr. Todd J. Turner of the Materials Directorate, Air Force Research Laboratory (AFRL). The authors wish to thank Professor Paul Dawson and Donald Boyce for their insightful comments. The finite element representation of orientation space employed, and tools to identify the orientations that are represented by a fiber, are part of a software package generated by Donald Boyce (deb14@cornell.edu). The package has several example problems and is available upon request. This work is based upon research conducted at the Cornell High Energy Synchrotron Source (CHESS) which is supported by the National Science Foundation under NSF award DMR-0225180.

CHAPTER 2
QUANTIFYING THE UNCERTAINTY OF SYNCHROTRON-BASED
LATTICE STRAIN MEASUREMENTS

2.1 Introduction

Investigations into stress driven mechanisms at the crystal scale within a polycrystalline sample, such as those active during fatigue crack initiation, are limited by the lack of experimental data at the relevant length scale. Diffraction-based experiments employing *in situ* mechanical loading that isolate the mechanical response of subsets of crystals within the deforming aggregate can provide insight into the stress state at the crystal length scale [9, 12, 16, 22, 38, 48, 49, 64]. Variation of the stress state (magnitude and direction) from one crystal orientation to the next is a key finding from these experiments [5, 49]. Such stress distribution information can prove to be extremely valuable for validating crystal scale modeling frameworks [49]. Experimental uncertainty is one glaring question that arises whenever comparisons to simulation are made, however. An essential step present in many lattice strain measurement experiments is the approximation of experimental error or “noise” by measuring the apparent lattice strains present in an unconsolidated sample constructed of a powder with precisely measured lattice parameters. Because this standard sample is completely strain free, the difference between the measured lattice spacing and the theoretical values computed using the precise lattice parameters can be used to establish the “error bar” associated with the experiments. A value typically cited in the recent neutron and x-ray literature is on the order of $\pm 100\mu\epsilon$ ($\pm 1 \times 10^{-4}$) [5, 10, 12, 40, 48, 63]. While a necessary component of a modern

diffraction experiment, this single measure of error (sometimes stated as resolution) fails to account for all the possible variation in uncertainty that can take place over the broad ranges of scattering vectors and families of crystallographic planes that we see in these experiments. Nor is this error a true uncertainty value since it is not typically associated with a specific confidence interval.

In this paper, we present a comprehensive definition of lattice strain uncertainty and a detailed description of its determination. We propose an expression that separates the uncertainty into a set of approximately orthogonal components: one associated with the **instrument** being used to make the measurement and another that considers the **material** under investigation. Since the instrument component is present regardless of material, it is the focus of the paper. We use experimental data from lattice Strain Pole Figure (SPF) experiments [48] conducted using at two distinct facilities: the A2 experimental station at the Cornell High Energy Synchrotron Source (CHESS) and beam line 1-ID-C at the Advanced Photon Source (APS). Two types of area x-ray detectors were employed. At CHESS, a MAR345 online image plate was used and a GE 41RT amorphous silicon detector was employed at APS. The data sets from these experiments provide the basis for developing a model that can be used to estimate the instrument portion of the uncertainty using apparent strains measured from a calibrant sample. We employed cerium dioxide (CeO_2) powder with a well documented lattice parameter of 5.411\AA . The paper begins with a short diffraction primer and an overview of the lattice SPF experiment. The next sections will introduce the lattice strain uncertainty, with the focus on the instrument portion of the uncertainty and the contributing sources of error. The key result is a procedure for determining the instrument portion of the lattice strain uncertainty for a given set of instrument conditions.

2.2 Background

Prior to introducing the experimental technique it is advantageous to establish some basic terminology using the conventions established in [25]. A source of experimental error leads to the measured value being offset from the true value. There are two classes of error, systematic and random. A systematic error limits the accuracy of the experiment by creating a bias in the data. Random errors contribute to the precision limit for each measurement. The uncertainty is a precision interval which represents the probable range, for a fixed degree of confidence, about the measured value in which the true value is expected to occur. The uncertainty for each measurement accounts for the convolution of the different sources of error. Resolution is the smallest measurement possible with a detector and establishes the minimum resolvable lattice strain.

A typical diffraction experiment conducted in transmission is shown in Figure 2.1. Instead of tracking individual crystals within the aggregate, the diffraction experiments described here interrogate an undifferentiated aggregate of crystals - a so called powder experiment [48]. The diffraction data corresponds to a typical material point. The relevant quantities for the experiment are the scattering vector, s , which is the bisector of the incoming and diffracted x-ray and the Bragg angle, $\theta_{\mathbf{c}||s}$, which is half the angle between the transmitted and diffracted x-ray. The subscript $\mathbf{c}||s$ indicates the specific diffraction measurement where \mathbf{c} is the plane normal for the crystallographic family ($\{hkl\}$) that is diffracting and the scattering vector, s . The diffraction condition for each measurement is defined by Bragg's law as,

$$n\lambda = 2d_{\mathbf{c}||s} \sin \theta_{\mathbf{c}||s} \quad (2.1)$$

where n is an integer, λ is the x-ray wavelength, and $d_{\mathbf{c}||s}$ is the lattice plane

spacing [17]. The energy is related to the wavelength by,

$$E = \frac{hc}{\lambda} \quad (2.2)$$

where h is Plank's constant and c is the speed of light.

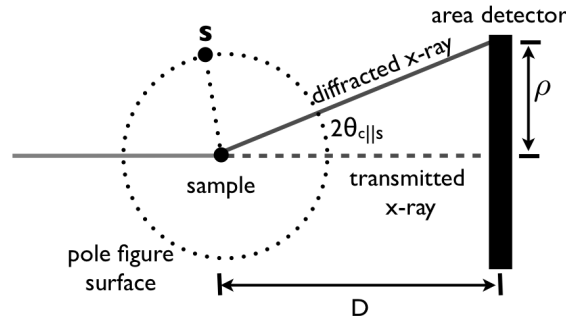


Figure 2.1: Schematic of a diffraction experiment conducted in transmission. Here D and ρ are the sample to detector distance and the radial distance on the detector, respectively.

Each lattice strain measurement corresponds to a radial (ρ) shift of a diffracted peak on the detector (referred to as a peak shift) and is defined using Equation 2.1 as,

$$\epsilon_{c||s} = \frac{d_{c||s} - d_{c||s}^0}{d_{c||s}^0} = \frac{\sin \theta_{c||s}^0}{\sin \theta_{c||s}} - 1 \quad (2.3)$$

Strain is measured relative to an initial or unstrained state of the material designated with the superscript 0. These values can be calculated using either the lattice parameter of the material or, for unstrained samples using *in situ* loading, the lattice spacing at zero load.

2.2.1 The Lattice Strain Pole Figure (SPF) Experiment

The SPF experiment employs high energy x-ray diffraction to quantify lattice strains in many directions for polycrystalline materials [5, 6, 48, 49, 56]. The

enormous number of distinct lattice strain measurements is the salient feature of this technique. The lattice strain data are plotted on pole figures to convey the orientation of the strain measurement relative to the directions of the specimen. To construct an SPF for a specific $\{hkl\}$, each measurement is plotted at the intersection of a unit sphere, representing the pole figure surface, and the scattering vector, as shown in Figure 2.1.

By reorienting the sample relative to the x-ray beam, different crystals in the aggregate are interrogated and the pole figures are populated. This experiment is often combined with *in situ* loading such that SPFs are measured at many points in the deformation history to quantify the evolving micromechanical state of the material. At a desired point in the deformation history we reduce the load slightly to mitigate creep effects and make a series of diffraction measurements that populate the pole figures [19]. An example of a lattice SPF for a nickel-based superalloy measured at a macroscopic stress of 720 MPa in uniaxial tension is shown in Figure 2.2. As expected, the largest tensile values of the lattice strain occurs near the loading direction, with compressive strains in the transverse direction consistent with the Poisson effect.

The use of a calibrant powder is a key aspect of our SPF experiment procedure. We fix an x-ray transparent container containing the unstrained calibrant powder (calibrant insert) to the sample. A schematic depicting the sample and calibrant insert relative to the components that make up the x-ray beam path is shown in Figure 2.3. Diffraction data from the calibrant are used to assess the instrument portion of the lattice strain uncertainty and to monitor the experiment geometry. More on the experimental procedure and illustrations can be found in [5, 6, 48, 49, 56]. The importance of fixing the calibrant insert to the deforming

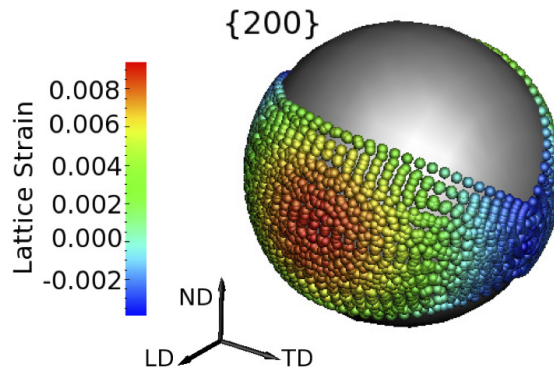


Figure 2.2: The {200} lattice SPF measured at a uniaxial macroscopic stress of 720 MPa for a nickel-based superalloy - Low Solvus High Refractory (LSHR). The coordinate system is relative to the sample and the directions are the Loading Direction (LD), the Transverse Direction (TD), and the Normal Direction (ND) [56].

sample for ensuring high fidelity results will be discussed in Sect. 2.5.

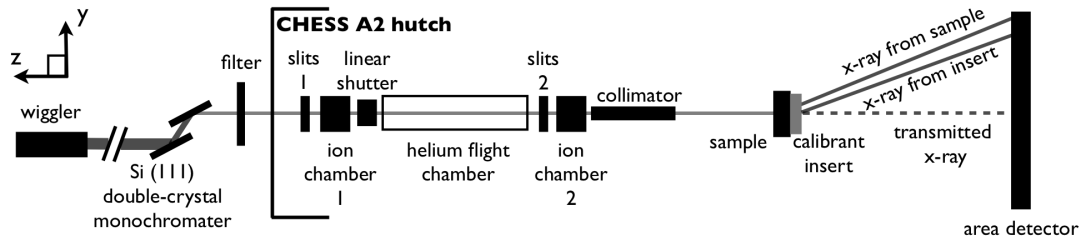


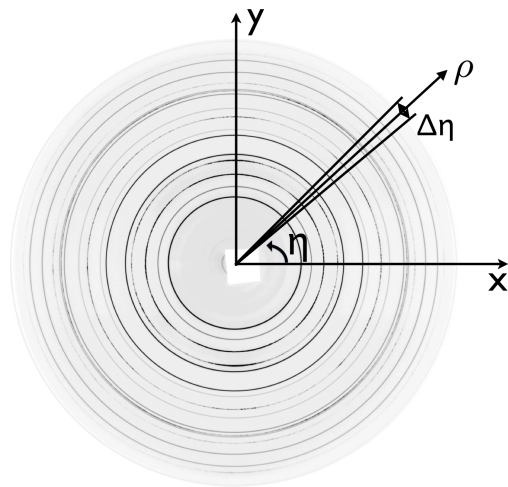
Figure 2.3: Schematic of the components that make up the x-ray beam path for the experiment conducted at CHESS. The monochromator isolates a single x-ray energy to within 50 eV, the slits define the cross section of the incoming x-ray beams, and the flight chamber and the collimator are used to minimize the scatter from sources other than the sample. The experiment conducted at the APS employed a similar arrangement of components along the x-ray beam path.

2.2.2 Diffraction Data

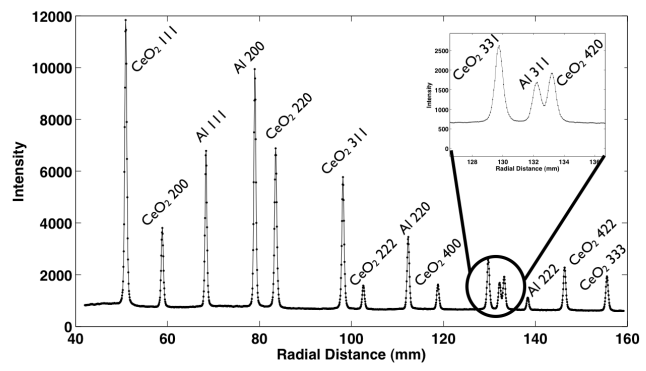
A typical diffraction pattern from a 7075-T6 aluminum sample with a CeO_2 calibrant insert fixed to its surface is shown in Figure 2.4(a). Since thousands of crystals are interrogated simultaneously in the SPF experiment, the diffraction data are complete Debye rings. A typical x-ray area detector is composed of discrete regions or pixels, which are distributed in a rectangular array. Diffraction data are discrete intensity values which represent the intensity measured by the individual pixel areas.

To more easily take advantage of the circular shape of the rings, the intensity data are mapped from the rectangular coordinates of the detector to polar coordinates. A pattern center is established, then each point on the detector can be represented by a radial distance (ρ) and an azimuthal angle (η). Each diffraction pattern is then sectioned into radial ($\Delta\rho$) and azimuthal bins ($\Delta\eta$) which are integrated to produce arrays of radial positions versus intensities for each azimuthal bin, such as the one shown in Figure 2.4(b) for the $\Delta\eta$ highlighted in Figure 2.4(a). The objective of the data reduction methodology is to identify the radial positions of the diffracted peaks on the area detector and, using the experiment geometry shown in Figure 2.1, calculate $2\theta_{\text{c}|\text{s}}$ for each peak. Each $2\theta_{\text{c}|\text{s}}$ value, therefore, corresponds to the most likely plane spacings for the crystals that contribute to the intensity distribution that makes up the peak. These $2\theta_{\text{c}|\text{s}}$ values are used to calculate lattice strains and are represented as discrete points on the SPFs.

The integration of the intensity for each bin (defined by $\Delta\rho$ and $\Delta\eta$) can be easily performed numerically using finite elements - this is one of the strengths of the method. While a number of discretization and rebinning schemes have



(a)



(b)

Figure 2.4: (a) Typical diffraction pattern measured with the MAR345 area detector at CHESS for an aluminum sample with a CeO_2 calibrant insert fixed to the sample. (b) The array of radial positions versus intensities for the highlighted azimuthal bin in (a). A region of the array is selected to indicate the similar characteristics of the calibrant and aluminum peaks.

been proposed and used extensively, the use of finite elements to discretize the detector surface is extremely straight forward. A brief overview of the application of finite elements for processing area detector data will be provided here; a more complete discussion is available in [14]. A schematic of a detector is shown in Figure 2.5(a) with both radial and azimuthal bins overlaid on a square grid representing the pixel array on the area detector. Here the inner and outer rings bound the region of interest on the detector. The center of each pixel is treated as a node and assigned the value of the pixel intensity. The nodes are grouped to form triangular elements over which the intensity is allowed to vary. Using linear interpolation functions we calculate the intensity at any point on the detector as a function of the nearest nodes (pixel values). An example of two triangular elements defined by four pixels is shown in Figure 2.5(b). Each pixel has coordinates defined (p_i^x, p_i^y) , where the subscript i indicates the pixel number. The use of an isoparametric map (mapping that employs the same interpolation functions as used for the intensity) allows for any point within an element, labeled 'A' in Figure 2.5(b), to be related to a position within a reference element (triangle with unit length sides) with coordinates defined (ξ, β) [14]. This relationship is expressed by,

$$p_A^x = p_1^x \xi + p_2^x \beta + p_3^x (1 - \xi - \beta) \quad (2.4)$$

$$p_A^y = p_1^y \xi + p_2^y \beta + p_3^y (1 - \xi - \beta) \quad (2.5)$$

By solving these equations for ξ and β , we can calculate the intensity at point 'A' using linear interpolation,

$$I_A = I_1 \xi + I_2 \beta + I_3 (1 - \xi - \beta). \quad (2.6)$$

Using the interpolation functions we define new triangular elements that exactly represent the bin geometry as shown for a single azimuthal bin in Figure 2.6. The integration can now be performed using numerical quadrature to

generate an array of radial positions versus intensities for each azimuthal bin [14].

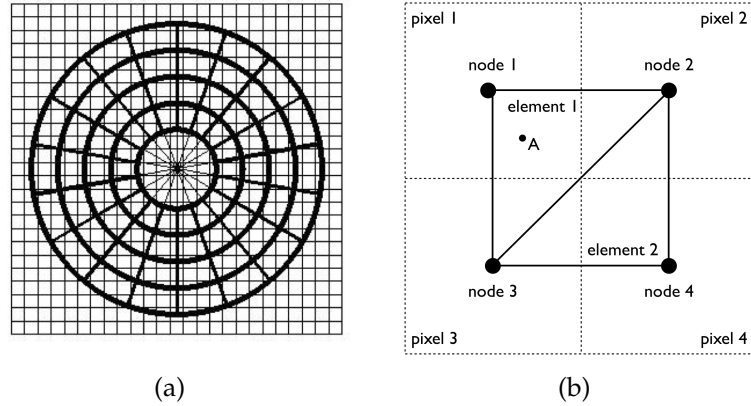


Figure 2.5: (a) Schematic of an area detector with four radial and eighteen azimuthal bins overlaid. (b) Two triangular elements defined by four pixels. The intensity value at any point 'A' within the element can be calculated using the neighboring nodal point values and the linear interpolation functions.

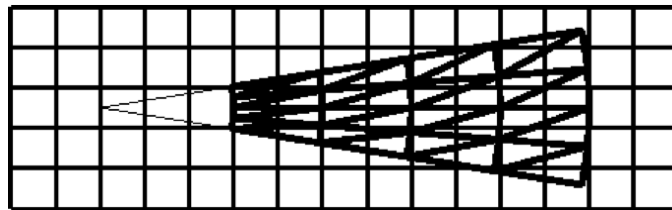


Figure 2.6: Schematic of a grid of square pixels is shown with a single azimuthal bin defined with triangular elements overlaid.

To extract quantitative information about the diffracted peaks from each array of radial positions versus intensities the data are represented by the superposition of a smoothly varying background function and an analytic peak profile function for each diffracted peak [5]. The information within each peak fit provides the position, intensity, and width of the diffracted peak on the detector.

A common peak profile function used to represent synchrotron diffraction

data is the pseudo-Voigt analytic peak profile function, which combines Gaussian and Lorentzian peak shapes using the rule of mixtures [5, 72],

$$y^{pV}(2\theta) = S(wG(2\theta) - (1 - w)L(2\theta)). \quad (2.7)$$

Here S scales the function to match the measured intensity and w is a mixing parameter to balance the Gaussian and Lorentzian contributions in G and L respectively. The Gaussian and Lorentzian functions are defined as,

$$G(2\theta) = \exp\left(-\frac{(2\theta - 2\theta_*)^2}{2\kappa^2}\right) \quad (2.8)$$

and

$$L(2\theta) = \frac{\left(\frac{\Lambda}{2}\right)^2}{\left(\frac{\Lambda}{2}\right)^2 + (2\theta - 2\theta_*)^2} \quad (2.9)$$

where $2\theta_*$ is the peak position and κ and Λ specify the width of the peak. The calculated spectrum is defined as,

$$y^{cal} = p^d + \sum_{i=1}^N y_i^{pV} \quad (2.10)$$

where p^d is a smoothing varying background function - often a polynomial, and N is the number of diffracted peaks ($\{hkl\}$ s). The peak positions are found by iterating the fit parameters to minimize the difference between the observed intensity, y^{obs} , and the calculated intensity, y^{cal} ,

$$R_y = \sum_{i=1}^b (y_i^{obs} - y_i^{cal})^2 \quad (2.11)$$

The number of data points used in this minimization, b , is established by the number of radial bins employed during the integration.

2.3 Lattice Strain Uncertainty

The uncertainty for each lattice strain measurement is represented as $\epsilon_{\text{c||s}} \pm U_{\text{c||s}}$. There are many sources of error which can cause the measured lattice strain value to deviate from the true value. We have elected to approximate the total uncertainty in a traditional format [25],

$$U_{\text{c||s}} = \sqrt{U_{\text{c||s}}^i{}^2 + U_{\text{c||s}}^m{}^2 + \dots} \quad (2.12)$$

This formulation is advantageous since the dominant contributions to the uncertainty can be explicitly represented, while leaving the possibility for additional influences to be quantified as the experiment evolves. The instrument, in the context of the lattice strain uncertainty, encompasses the experimental conditions and the procedure employed to reduce the data. In short, the instrument represents all aspects of the experiment that influence the measurement of diffracted peak positions on the area detector. The term $U_{\text{c||s}}^i$ constitutes the minimum lattice strain uncertainty for an experimental configuration and will be investigated in the subsequent sections.

The most significant source of error that contributes to $U_{\text{c||s}}^m$ is related directly to the number of crystals probed by each measurement. Each lattice strain measurement in an SPF experiment amounts to a statistical sampling problem. The diffraction measurement probes a subset of the irradiated crystals that satisfy the diffraction condition (Bragg's law in Equation 2.1). This subset is unique to the sample, and the resulting lattice strain value is the mean for all the crystals satisfying the c||s combination. Since the goal of the SPF experiment is to measure the true lattice strain value for the subset of orientations probed by each measurement, it is necessary to probe a statistically significant number of crystals. Determining $U_{\text{c||s}}^m$ for each measurement is coupled to the number

of diffracting crystals, the grain morphology, and the variation in the lattice strains between the diffracting crystals. The probable number and morphology of the crystals can be addressed using microstructure characterization techniques, such as Electron Back Scatter Diffraction (EBSD). Without measuring strains in each individual crystal that satisfies the Bragg condition, the statistical lattice strain variance for each $c||s$ combination cannot be determined. To avoid the uncertainty due to statistical sampling errors, the SPF experiment has been restricted to materials where the number of diffracting crystals is large enough, several hundred to thousands for each measurement, such that the measured lattice strain value can be assumed to be the true lattice strain value. Application of experiments to measure lattice strain for a broader range of materials require that $U_{c||s}^m$ be determined and is the focus of ongoing work.

Another potential source of error that contributes to $U_{c||s}^m$ is the ambiguity of overlapping diffracted peaks. Diffraction data are the superposition of the x-ray intensity that reaches the detector. Consider the highlighted portion of the diffracted spectra in Figure 2.4(b). Identifying the the exact peak position of the {311} aluminum peak is dependent on separating the contribution to the intensity from the different peaks. As stated in [5, 6], this problem could be addressed by incorporating a model for strain as function of crystal orientation into the Rietveld technique [72], but currently such models are not available for use.

2.3.1 Instrument Contribution ($U_{\mathbf{c}||\mathbf{s}}^i$)

The instrument contribution to the lattice strain uncertainty arises from several sources of error including the integration method employed to transform the raw data to diffraction spectra, the identification of diffracted peak positions, the model for the relationship between the sample and detector, and the experimental conditions employed. To investigate the instrument portion of the lattice strain uncertainty we conducted the SPF experiment on a CeO_2 calibrant powder specimen using the two sets of experimental conditions shown in Table 2.1. The pertinent characteristics of the detectors employed are shown in Table 2.2. A key difference between the two detectors is the type of readout mechanism employed. A more detailed discussion of the detector hardware is provided in [40]. The range of sample directions interrogated for the CHESS experiment corresponds to the coverage shown for the SPF in Figure 2.2. The SPF coverage employed for the APS experiment corresponds to a series of sample rotations about a vertical axis between -60° and 60° in 2.5° increments. At 0° the sample was normal to the incoming x-rays. A total of 17280 and 31752 unique lattice strain measurements were made for the CHESS and APS experiment, respectively. These massive data sets enable a statistics-based approach for quantifying the uncertainty. This marks an important shift from an uncertainty estimated from a single event, to that calculated from an ensemble.

Each diffraction measurement can be used to determine the mean lattice strain for the crystals satisfying the diffraction condition. A set of diffraction measurements, therefore, constitutes a set of mean values. If a series of identical diffraction measurements (same $\mathbf{c}||\mathbf{s}$ combination) were made, each from an independent sample, then from the central limit theorem in statistics we expect

Table 2.1: The experimental conditions used in the two experiments.

Experiment	Energy (KeV)	D(mm)	Beam Size(μm^2)	η (#, deg. incr.)
CHESS	49.989	≈ 650	500×500	$72, 5^\circ$
APS	90.500	≈ 1450	250×250	$72, 5^\circ$

Table 2.2: The characteristics of the area detectors employed.

Experiment	Detector	Size	Pixel Size (μm^2)
CHESS	MAR345	345 mm diameter	100×100
APS	GE 41RT	$409.6 \times 409.6 \text{ mm}^2$	200×200

the set of lattice strains to approximate a normal distribution [24]. If a set of measurements follow a normal distribution, then the uncertainty can be determined from the standard deviation of the measurements and a scaling factor for the degree of confidence [25],

$$U_{\mathbf{c}||\mathbf{s}}^i = t\phi_{\mathbf{c}||\mathbf{s}}. \quad (2.13)$$

For 95% confidence $t = 1.96$ and corresponds to 95% of the area under a standard normal curve [25]. Here $\phi_{\mathbf{c}||\mathbf{s}}$ is the standard deviation of the repeated lattice strain measurements (same $\mathbf{c}||\mathbf{s}$ combination, but independent samples). It is currently not possible to determine $\phi_{\mathbf{c}||\mathbf{s}}$ for each measurement, but there should be absolute commonality between lattice strains for each $\{hkl\}$ measured on a calibrant sample,

$$U_{hkl}^i = t\phi_{hkl}. \quad (2.14)$$

The lattice strain distributions for each $\{hkl\}$ are shown in Figure 2.7 and Figure 2.8. Each distribution is expected to be both centered about zero and

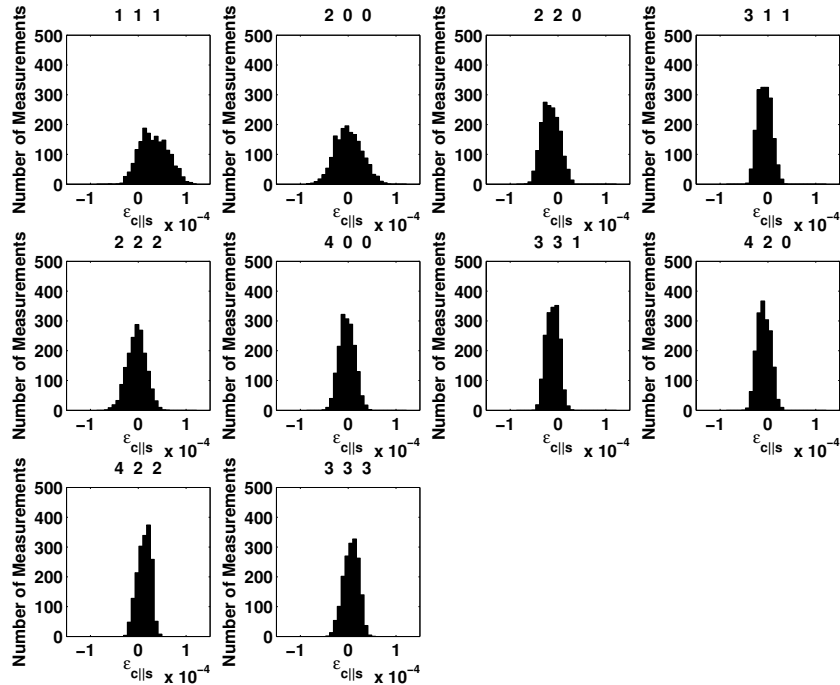


Figure 2.7: CeO₂ lattice strain distributions are shown for each $\{hkl\}$ for the experiment conducted at CHESS. Though each measurement pertains to a specific $c||s$ combination, to investigate the instrument portion of the uncertainty data for each $\{hkl\}$ are grouped together.

follow a normal distribution. The mean of the mean lattice strains for each $\{hkl\}$ was found for both experiments to be 3.8×10^{-7} and 4.6×10^{-7} , respectively. The standard deviation of the means for the lattice strain distributions was 1.4×10^{-5} and 3.0×10^{-6} , respectively. The largest deviation from zero a single lattice strain distribution occurred for the $\{111\}$ lattice strain distribution in Figure 2.7. This offset is due to an artifact in diffraction data near the center of the pattern which is associated with the sample holder. This issue will be explored more in Sect. 2.3.1.

From statistics we know the skewness and kurtosis of a normal distribution

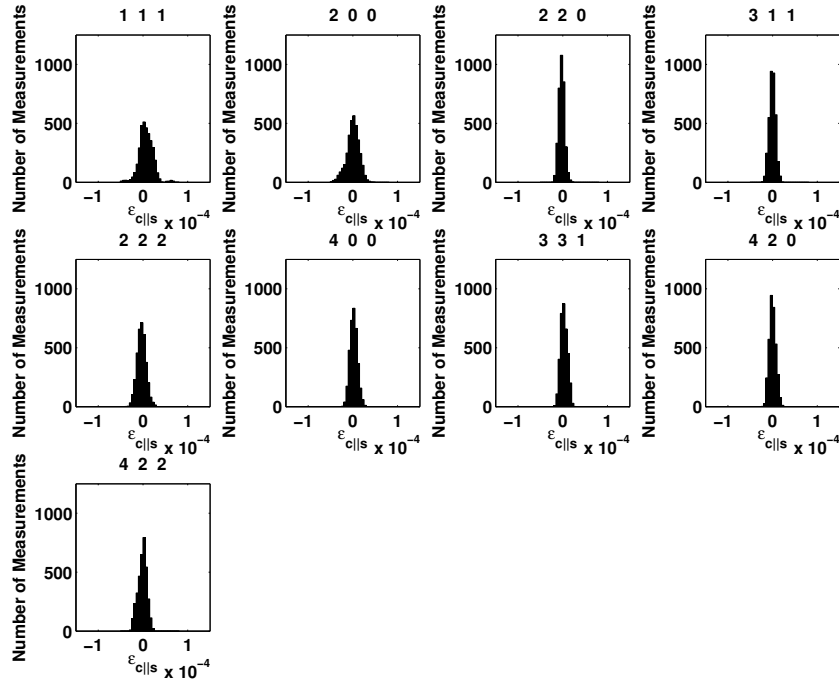


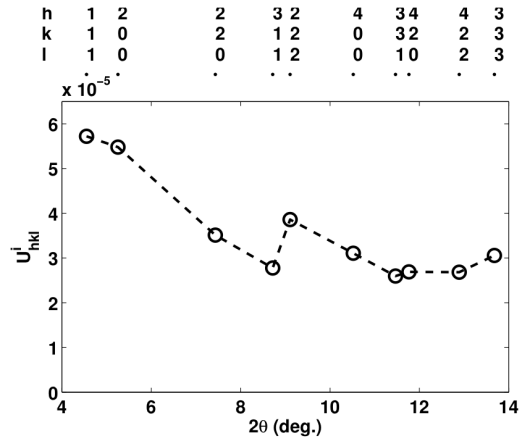
Figure 2.8: CeO₂ lattice strain distributions are shown for each $\{hkl\}$ for the experiment conducted at the APS.

to be 0 and 3, respectively [24]. The average skewness for the lattice strain distributions in Figure 2.7 and Figure 2.8 was found to be 0.007 and 0.03, respectively. The average kurtosis for each experiment was 2.6 and 3.2, respectively. Using the χ^2 goodness of fit test [24], which estimates the likelihood that a set of measurements is from a normal distribution, we found that all but one of the lattice strain distributions for each $\{hkl\}$ were normal to within 95% confidence. The $\{222\}$ for the experiment conduction at CHESS (Figure 2.7) was determined to be normal to within 90% confidence. This reduction in confidence for the $\{222\}$ will be addressed in Sect. 2.3.2.

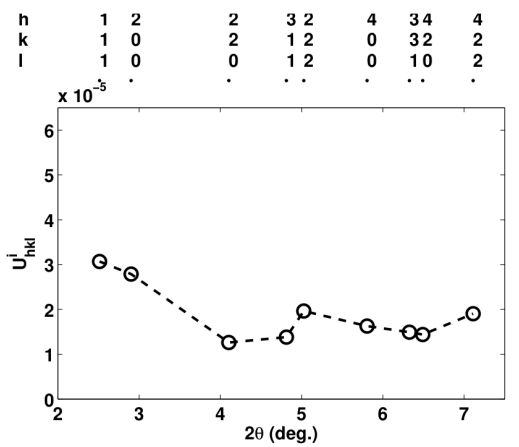
The application of Equation 2.14 to the data presented in Figure 2.7 and Figure 2.8 is shown in Figure 2.9. Both sets of U_{hkl}^i values are significantly smaller

than the previously quoted values of $\pm 1 \times 10^{-4}$. The variations between the different $\{hkl\}$ s shown in Figure 2.9 appear qualitatively similar for both instruments. The difference in the U_{hkl}^i values between the CHES and the APS experiments is most likely due to the sharp difference in the detector readout mechanisms. These results clearly demonstrate that a single value for the instrument portion of the uncertainty is inadequate for experiments interested in the subtle evolution of the crystal stress state during deformation. In addition, diffraction from a material of interest will inherently produce diffracted data that differ from the calibrant. Therefore, quantifying U_{hkl}^i for each calibrant $\{hkl\}$ provides insight into possible uncertainty values, but is insufficient to determine the instrument uncertainty for lattice strain measurements on materials other than the calibrant. Moreover, the discontinuity in U_{hkl}^i between the $\{311\}$ and $\{222\}$ results for both experiments indicates that interpolation between the different U_{hkl}^i values may lead to erroneous results.

To accurately estimate the instrument portion of the uncertainty we developed a model, defined U_{hkl}^{i*} that is capable of reproducing the uncertainty values measured for the calibrant shown in Figure 2.9. This model assumes that systematic contributions to the instrument uncertainty are minimized, and that the uncertainty is governed by the resolution of the position and intensity measurements using the detector. Application of U_{hkl}^{i*} to the measured uncertainties for each calibrant $\{hkl\}$ allows for the model parameters to be determined and used to estimate the instrument portion of the uncertainty for other materials of interest. Prior to outlining U_{hkl}^{i*} and the connection to the lattice strain resolution, we will introduce the dominant sources of experimental error.



(a)



(b)

Figure 2.9: The measured lattice strain uncertainty for each CeO_2 $\{hkl\}$ are shown for the experiments conducted at (a) CHES and the (b) APS. Each data point corresponds to the $\{hkl\}$ indicated at the top of the figure.

Integration Parameters

As described in Sect. 2.2.2, the data reduction procedure begins with converting each diffraction pattern to polar coordinates. The data within each bin are integrated using finite elements to generate arrays of radial positions versus intensities like the array shown in Figure 2.4. The use of finite elements for performing the integration adds a degree of smoothing to the measured data.

The abrupt intensity changes between pixels is the result of measuring intensity over the finite area of each pixel. It is probable that the actual intensity varies smoothly within and between pixels, but due to the discrete pixel values, the diffraction pattern is distorted. As such, the smoothing introduced by the finite elements is not detrimental to the results.

Selection of the parameters such as the size and number of triangular elements used to represent each bin ($\Delta\rho$, $\Delta\eta$) have the potential to contribute to the instrument portion of the uncertainty. To avoid numerical errors during the integration process the aspect ratio of the elements employed to represent the azimuthal bin geometry, as shown in Figure 2.6, are typically constrained to less than 4:1 (ratio of the base to height of the element). The maximum number of elements employed is limited by the computational requirements. The element size should be selected such that the constraint on the aspect ratio is satisfied, but additional discretization does not greatly improve the results.

Diffracted Peaks Identification

The discrete points resulting from the integration described above are difficult to employ as a spectrum. Therefore, a smooth curve is often 'fit' to the data. Fitting diffracted peaks during the data reduction procedure contributes to the instrument uncertainty in several ways. The quality of the fit is proportional to the magnitude of R_y (Equation 2.11) and is a source of error that contributes to the instrument uncertainty. The fit is an important quantity that represents both the analytic profile function and the treatment of the background data. As previously stated, diffraction data are the superposition of any x-rays that reach the sample. Spurious x-rays from sources other than the sample (components

along the beam path, air, etc.) contribute to the background on the detector. The scaling parameter S is an indicator of the measured intensity above the background and is coupled to the resolution of diffracted peak positions. The uncertainty in the measured peak positions increases as the scaling parameter S approaches zero; indicating that there is no longer sufficient diffracted signal to identify a peak.

Often the most pronounced contribution to the background occurs near the center of the diffraction pattern. For these experiments the grips that hold the sample within the loadframe absorb x-rays and produce a visible contrast pattern in the background signal. These sharp changes in the background are an insidious effect that can lead to low R_y values, while the peak position is offset significantly. It is probable that the slight offset of the {111} lattice strain distribution from a mean value of zero, shown in Figure 2.7, is due to this effect.

Modeling the Experiment Geometry

As described in Sect. 2.2, a lattice strain accompanies a radial shift of the intensity on the detector. As described in detail in [5], the accuracy of the conversion of a radial shift to a lattice strain depends on how the detector is aligned with the x-ray beam. The model for the experiment, referred to as the geometric model, is used to correct for the detector not being centered or orthogonal with respect to the incoming x-ray. This model consists of two parameters for the detector center (c_x, c_y), two detector tilts, D , and a distortion correction for the detector (ρ^*). The distortion correction addresses the systematic error with the detector due to the arrangement of pixels, the readout mechanism, and the electronics. Different corrections have been used for each of the detectors considered. The

Table 2.3: Parameters for the distortion correction for the GE 41RT detector published in [40].

a_1	a_2	n_1	n_2	ρ_d
-3.174×10^{-5}	-2.595×10^{-4}	3.111	2.295	204.8

MAR345 distortion correction is a constant radial shift [5],

$$\rho^* = \rho + \rho_0 \quad (2.15)$$

where ρ^* is the undistorted radial positions and ρ_0 is a constant. Typically ρ_0 shifts the data by much less than a pixel. The distortion correction used for the GE 41RT amorphous silicon detector is more complicated [40],

$$\rho^* = f\rho \quad (2.16)$$

$$f(\rho, \eta) = a_1 \left(\frac{\rho}{\rho_d} \right)^{n_1} \cos(4\eta) + a_2 \left(\frac{\rho}{\rho_d} \right)^{n_2} + 1 \quad (2.17)$$

Typical values for a_1 , a_2 , n_1 , n_2 , and ρ_d presented in [40] are shown in Table 2.3.

A short overview of the implementation of the geometric model will be provided here, but a more complete discussion is given in [5]. Implementation of the geometric model begins with a very precise understanding of the lattice parameters of the calibrant material. The difference between the expected calibrant peak positions and the measured peak positions for several calibrant peaks, over a range of Bragg angles, are minimized by adjusting the parameters of the geometric model (c_x , c_y , detector tilts, D , and ρ^*). To determine the optimal geometric model parameters a nonlinear least squares optimization routine is utilized. Each iteration of the optimization involves a slight perturbation of the model parameters, a remapping of the data, and the identification of the new peak positions to be used in calculating the difference between the expected and measured Bragg angles.

The geometric model maps the entire diffraction pattern from the initial to ‘corrected’ positions and, as such, has immense potential to impact the lattice strain uncertainty. After implementation there are two common sources of error that remain. First, employing a nonlinear optimization process to determine the ‘best’ possible set of model parameters is initial guess dependent. Currently the software package Fit2D is used to generate an initial guess [29]. The second common source of error is a systematic failure of the model to represent the detector; for instance an incomplete or inaccurate distortion correction that introduces a bias to the measured lattice strains.

Lattice Strain Resolution / Experimental Conditions

Since each diffraction pattern is represented by pixels with specific **position** and **intensity** values, the resolution of the lattice strain measurements is linked to these quantities. More explicitly, the resolution for the lattice strain measurements is defined by the smallest resolvable change in the position of a diffracted peak and the intensity required to identify diffracted peak positions on the area detector. The smallest resolvable change of a single point on the detector is governed by the detector point spread function. Each diffracted peak spans many pixels (≈ 20) in the radial direction and can be seen in Figure 2.4(b). Since each peak is fit with an analytic function, it is possible to resolve changes in the peak position that are much less than a pixel. If the sources of error contributing to each lattice strain measurement are minimized, then the instrument portion of the uncertainty will approach a limit established by the resolution.

The experimental conditions that most influence U_{cls}^i are the sample to detector distance (D), the x-ray energy, and the size of the x-ray beam cross section.

To investigate the influence of these parameters on the lattice strain uncertainty, we define the smallest resolvable peak shift to be $\delta\rho_{min}$. Using Equation 2.3, the geometric relationship $2\theta = \arctan(\frac{\rho}{D})$, and all radial positions on the detector, and not just an exact measurement indicated by a $\mathbf{c}||\mathbf{s}$, we can write a continuous function for the minimum resolvable lattice strain using $\delta\rho_{min}$,

$$\epsilon_{min} = \frac{\sin(\frac{\arctan(\frac{\rho}{D})}{2})}{\sin(\frac{\arctan(\frac{\rho-\delta\rho_{min}}{D})}{2})} - 1. \quad (2.18)$$

The minimum resolvable lattice strain, ϵ_{min} , is shown in Figure 2.10 for three different values of $\delta\rho_{min}$ using the experimental conditions employed for the CHESS experiment (shown in Table 2.1 and Table 2.2).

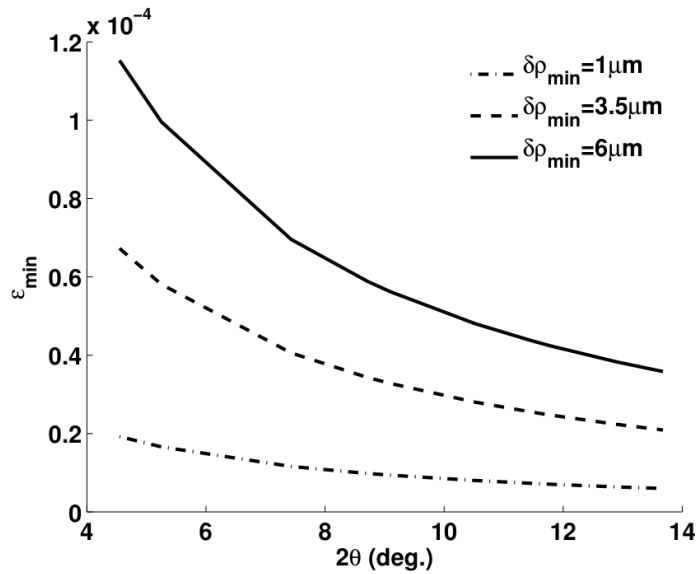
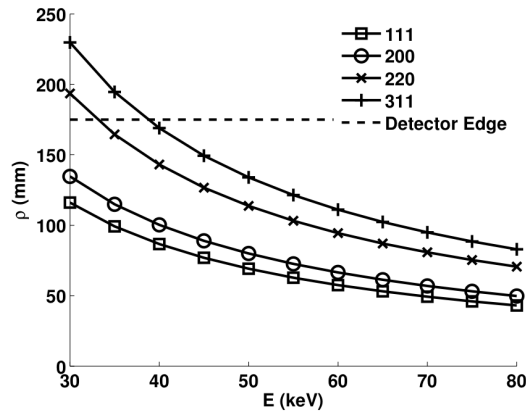


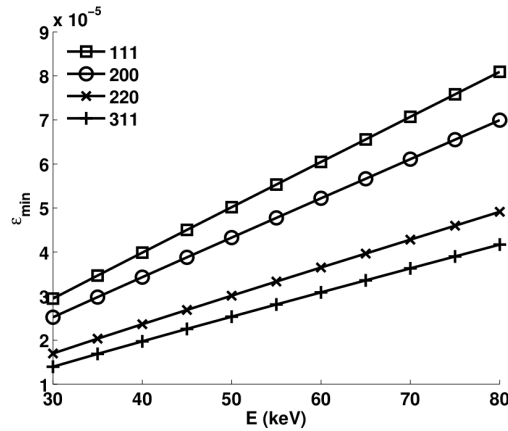
Figure 2.10: The minimum resolvable lattice strain for three $\delta\rho_{min}$ values show a characteristic decline in the minimum lattice strain value with increasing 2θ values.

To investigate the influence of the x-ray energy and the sample to detector distance on the uncertainty we set $\delta\rho_{min} = 3.5\mu m$. For discussion purposes let us consider the $\{111\}$, $\{200\}$, $\{220\}$, and $\{311\}$ diffracted peaks for pure aluminum

(FCC) with a lattice constant of 4.054\AA . From Equation 2.1 and the plane spacings for each $\{hkl\}$ we determine the Bragg angle as a function of the x-ray energy. For a fixed D of 650 mm, we find that the radial position of each peak decreases with increasing x-ray energy as shown in Figure 2.11(a). The corresponding minimum resolvable lattice strains for $\delta\rho_{min} = 3.5\mu\text{m}$ are shown in Figure 2.11(b).



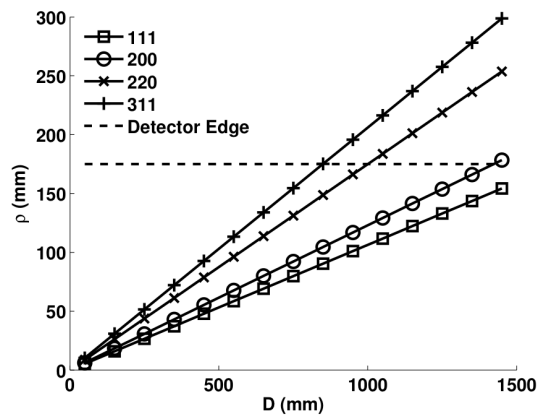
(a)



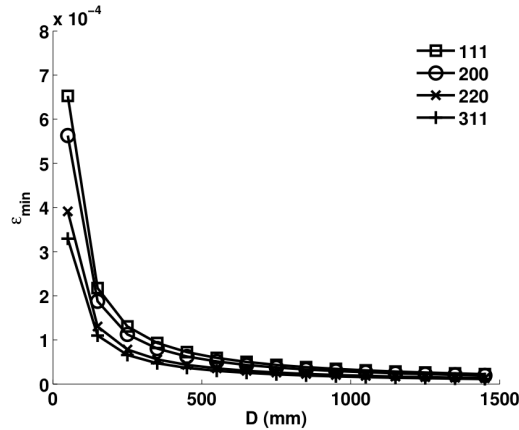
(b)

Figure 2.11: (a) The radial peak position of four aluminum $\{hkl\}$ s are shown for varying x-ray energies at a fixed sample to detector distance of 650 mm. (b) The minimum lattice strain for $\delta\rho_{min} = 3.5\mu\text{m}$ is shown to increase with increasing x-ray energy for the radial positions in (a).

Conversely, for a fixed x-ray energy of 50 keV the radial positions on the detector increase linearly with D . The results for the same four $\{hkl\}$ s are shown in Figure 2.12(a). Using Equation 2.18 and $\delta\rho_{min} = 3.5\mu m$, values for ϵ_{min} are found to decrease with increasing D and are shown in Figure 2.12(b). The pronounced reduction of the minimum lattice strains with increasing D shows that, for a fixed x-ray energy, the SPF experiment should be conducted at as large a sample to detector distance as possible.



(a)



(b)

Figure 2.12: (a) For a fixed x-ray energy the radial positional of the diffracted peaks increases linearly with the sample to detector distance. (b) The minimum resolvable lattice strains are shown for a peak shift of $\delta\rho_{min} = 3.5\mu m$.

As shown in Figure 2.11 and Figure 2.12, the x-ray energy and the sample to detector distance scale the lattice strain uncertainty by governing the radial position of each diffracted peak on the detector. These parameters should be selected such that the outer most $\{hkl\}$ of interest is measured near the edge of the detector to minimize ϵ_{min} . In addition, the selection of these parameters is further constrained by the absorption of the sample, the characteristics of the synchrotron, and the physical constraints of the experimental station. The optimal set of parameters varies for each experiment, but consideration of ϵ_{min} should guide the decision process.

To a lesser degree, the x-ray energy bandwidth and the cross section of the incoming beam play a role in the instrument portion of the lattice strain uncertainty. Both parameters contribute to the breadth of the diffracted peaks, and are typically constrained to less than 50 eV and $500\mu m \times 500\mu m$, respectively. These parameters are selected to allow for the diffracted peaks to be ‘sharp’, in an effort to minimize data ambiguity due to the overlap of diffracted peaks. Moreover, the SPF technique assumes that the diffraction comes from a point in space. As the beam size increases, spatial features in the data begin to play a role and slight perturbations in the uniformity of the flux of the direct beam are manifested as peak shifts between measurements. These shifts can be corrected using the calibrant material, and will be discussed in Sect. 2.5.

2.3.2 Model for U_{hkl}^i

If all of the sources of error are minimized, then U_{hkl}^i is expected to be a function of the resolution. The resolution for lattice strain measurements, as previ-

ously described, is governed by the smallest resolvable peak shift on the detector, $\delta\rho_{min}$, and the intensity required to identify the position of diffracted peaks. We define the model for the instrument uncertainty, $U_{c|s}^{i*}$, to be the superposition of separate terms for each aspect of the resolution,

$$U_{c|s}^{i*} = f(\delta\rho_{min}) + f(S). \quad (2.19)$$

Recall that S is the scaling factor for the intensity in Equation 2.7. To investigate the proposed functional form we assume $U_{c|s}^{i*}$ is equivalent to U_{hkl}^{i*} for the lattice strains measured for the calibrant material. In Figure 2.13, the measured uncertainty for the calibrant lattice strains are presented again with the addition of the average intensity for each $\{hkl\}$, S_{hkl} . The general downward trend of U_{hkl}^i with increasing 2θ values correlates well with the observed trends of ϵ_{min} shown in Figure 2.10. From the strength of this comparison we define $f(\delta\rho_{min})$ to be Equation 2.18.

We have consistently observed that the difficulty in determining peak positions increases as the peak intensity approaches the level of the diffraction pattern background. Therefore, we have chosen to represent $f(S)$ as inversely proportional to the intensity, i.e.

$$f(S) = S_{\alpha} \left(\frac{S_{lim}}{S} \right) \quad (2.20)$$

Here S_{lim} is the maximum possible pixel value (a property of the detector) and S_{α} scales the intensity contribution to the uncertainty. To investigate $f(S)$ we compare the variation in U_{hkl}^i with the magnitude of the measured intensities between the different $\{hkl\}$ s. It is important to note that the sharp intensity changes between the $\{hkl\}$ s are due to the characteristics of the material, in particular the crystal structure, and only the magnitude of the intensity for each

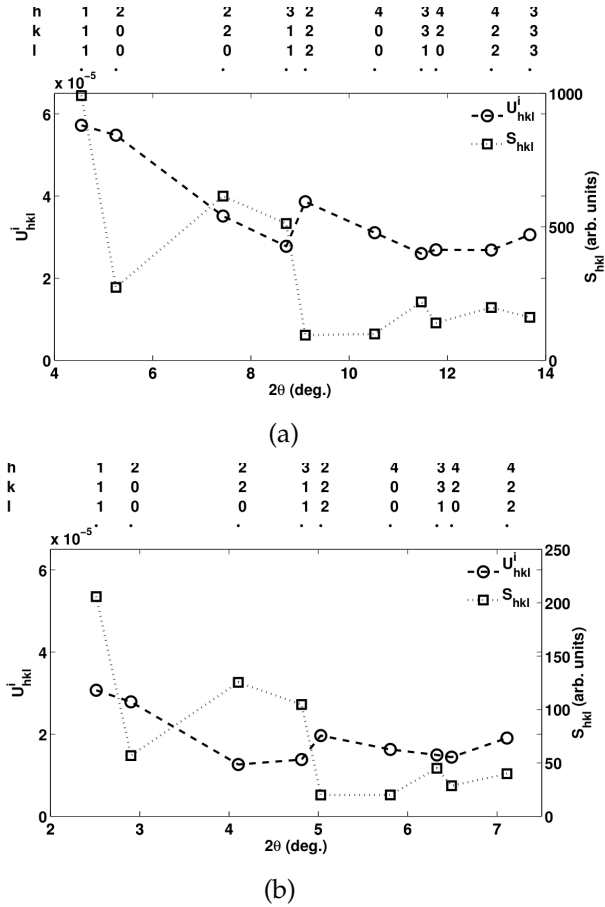


Figure 2.13: The measured uncertainty and the average intensity scaling factor for each CeO_2 $\{hkl\}$ is show for both the (a) CHES and the (b) APS experiment. The difference in the magnitude of the measured intensities between the detectors is due to the difference in maximum allowable intensity values.

$\{hkl\}$ is expected to contribute to $f(S)$. The most significant discontinuity of the measured U_{hkl}^i values occurs between the $\{311\}$ and the $\{222\}$ peaks. This deviation corresponds to a significant reduction of S_{hkl} for the $\{200\}$. Further investigation shows a similar reduction in S_{hkl} between the $\{111\}$ and the $\{200\}$ peaks, without a sharp change in the U_{hkl}^i values. A comparison between the two results shows that the average intensity for the $\{200\}$ peaks remains much greater than that of the $\{222\}$. It is probable that the reduction in the confidence

Table 2.4: The resulting parameters for Equation 3.7 are presented for both experiments.

Experiment	$\delta\rho_{min}$	S_α	S_{lim}
CHESS	$2.9\mu m$	1.6×10^{-8}	2^{16}
APS	$1.8\mu m$	7.6×10^{-9}	2^{14}

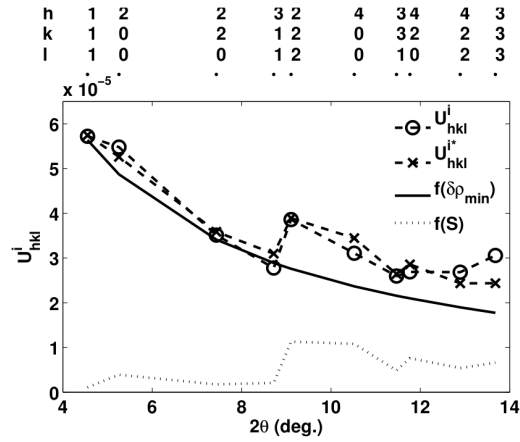
that the $\{222\}$ lattice strain distribution in Figure 2.7 is normal, is due to the difficulty in determining the peak positions for such low average intensity.

The uncertainty parameters $\delta\rho_{min}$ and S_α are determined from fitting U_{hkl}^{i*} to the measured uncertainty for the calibrant, U_{hkl}^i . Once these parameters are known, the instrument portion of the uncertainty can be calculated for each measurement using Equation 2.19 for the exact position on the detector and the measured intensity of the diffracted peaks.

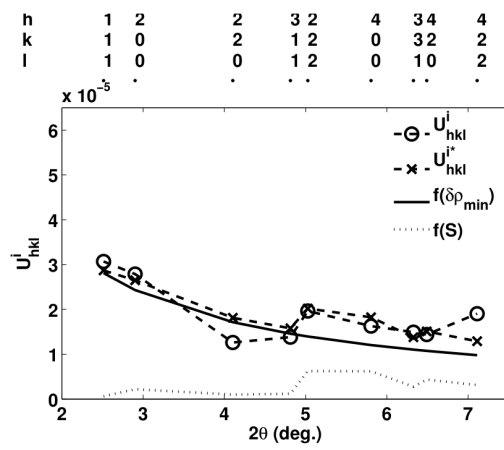
2.4 Results

The uncertainty parameters in Equation 2.19 are optimized using least squares such that U_{hkl}^{i*} matches U_{hkl}^i and the results are presented in Table 2.4 for both experiments. The function evaluated for each calibrant $\{hkl\}$ is shown in Figure 2.14, with the exact contribution from $f(\delta\rho_{min})$ and $f(S)$ shown explicitly. The results show close agreement between the measured and calculated uncertainties except for the last $\{hkl\}$ considered for both experiments.

To investigate $f(S)$ directly we made two diffraction measurements in succession where the only difference was the length of time for each exposure. For



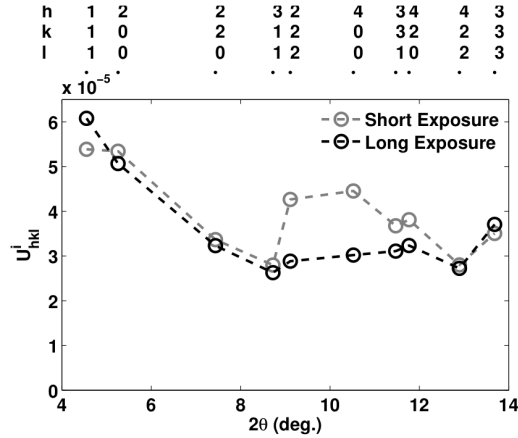
(a)



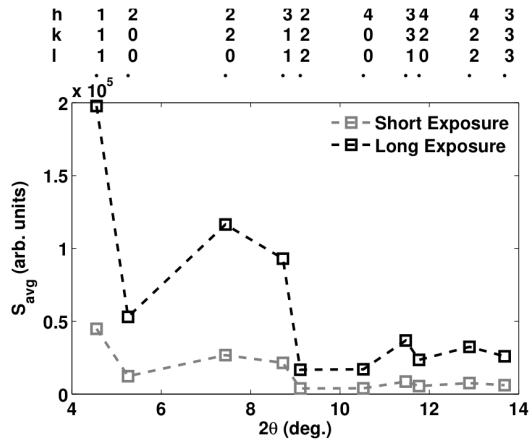
(b)

Figure 2.14: The calculated lattice strain uncertainties are shown overlaid on the measured values for both the (a) CHES and the (b) APS experiments. Each component of the uncertainty from Equation 2.19 is also shown independently.

a constant x-ray flux, the measured intensity values scale with the exposure time for each measurement. From these two diffraction patterns we can investigate the variation in U_{hkl}^i values due to a change in the measured intensity for the entire diffraction pattern. The results are shown in Figure 2.15. As expected, the uncertainty is greater for the measurements with low intensity (short exposure) as compared with the measurement made with a longer exposure time.



(a)



(b)

Figure 2.15: (a) The (a) U^i_{hkl} and (b) intensity values are shown for two measurements made in succession with different exposure times using the CHES experimental configuration. As expected, the uncertainty increases as the intensity decreases.

Each diffraction pattern was measured in succession and the time between images is set by the x-ray flux and the detector readout time. For the CHES and the APS experiments, the time between measurements was approximately 3.5 minutes and 2 seconds, respectively. We can investigate the influence of time on the lattice strain results by monitoring the geometric model parameters for each image. The parameters which vary significantly between measurements

are the pattern centers and are shown in Figure 2.16. The progression between measurements is indicated by the shading of the data points from black (first) to gray (last). The observed movement is systematic in nature and the magnitude is greater than the $\delta\rho_{min}$ values shown in Table 2.4. If this movement was left unaccounted for it would introduce a systematic bias to the results.

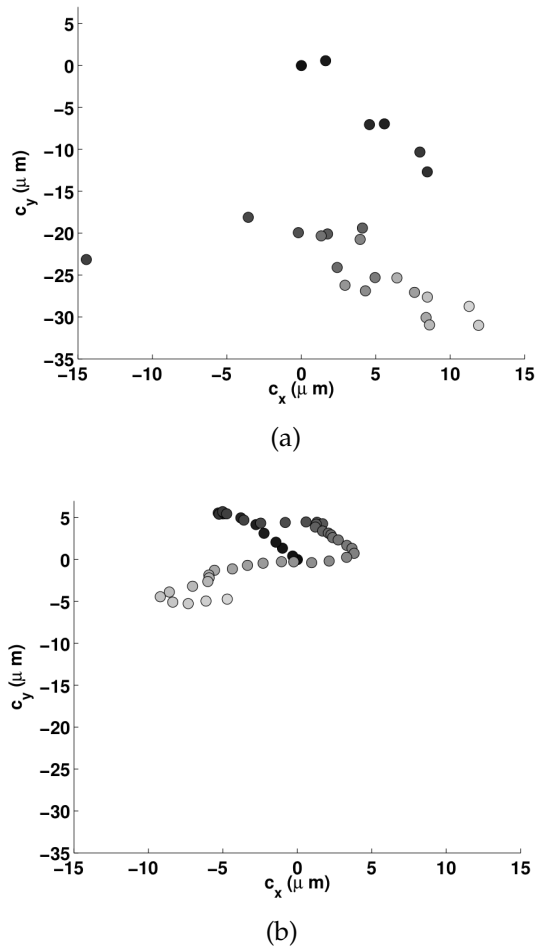


Figure 2.16: The change in the pattern center position is shown with increasing time by the data points ranging from black (first image) to gray for both the (a) CHESSE and the (b) APS experiments.

2.5 Discussion

The development of a new experiment typically involves an approximation of sensitivity. Does the change in the measured experimental variable represent an acceptable change in the quantity of interest? For mechanical testing these are often questions like what range of load or strain corresponds to a full scale output of ± 10 volts? The next step with such a system is often quantifying resolution - the smallest voltage change that might be detected by one's multimeter. The excitement of early results that display trends that might match our intuition - the load signal gets larger as weights are added to the system - is quickly replaced with the stark realization that we do not really know how "good" the measurements are. A robust estimation of the signal to noise ratio may be the most important step in the development of a mechanical testing capability. From a formal statistical perspective, this step is the quantification of experimental uncertainty associated with a particular confidence interval. With an accurate approximation of experimental uncertainty, lattice Strain Pole Figure data evolve from experimental curiosities that mainly define micromechanical trends for the orientations within the polycrystalline aggregate to high fidelity results that can be compared on equal footing with results from large scale polycrystal simulations. More importantly, by creating an analytical expression for uncertainty in terms of the experimental variables, experimental design can be improved to obtain a particular uncertainty value. This is especially important considering the enormous cost associated with synchrotron beam time.

Measurement of lattice strain requires the ability to identify subtle peak shifts on the area detector. Prior to identifying a peak shift the diffraction data are converted from a grid of pixel intensity data, to polar coordinates where

the pixel data are parsed into different azimuthal bins and integrated to produce arrays of radial positions versus intensities. Due to the discrete nature of the intensity data, this procedure can be simplified through the use of a simple finite element representation. The finite element method is a robust tool that is commonly used for representing seemingly continuous fields by discretizing the subject domains. Often complex differential equations are solved using finite elements. The application of the finite element method to diffraction data is straight forward and minimizes the uncertainty introduced during the integration procedure. This is advantageous for studies interested in quantifying ever smaller perturbations of diffracted peaks.

The combination of the high speed area detectors, the immense brilliance of typical synchrotron x-rays, and the number of unique measurement directions interrogated during an SPF experiment result in potentially massive lattice strain data sets. These data sets provide the foundation for the application of a statistics-based approach for quantifying the uncertainty. This uncertainty is a precision interval, for a specific confidence level, in which the probable value is expected to occur. Better understanding of the uncertainty for each measurement bolsters the application of SPF experiment to study the subtle evolution of lattice strain distributions during processes like cyclic mechanical loading.

Development of a functional representation for U_{ells}^i enables the instrument portion of the uncertainty to be determined for materials other than a calibrant. The quality of the comparison between the U_{hkl}^{i*} and the U_{hkl}^i values for both experiments, shown in Figure 2.14, indicates that the uncertainty can be approximated using simple functions of the lattice strain resolution. In essence, using Equation 2.19 and the parameters in Table 2.4 we can calculate the in-

strument portion of the uncertainty for the exact position and the intensity of each diffracted peak without a significant modification of the SPF experimental procedure. The uncertainty parameters in Table 2.4 illustrate possible values, but are not fundamental quantities for the synchrotron facilities. Due to the convolution of many sources of error and the robustness of the data reduction procedure employed, these values must be calculated for each experiment. The difference between the levels of uncertainty for the two experiments cannot be contributed directly to the x-ray source. It is probable that the differences in the detector readout mechanisms and the complexity of the distortion corrections are more likely sources. It is not possible to identify the source of this offset definitively from these results. The values presented here should be used as a benchmark for experiment planning and as a metric for comparing data reduction techniques.

The model developed for the instrument portion of the lattice strain uncertainty is based on all of the sources of error being minimized such that the resolution governs the results. The presence of systematic features in the background of the diffraction data, any incompleteness of the detector distortion correction, and the variation of the experimental configuration between measurements are the most significant sources of systematic error that must be considered. Due to the discrete nature of the calibrant results on the area detector, it is not possible to fully characterize and address the influence of systematic patterns present in the background for all possible situations. Often great lengths are taken to ensure that systematic features are minimized prior to conducting the experiment. Similarly, it is not possible to use the calibrant peak positions to develop a complete mapping for each pixel from a distorted to an undistorted configuration. The distortion corrections currently employed are continuous

functions that are the best fit for calibrant data, but are insensitive to local fluctuations. In both experiments the distortion corrections were found to account for most of the systematic offset. Any remaining distortions in the data biases the results and are not explicitly accounted for using the proposed model for the instrument portion of the lattice strain uncertainty.

In addition to conducting a full set of measurement using only a calibrant sample, employing a calibrant insert on the deforming sample allows for both the instrument uncertainty and the geometric model parameters to be quantified and monitored throughout the experiment to ensure the data reduction produces consistent results. To accurately remap the raw data to polar coordinates the diffraction pattern center must be identified. The pattern center is found from the calibrant, and corresponds to the centroid of the flux of the direct x-ray beam. Variation in the pattern centers between measurements is due to the relative movement of the slits, the detector, and the x-ray beams. Of these possible sources, the slight changes in the uniformity of the flux between measurements is the most substantial and must be accounted for. The approximate $30\mu\text{m}$ and $15\mu\text{m}$ variation in pattern centers found for the CHESS and APS experiments and shown in Figure 2.16 would, if unaccounted for, result in the lattice strains for the $\{111\}$ peak to be offset by as much as 5.8×10^{-4} and 2.4×10^{-4} , respectively. These errors act to bias the data and limit the applicability of estimating the lattice strain uncertainty using Equation 2.14.

2.6 Summary/Conclusions

Creating an approximation of the experimental uncertainty associated with the lattice Strain Pole Figure (SPF) experiment has the potential to transform this new method from a one-off “heroic effort” into a true measurement *capability* – one that can be employed hand-in-hand with detailed polycrystal simulations to create new understanding of micromechanical deformation processes like microcrack initiation. Due to the significant cost associated with producing synchrotron x-rays, SPF data are perhaps some of the highest value mechanical testing results currently being produced. It is the role of the experimentalist to approximate possible sources of error within his/her experimental method, but with the large amount of lattice strain data produced during a typical SPF experiment, conventional statistical analysis-based uncertainty determination can be applied. We proposed an expression for uncertainty that consists of “vector” components linked to the instrument and the material. This format does not preclude the addition of new uncertainty components as the experimental technique evolves. The focus of the paper is on the instrument portion of the uncertainty and was investigated with lattice strains measured at two synchrotron facilities using different experimental conditions – including two different x-ray detectors – at CHESS and the APS. The material portion of the uncertainty is most tightly coupled to the number of diffracting crystals, and the variation of the lattice strains between these crystals.

To investigate the instrument portion of the lattice strain uncertainty we applied the SPF experiment technique to an unstrained cerium dioxide powder. By calculating lattice strains for this unstrained powder we investigated the uncertainty for the exact experimental conditions employed. The results show uncer-

tainties well below previously quoted values, but more importantly, the results vary due to the position on the detector and the intensity of the diffracted peaks. Using these two parameters we developed a new model capable of recreating the uncertainties measured for the unstrained powder. This model for the instrument portion of the uncertainty can now be applied to diffraction results from materials other than an unstrained powder. By accurately quantifying the uncertainty we can confidently apply this experimental technique to more complex problems where the “signal-to-noise” ratio is expectedly small. Key findings from this paper include:

- A finite element discretization of the x-ray detector surface greatly simplified the integration process employed during the processing of diffraction data.
- The lattice strain uncertainty can be separated into independent sources coupled to the experimental configuration (instrument) and the material under investigation.
- The instrument portion of the uncertainty varies with the selection of the x-ray energy, sample to detector distance, and the characteristics of the area detector employed.
- A new model for the instrument portion of the uncertainty based on the lattice strain resolution was developed. The model parameters are determined from fitting results from an unstrained powder. Using this model the instrument portion of the uncertainty can be determined for materials other than the calibrant from the exact position and intensity values measured with the detector.
- The addition of an unstrained powder in an x-ray transparent container

to the back of the deforming sample allows for both the instrument portion of the lattice strain uncertainty and the experimental conditions to be monitored throughout the experiment to ensure the quality of the data is consistent between measurements.

2.7 Acknowledgments

The experiments at the Advanced Photon Source (APS) were conducted by Kevin McNelis. The work on was supported financially by the Air Force Office of Scientific Research under grant/contract number FA9550-06-1-0168 (Dr. Jaimie Tiley, program manager) and the Air Force Research Laboratory, Materials Directorate (Dr. T.J. Turner, program manager). The work is based upon research conducted at the Cornell High Energy Synchrotron Source (CHESS) which is supported by the National Science Foundation under award DMR-0225180. Dr. Alexander Kazimirov of CHESS is explicitly acknowledged for his ongoing support of our experimental effort at the A2 station. Use of the Advanced Photon Source (APS) was supported by the U.S. Department of Energy, Office of Science, Office of Basic Energy Sciences, under Contract No. DE-AC02-06CH11357. Dr. Ulrich Lienert, beamline scientist at APS 1-ID-C is acknowledged for his ongoing support of our experimental effort at APS.

CHAPTER 3
QUANTIFYING THE EVOLUTION OF CRYSTAL LEVEL STRESSES DUE
TO CYCLIC LOADING IN AA7075-T6

3.1 Introduction

The complex boundary conditions within a deforming polycrystal establish the crystal level stresses that drive processes like the initiation of fatigue life limiting defects. Over the past 10-15 years diffraction-based experiments and crystal-based simulations have shown the investigation of lattice strains to be a viable method for probing the crystal level stress state in deforming polycrystalline samples [9, 12, 16, 18, 22, 38, 48, 64]. These investigations have enabled new understanding and the development of models for capturing the mechanical response below the macroscopic length scale. Most of these efforts have consisted of comparing lattice strains, measured and simulated in relatively few directions. This limited set of measurements has not warranted a truly integrated approach of experiments and simulations to study the material behavior.

The recent availability of high rate x-ray area detectors has enabled the generation of massive numbers of lattice strain measurements. During a typical neutron diffraction experiment, lattice strains are measured in the sample loading and transverse directions. The prodigious data sets that can be generated using high rate x-ray area detectors represent an opportunity to reassess how investigations are conducted, which assumptions and models are applied, and ultimately how lattice strains are interpreted. At the core of this effort is the development of a new methodology for studying the grain scale response of a deforming polycrystal founded on the union of high energy diffraction mea-

measurements with *in situ* mechanical loading and crystal-based finite element simulations. This integrated approach provides a more complete picture of the micromechanical response of engineering materials than is possible with investigations based on comparing individual experiments and simulations.

This new methodology of integrated experiments and simulations is applied to study fatigue - in particular, the zero-tension fixed stress amplitude cyclic loading of an aluminum alloy 7075-T6 (AA7075-T6) sample. The fatigue life of a test specimen undergoing cyclic loading can be divided into two parts: the time required to initiate a fatigue life limiting defect and the time to propagate the defect to failure. There has been significant emphasis on the latter portion with the development of fracture mechanics, while the earliest stages of fatigue damage are not well understood. Quantifying the evolution of the stress state at the crystal scale prior to the nucleation of a fatigue life limiting defect has remained an elusive goal within the field of mechanics of materials. Understanding the crystal level stresses that drive the initiation of fatigue life limiting defects is an important step for the development of new models capable of predicting fatigue failures. The goal of this effort is to quantify the cycle-by-cycle changes in the elastic lattice strains, which are related to the stress state at the grain scale, during fixed stress amplitude cyclic loading. The lattice strain evolution is expected to be small, and the interpretation of the results as 'signal' or 'noise' is at the forefront of this effort.

The structure of this paper is as follows: an overview of how polycrystals deform, descriptions of x-ray diffraction techniques, lattice strain measurements, and crystal-based finite element simulations are presented first. Next, the procedure for quantifying measured and simulated lattice strains is demonstrated

for the AA7075-T6 sample and results are shown at several load steps during monotonic response (cycle zero). Using the monotonic results, we outline a precise estimate of the uncertainty for each measurement that is built on combining results from the experiment and simulation. We then investigate the evolution of the lattice strains measurements with increasing cyclic deformation using the uncertainty estimate to interpret the results. A key finding of this paper is that the stress state at the crystal scale evolves rapidly during the early portion of the fatigue life and slows as the sample approaches failure.

3.2 Background

Investigating elastoplastic deformation in polycrystalline alloys requires an array of characterization probes and sophisticated models. Before exploring the means by which these polycrystals deform and are investigated, it is worthwhile to outline the relevant length scales. From a continuum mechanics perspective we define the grain, the aggregate or polycrystal, the specimen, and the component. Each grain (synonymous with crystal) is a collection of unit cells formed by atoms that are fixed at specific periodic intervals. The aggregate is commonly referred to as a continuum point and is defined to be a collection of grains. Each aggregate has a statistical aspect to it in terms of the number, size, and orientation distributions of the set of crystals. The specimen is comprised of many aggregates. The component constitutes all possible specimens; specimens are designed such that the distinction between the specimen and the component is minimal. A schematic of the relationship between the relevant length scales is shown in Figure 3.1.

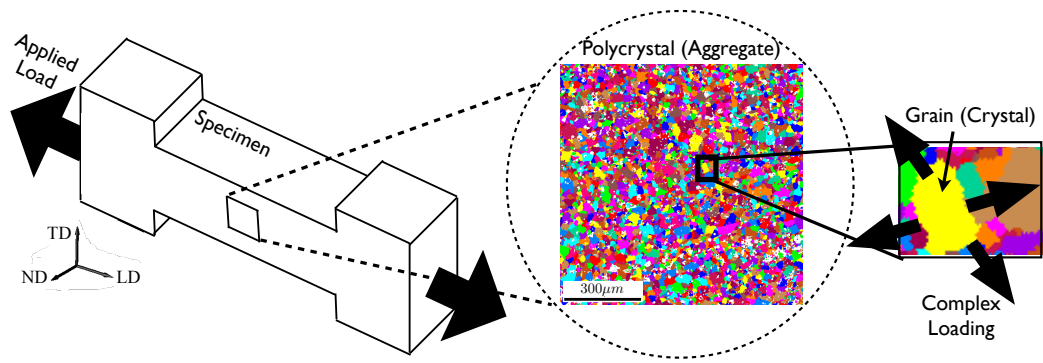


Figure 3.1: Schematic of the relevant length scales for studying elastoplastic deformation in polycrystalline alloys.

Conventional mechanical testing consists of measuring the response of a sample to external loads. Investigations of the macroscopic response alone are inadequate to study the micromechanical conditions that lead to the formation of a fatigue life limiting defect. Even during simple uniaxial tension, within the deforming polycrystal there is variation in the stress state both within and between the grains due to anisotropic single crystal properties and the complex arrangements of grains. To accommodate mechanical equilibrium at the grain scale, each grain responds to the boundary conditions prescribed by the neighboring grains. Developing new techniques that probe this length scale, during macroscopic loading, are paramount for investigating the evolution of the crystal level stresses due to cyclic loading.

3.2.1 Crystal Orientations and Diffraction Measurements

There are many ways to represent the orientation of a single crystal relative to the sample coordinate system. One method is to represent each orientation by the rotation matrix, \mathbf{R} , which maps a vector from the crystal coordinate system

to the sample coordinate system, $\mathbf{v}_{sam} = \mathbf{R}\mathbf{v}_{crys}$. Here both \mathbf{v}_{sam} and \mathbf{v}_{crys} are defined in Cartesian coordinate systems. For a cubic crystal the basis vectors for a vector in the crystal coordinate system, \mathbf{v}_{crys} , are aligned with the $\{100\}$ cube plane normals. The basis vectors for a vector in the sample coordinate system, \mathbf{v}_{sam} , are defined relative to the sample Loading Direction (LD), Transverse Direction (TD), and Normal Direction (ND).

The relevant direction for diffraction measurements is the bisector of the incoming and diffracted x-ray beams shown in Figure 3.2, and defined the scattering vector, \mathbf{s} . Diffraction occurs for the subset of crystals with plane normals, $\{hkl\}_s$, aligned with \mathbf{s} . The diffraction of monochromatic x-rays (fixed wavelength, λ) is represented by Bragg's law [17],

$$n\lambda = 2d_{\mathbf{c}||\mathbf{s}} \sin \theta_{\mathbf{c}||\mathbf{s}} \quad (3.1)$$

Here n is an integer, $d_{\mathbf{c}||\mathbf{s}}$ is the crystallographic plane spacing, and $\theta_{\mathbf{c}||\mathbf{s}}$ is half the angle between the transmitted and diffracted x-ray beams shown in Figure 3.2 and is referred to as the Bragg angle. The subscript $\mathbf{c}||\mathbf{s}$ indicates the specific measurement where for cubic materials \mathbf{c} is defined $\mathbf{c} = \frac{1}{\sqrt{h^2+k^2+l^2}}[h \ k \ l]$ and \mathbf{s} the scattering vector. The orientations that satisfy Equation 3.1 share a crystallographic plane normal which is parallel with the scattering vector and are explicitly defined as a crystallographic fiber. The orientations that comprise the fiber satisfy,

$$\mathbf{R}\mathbf{c} = \pm\mathbf{s} \forall \mathbf{R} \quad (3.2)$$

The $\pm\mathbf{s}$ is due to the subset of orientations interrogated being unchanged by the sign of the measurement direction.

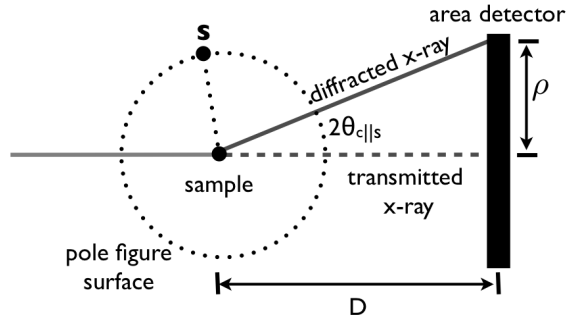


Figure 3.2: The transmission diffraction geometry is shown. Here D is the distance between sample and the area detector and ρ is the radial position of the diffracted x-ray on the detector.

3.2.2 Rodrigues Parameterization and the Orientation Distribution Function

The rotation matrix, \mathbf{R} , can also be represented using the Rodrigues parameterization [27]. A Rodrigues orientation vector is an angle-axis representation where the direction of the vector from the origin of the space defines a rotation axis, and the magnitude is related to the rotation angle,

$$\mathbf{r} = \mathbf{n} \tan\left(\frac{\phi}{2}\right) \quad (3.3)$$

Here \mathbf{n} defines the axis of rotation and ϕ is the angle of rotation about the axis [27, 39, 50]. A strength of the Rodrigues parameterization is that the orientations that define a fiber (Equation 3.2) form a straight line in Rodrigues space. The application of crystal symmetries reduces the space comprised of all possible Rodrigues vectors to a bounded region for many crystal types. This reduced set of orientations is referred to as the fundamental zone [2, 27, 32, 39]. Any portion of a fiber that extends beyond the boundary of the fundamental zone can be remapped back to an equivalent orientation within the fundamental zone. The result is that a fiber shown in the fundamental zone appears as many segments

[56].

Calculations over the fundamental zone are performed using a finite elements representation where each node represents an orientation [39]. Representing the fundamental zone with finite elements allows for field quantities to be defined over orientation space and provides a robust framework for calculating fiber averaged quantities (i.e. orientation pole figures). A more complete description of the fundamental zone and the use of finite elements over orientation space can be found in [2, 27, 32, 39]. Use of the software package, OdfPf, greatly simplified the process of generating a finite element mesh for the fundamental zone and the calculation of fiber averaged quantities [8].

The Orientation Distribution Function (ODF), $f(\mathbf{r})$, represents the likelihood of a crystal having a particular orientation relative to the sample reference frame. This relationship is formally defined over the fundamental zone as,

$$\frac{dV_\beta}{V_\beta} \equiv \frac{1}{V_\Omega} f(\mathbf{r}) d\mathbf{r} \quad (3.4)$$

Here V_β is the volume of the material in physical space, V_Ω is the associated volume in orientation space. The integral of the ODF over the fundamental zone must equal one and $f(\mathbf{r}) \geq 0$.

3.2.3 Lattice Strain Measurements

There are few techniques available for probing the grain scale mechanical response of a deforming polycrystal. The most notable combine *in situ* mechanical loading and high energy diffraction to measure lattice strains at many points in the deformation history. Lattice strain experiments can be separated into two

categories based on whether the measurements probe the response of individual grains within the aggregate [1, 26, 41, 42, 45, 52], or an aggregate comprised of grains that satisfy the diffraction condition (so called powder experiment) [9, 12, 16, 18, 22, 38, 48, 64]. The diffraction data consist of isolated ‘spots’ for the single grain experiment and complete Debye rings for the aggregate experiment. For this effort we focus on the aggregate experiment.

Lattice strains are the average normal strain in the direction of the scattering vector for the subset of crystals that satisfy Bragg’s Law (Equation 3.1). Each lattice strain measurement is defined using the plane spacing as,

$$\epsilon_{c||s} = \frac{d_{c||s} - d_{c||s}^0}{d_{c||s}^0} \quad (3.5)$$

Here $d_{c||s}^0$ is the initial or unstrained plane spacing. For a cubic material only one lattice constant is needed to describe the crystal lattice.

The Lattice Strain Pole Figure (SPF) Technique

The lattice Strain Pole Figure (SPF) experiment, presented in [48], combines *in situ* loading with high energy x-ray diffraction to determine lattice strains in engineering materials. The diffraction experiment is conducted in transmission (Figure 3.2) and the sample is deformed using load control due to the strong dependence of lattice strain on the applied load. Each SPF consists of the lattice strain data measured in many directions for a particular $\{hkl\}$. To generate an SPF, the measured lattice strains are plotted at the intersection of the scattering vector, s , and a unit sphere as shown in Figure 3.2. A point on an SPF is defined relative to the sample coordinate system. Sample rotations increase the number of independent measurement directions - resulting in an increase in SPF coverage. An SPF experiment consists of a series of loading interruptions, or holds, in

the deformation during which a series of diffraction measurements (along with sample rotations) are conducted. During each of the holds, the load is reduced by 10% to minimize creep effects during the series of diffraction measurements [18].

Since lattice strains are elastic, the SPFs have also been used to determine the most likely lattice strain tensor, and ultimately the stress tensor, for each crystal orientation [4–6]. For more background on the SPF technique the authors recommend [5, 48, 56].

Diffraction Data

An example of a diffraction pattern for the AA7075-T6 sample is shown in Figure 3.3(a) with three aluminum Debye rings indicated. In addition to the aluminum, there are also Debye rings from an unstrained cerium dioxide (CeO_2) powder. The CeO_2 powder is held within an x-ray transparent container that is fixed to the sample and referred to as a calibrant insert. The calibrant insert is used to quantify both the experiment geometry and the lattice strain uncertainty associated with the instrument itself [5, 55].

The area detector is made up of a regular grid of rectangular pixels. Each pixel quantifies the x-ray intensity measured over its area. The raw data are therefore an array of position and intensity values. Typically, each diffraction pattern is mapped from the rectangular array defined by the pixels to polar coordinates and azimuthally parsed into radial/azimuthal subregions ($\Delta\rho, \Delta\eta$). The intensity within each subregion can be integrated to generate arrays of radial position versus intensity for each bin (η) [55]. Using the experiment geome-

try shown in Figure 3.2 these arrays are converted to 2θ versus intensity like the example shown in Figure 3.3(b).

The resulting arrays of 2θ values versus intensity for each η bin are then fit with an analytic profile function for each diffraction peak. For synchrotron data a pseudo-Voigt analytic peak profile function, which combines Gaussian and Lorentzian peak shapes [5, 55, 72], is often used. By minimizing the difference between the superposition of a smoothly varying background and the peak profile functions, the positions of each peak can be determined [5, 55]. With the peak positions ($2\theta_{\text{c||s}}$) quantified, lattice strain can be calculated using Equation 3.1 and Equation 3.5.

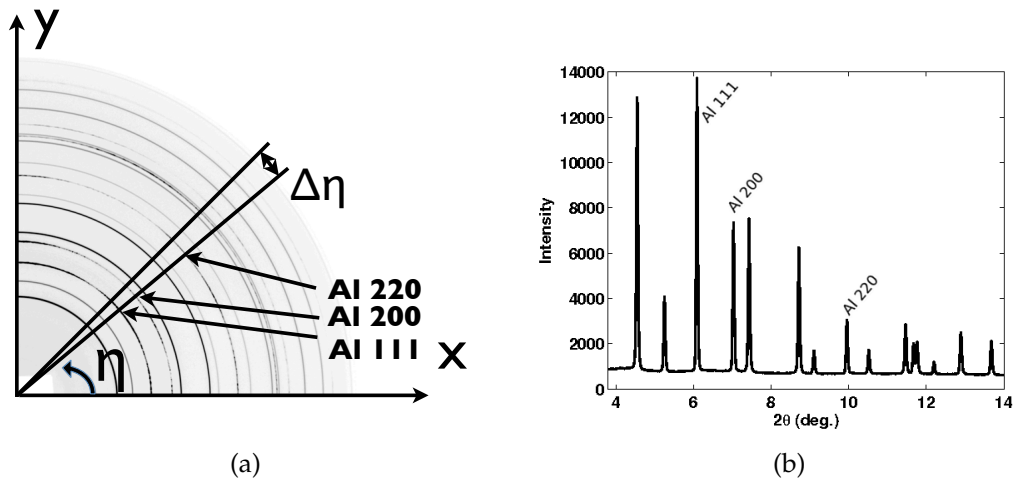


Figure 3.3: (a) One quarter of the surface of an area detector displaying a typical diffraction pattern for the AA7075-T6 sample with a 5° azimuthal bin ($\Delta\eta$) indicated. (b) Spectrum for the highlighted bin with the same aluminum peaks indicated.

The conversion of raw diffraction data to lattice strains relies heavily on models for the detector, the experiment configuration, and even the material under investigation. Ideally the detector would be positioned at a known distance from the sample, and the surface of the detector would be centered and

orthogonal to the incoming x-ray beams. To convert diffracted intensity to lattice strains necessitates an accurate model for the experiment geometry [5]. The model parameters consist of the coordinates of the pattern centers, two tilt angles, the sample to detector distance (D in Figure 3.2), and a distortion correction for the detector. The model parameters are determined using diffraction results for the calibrant material. Using the well known lattice parameters for the CeO_2 , the x-ray wavelength, and an initial guess for the model parameters a set of expected peak positions can be calculated for the calibrant. The model parameters are determined by minimizing the difference between the measured and expected calibrant peaks [5]. After the data are mapped to a 'corrected' configuration the lattice strains can be calculated. The initial guess for the model parameters is found using the data reduction software Fit2D [29].

Each diffracted peak used to calculate a lattice strain measurement represents a subset of crystals within the sample that satisfies the diffraction condition. In essence, each lattice strain measurement is a statistical sampling problem linked to the interpretation of $d_{c||s}$ as the average plane spacing for the subset of orientations that satisfy Equation 3.2. The goal of the SPF experiment is that each lattice strain measurement (analogous to a sample mean in statistics) provide insight into the true lattice strain value (population mean). Without an estimate of the difference between the true and measured lattice strain, it is difficult to interpret the lattice strain results.

The need for an estimate of the lattice strain uncertainty for each measurement can be explored with a simple example. Consider the iso-strain case for a polycrystal. A lattice strain measurement from a single grain would be sufficient to capture the true lattice strain value. Conversely, as the variation in the lattice

strains between the probed grains increases, the measured value is coupled to the both the number of grains interrogated and the magnitude of this variation. To approximate the variation in the lattice strains between the crystals that contribute to a single diffraction measurement we use a crystal-based elastoplastic finite element model to simulate the response of a virtual polycrystalline specimen under the same loading conditions as in the experiment. Estimating a precision interval, referred to as the uncertainty, about the measured value in which the true value is expected to occur is central to the interpretation of the results at this length scale.

3.2.4 Crystal-based Finite Element Simulation

An elastoplastic constitutive model, which approximates the behavior of a single crystal, is implemented within a finite element formulation to model the behavior of an aggregate of crystals. The finite element formulation is implemented on a distributed computing (parallel) architecture. An overview will be provide here, but a complete description of the finite element model and its implementation can be found in [21, 46, 47].

The elastoplastic constitutive model incorporates anisotropic elasticity, coupled with plastic deformation by crystallographic slip on a restricted number of slip systems. The inelastic shearing is rate-dependent and for FCC materials occurs on 12 $\{111\}\langle 110\rangle$ slip systems. By assuming crystallographic slip to be the dominant mode of inelastic deformation in a crystal, the crystal kinematics can be represented by a multiplicative decomposition of the deformation gradient into plastic, rotational, and elastic stretching portions. Accordingly, texture

evolution is represented through crystallographic lattice reorientation [46, 47].

The simulation models the response of a polycrystalline aggregate to the applied boundary condition using the weak form of the equations of equilibrium and implicit time-integration of the constitutive equations. A virtual specimen in the shape of a cube is instantiated with thousands of grains, each composed of multiple elements. All the finite elements associated with one grain are assigned the same initial lattice orientation, and the lattice orientations of the grains are assigned by random sampling of the ODF.

A major strength of these simulations is the explicit representation of the stress state for each element - providing information at the grain, and subgrain level. In essence, the simulation monitors the stress state of each crystal, and directly represents the processes by which the material deforms. Results from the crystal-based simulations can be sampled by isolating elements oriented to satisfy the diffraction condition. The strain tensor for each element can then be projected in the direction of the scattering vector to 'build' the lattice strain distribution grain-by-grain. Having access to the whole distribution, and not just the mean lattice strain value that is accessible experimentally, enables the variation in the lattice strains between the different diffracting grains to be calculated. Additionally, the combination of a crystal-based finite element simulation with experimental data at the grain scale allows for the pertinent model parameters that govern the lattice strain response to be determined.

Moreover, results from both the experiment and the simulation can also be used to determine the Lattice Strain Distribution Function (LSDF), which is the most likely strain tensor for each crystallographic orientation [3, 4, 56, 65, 66]. Using the LSDF, Hooke's law, and the single crystal elastic moduli the average

stress for each crystal orientation can be determined. Rigorous comparisons of the experimental and simulated results can be conducted using the coefficients of a spherical harmonic decomposition of the stress over orientation space [49].

3.3 Measuring/Simulating SPFs for AA7075-T6

To quantify and monitor lattice strain evolution during fixed stress amplitude cyclic loading requires a suite of characterization probes and precise models to interpret the results. To explore the techniques used to build the measured and simulated SPFs we will consider several load steps during the monotonic loading for cycle zero (the initial loading cycle). The first step in such an investigation is to characterize the state of the material, initialize the virtual sample, and simulate the macroscopic response. The investigation into the grain scale response requires information from both the simulation and experiment. As might be expected, the use of a precise set of material constants, including the single crystal elastic moduli and slip system strength is needed to simulate the material response [70]. The addition of alloying elements can perturb the single crystal properties of a pure material. Quantifying these properties for alloys like AA7075-T6 is necessary for the simulation to accurately represent the deforming polycrystal. Integration of the finite element simulation with the diffraction data allows for these properties to be perturbed until the simulated lattice strains match those measured experimentally.

3.3.1 Material Characterization

The AA7075-T6 is an aerospace alloy that is regularly used in the skin and fuselage of aircraft. The AA7075-T6 sample used was cut from a 1.63 mm thick rolled sheet acquired from Alcoa for its near equiaxed grains. The coordinate system for the sheet is defined by the sheet rolling direction (L), the long transverse direction (LT), and the short transverse direction (ST). Recall that the sample coordinate system was defined by the loading direction (LD), the transverse direction (TD), and the normal direction (ND). Using the symbol || to indicate parallel, the relationship between the sample and the sheet was LD||LT, TD||L, and ND||ST. The gage length of the specimen was 36.83 mm long with a $1 \times 1.2\text{mm}^2$ (ND×TD) cross-section (schematic shown in Figure 3.8). An Electron Back Scattered Diffraction (EBSD) scan for the sheet rolling plane is shown in Figure 3.4 with each grain overlaid with a random color. The average grain size was determined from EBSD and optical micrographs to be $\sim 19.5\mu\text{m}$. The ODF was found using a Rietveld analysis of the diffraction data and is shown in Multiples of a Uniform Distribution (MUD) in Figure 3.5 [7, 43, 44].

The macroscopic stress-strain response of the sample is measured during the deformation with a load cell and a strain gage fixed to the sample. The monotonic portion of the stress-strain response is shown in Figure 3.6. At many points in the deformation history the applied load is reduced to 90% of the previous value and the series of diffraction images necessary for an SPF are measured using different sample orientations.

The lattice parameter for the face centered cubic AA7075-T6 was determined from the diffraction data prior to loading. By varying the lattice parameter until the difference between the measured and expected plane spacings was mini-

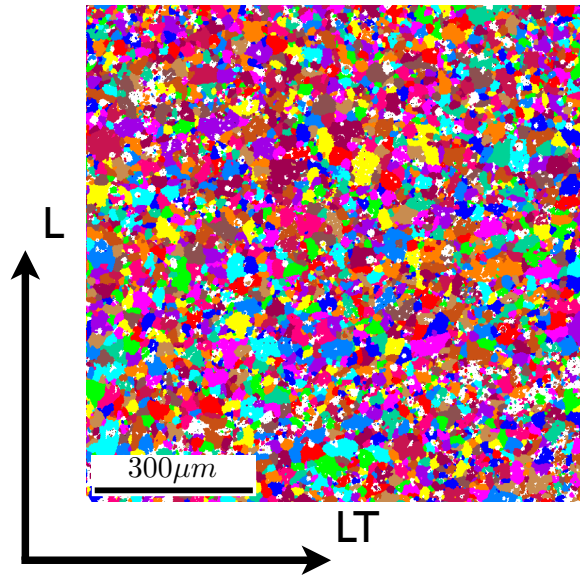


Figure 3.4: EBSD data for AA7075-T6 are shown for the plane defined by the sheet rolling direction (L) and the long transverse direction (LT). An arbitrary color is overlaid for each grain.

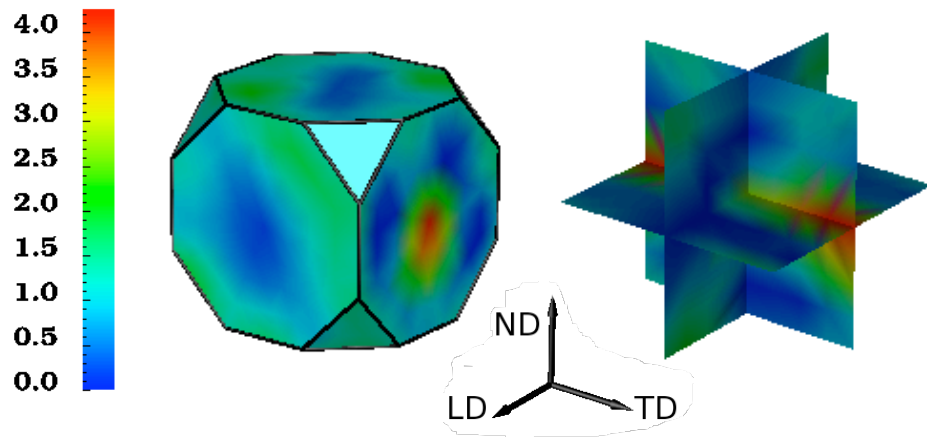


Figure 3.5: The ODF for the AA7075-T6 calculated from the diffraction data using MAUD [44]. The colorbar is in Multiples of a Uniform Distribution (MUD)

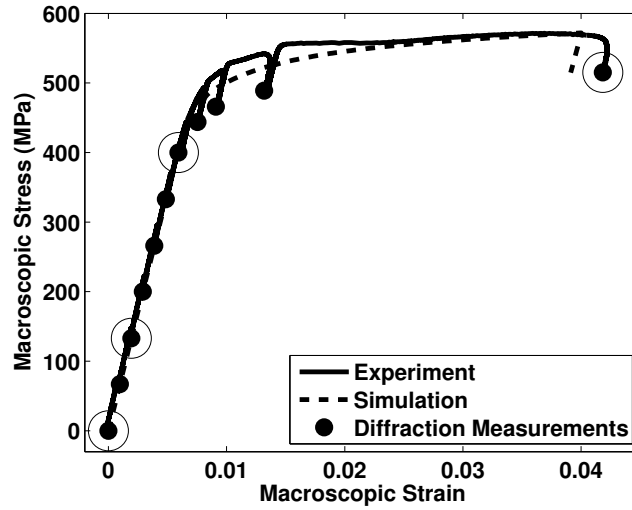


Figure 3.6: Experiment and simulation macroscopic stress-strain curves are shown for the monotonic portion of the deformation. The points indicate where the SPFs were measured. The circled points indicate the stress levels associated with the SPFs shown in Figure 3.9, Figure 3.10, Figure 3.11, and Figure 3.12.

mized, the lattice parameter that best fit the initial plane spacings was found to be 4.056 \AA . This value matches the lattice constant found in [73] for the same material with two different grain sizes to within $\pm 0.005 \text{ \AA}$.

3.3.2 Diffraction Experiment Details

The experiment was conducted in the A2 experimental station at the Cornell High Energy Synchrotron Source (CHESS). An x-ray energy of 49.989 KeV ($\lambda = 0.2480 \text{ \AA}$) with a bandwidth of 50 eV was selected using a silicon {111} double-crystal monochromator. The beam size of $0.5\text{mm} \times 0.5\text{mm}$ was defined by two sets of tungsten slits. The experiment was conducted in transmission with approximately 650 mm between the sample and the MAR345 area detector (D in Figure 3.2). The detector pixel size is $100\mu\text{m} \times 100\mu\text{m}$. A detailed schematic of

the components in the beam path and a description of the experimental method can be found in [56]. The diffractometer used for these experiment, shown in Figure 3.7, allows for the rotation of the specimen about a vertical axis orthogonal to the x-ray (ω) and the specimen LD (χ) [57]. The zero position ($\omega = \chi = 0^\circ$) is defined such that the sample normal is aligned with the incoming x-ray beam. Measurements were made for $\omega = -40^\circ$ to 35° in nine increments with $\chi = 0^\circ$ and $\chi = 12.5^\circ$, and $\omega = -25^\circ$ to 25° in six increments with $\chi = 25^\circ$. To increase the number of crystals that contribute to each measurement the sample was reoriented, or rocked about each (ω, χ) pair by $\pm 2.5^\circ$ in ω and χ . The benefits of sample rocking will be discussed in Sect. 3.4.2. These measurements were repeated at each point shown in Figure 3.6. The SPFs were also measured at 515MPa for cycle numbers 1, 5, 10, 20, 50, 100, 500, and 1000. The full stress-strain curve is shown in Figure 3.19.

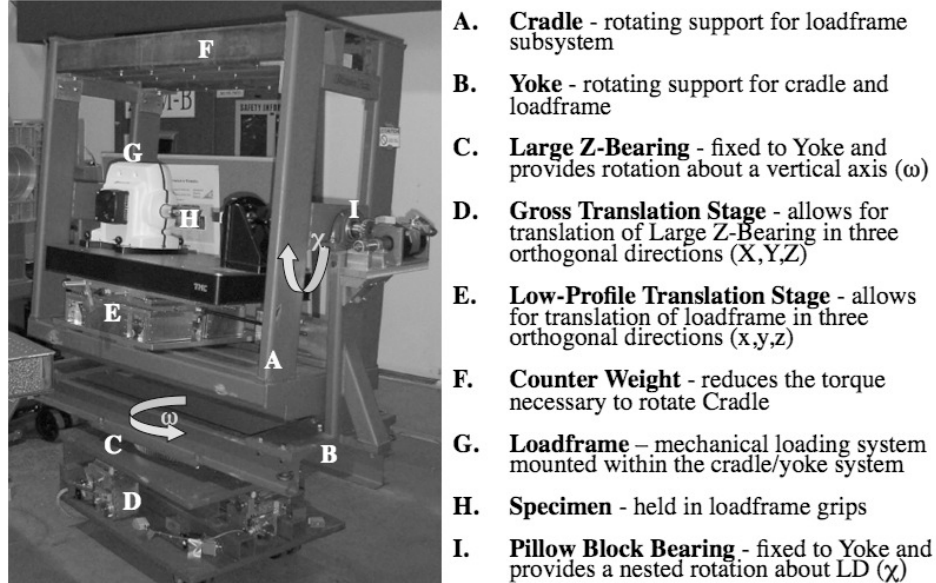


Figure 3.7: The loadframe/diffractometer is shown with key components labeled [57].

3.3.3 Simulation Details

A virtual specimen was instantiated with 2916 complete rhombic dodecahedra grains, where each complete grain was comprised of 48 10-node tetrahedra elements. There were also additional partial grains added to create the surfaces of the cube. The virtual specimen has a total of 192,000 finite elements contributing to the mesh. The virtual specimen underwent uniaxial tensile loading, with a deformation history analogous to the monotonic portion of that applied in the experiment. As shown in Figure 3.8, the sample LD, TD and ND directions correspond to the X, Y and Z directions of the finite element mesh, respectively. Both the experiments and simulations were conducted in load control. A constant velocity was applied on the positive X surface of the finite element mesh, while the $X = 0$ face of the mesh was constrained in the X-direction. The two positive Y and Z surfaces of the mesh were traction-free, while the $Y = 0$ and $Z = 0$ surfaces had symmetry boundary conditions imposed. The simulation was conducted by Su Leen Wong.

The influential parameters for the simulation are the strain hardening constants and the single crystal elastic moduli. An isotropic hardening law was used to evolve the slip system strengths. The required constants were determined by adjusting the values until the simulated and measured macroscopic stress-strain curve compared well. A more complete description of the model and the model constants can be found in [71].

The lattice strain response in the elastic-plastic transition regime is influenced by a combination of the elastic and plastic anisotropy [70]. Due to the addition of alloying elements, the single crystal elastic moduli for AA7075-T6 will not be identical to those for pure aluminum. In particular, the anisotropic ratio

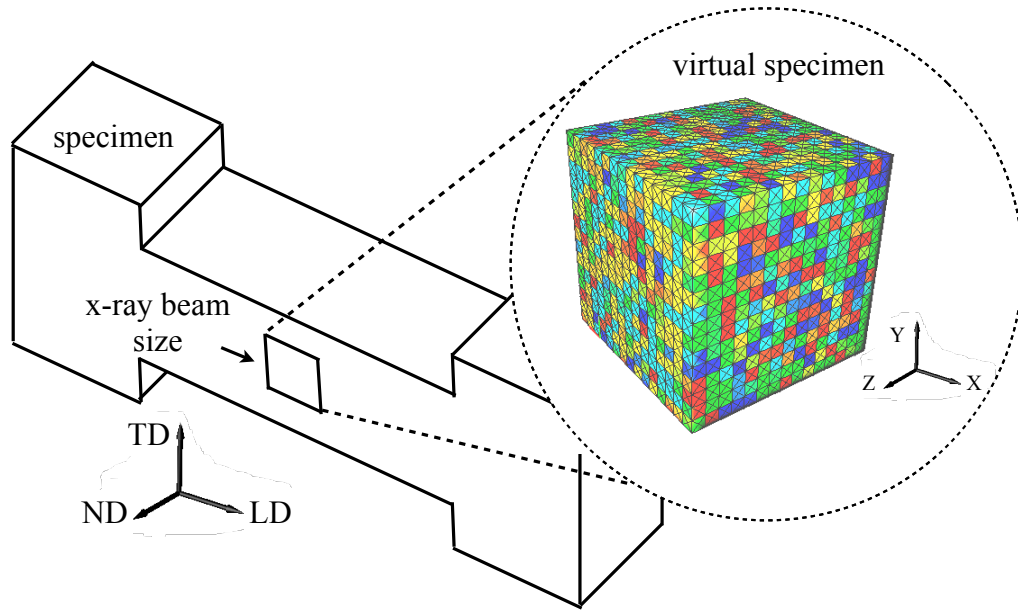


Figure 3.8: The relationship between the specimen and the virtual specimen is shown schematically. The color of the grains making up the virtual specimen corresponds to the orientation. The x-ray beam size of $0.5\text{mm} \times 0.5\text{mm}$ is also indicated.

can vary significantly [20]. To determine the elastic moduli we start with the single crystal elastic moduli of pure aluminum reported by Hosford [34]. The values for the single crystal elastic moduli most suited to AA7075-T6 were determined by comparing a suite of simulated lattice strains using different moduli to the measured lattice strains following the procedure outlined in [18, 70]. The lattice strains are compared for all the measurements made throughout the deformation history and the best fit corresponds to the lowest difference between the measured and simulated lattice strains. The elastic constants used were $C_{11}=101.5$ GPa, $C_{12}=60.0$ GPa, and $C_{44}=29.0$ GPa. The selection of the elastic constants is aided by a wide range of scattering vectors to avoid biasing the simulation toward a select few directions.

3.3.4 Measured and Simulated SPFs During the Monotonic Response

Both the measured and simulated SPFs for the monotonic loading at 0, 135, 400, and 515 MPa are shown in Figure 3.9, Figure 3.10, Figure 3.11, and Figure 3.12, respectively. The results are shown with a different color bar for each load step to allow for variation between the experiment and simulation to be visible. Each figure shows the SPFs for the experiment (exp.) and the simulation (sim.). The difference (dif.) between the two (exp.-sim.) are shown for all but the zero load SPFs (Figure 3.9). The simulated SPFs at 0 MPa shown in Figure 3.9 are zero by definition. The differences between the experiment and simulation in Figure 3.9 are due to the presence of a residual lattice strain distribution in the sample. The overall trends for the SPFs in Figure 3.10, Figure 3.11, and Figure 3.12 show the most tensile lattice strains near LD and the most compressive near TD. These trends are present in both the simulated and the experimental results. Each element in the simulations is initialized with a zero strain state. The influence of the residual is most visible for the $\{200\}$ SPFs throughout loading. Overall the experiment and simulation compare well with increasing deformation. To interpret changes in the lattice strains as a result of material evolution or experimental fluctuations we need to estimate the uncertainty in the lattice strain experimental data.

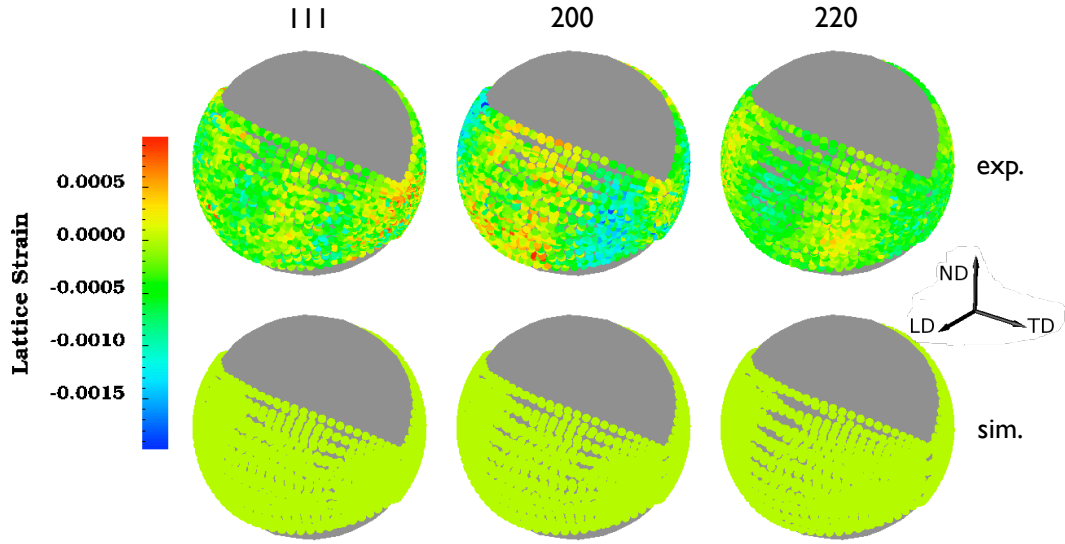


Figure 3.9: The measured (exp.) and the simulated (sim.) SPFs are shown at 0 MPa. The simulation assumes the initial lattice strains to be zero.

3.4 Lattice Strain Uncertainty

Recently we have proposed a new framework for the lattice strain uncertainty for each measurement was presented which separates the contributing sources of error into two categories that vary independently [55],

$$U_{\text{c|ls}} = \sqrt{U_{\text{c|ls}}^i{}^2 + U_{\text{c|ls}}^m{}^2 + \dots} \quad (3.6)$$

These sources represent the contribution to the uncertainty from the instrument used to make the measurements, $U_{\text{c|ls}}^i$, and the contribution to uncertainty from the material under investigation, $U_{\text{c|ls}}^m$. The instrument contribution to the uncertainty was shown in [55] to be related to the experiment geometry and the resolution of the position and intensity of diffracted peaks on the area detector. The material portion of the uncertainty is related to the number of diffracting crystals, and the variation in the lattice strain between these crystals. Previous investigations have implicitly relied on the assumption that enough crystals sat-

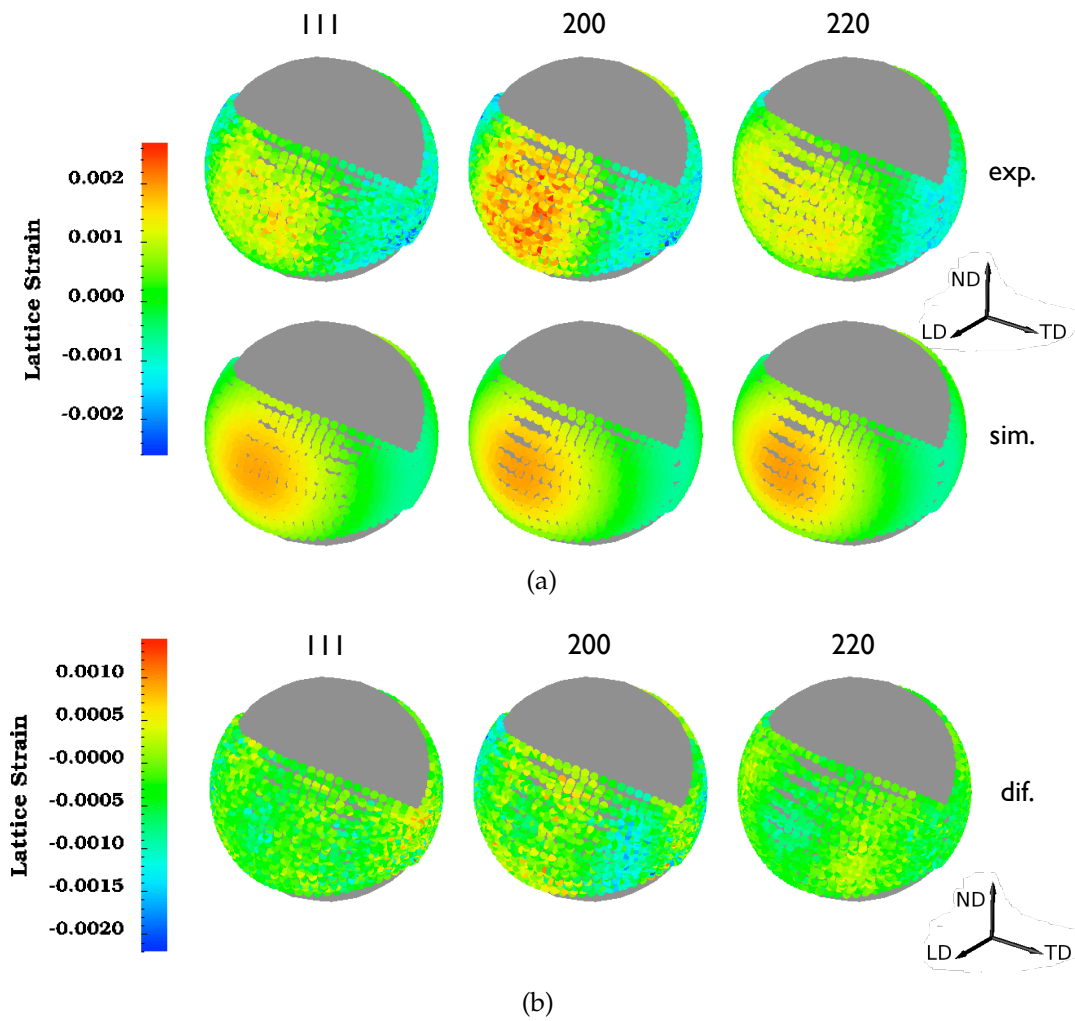


Figure 3.10: (a) The measured and the simulated SPFs at 135 MPa. The difference is shown in (b).

isfy the diffraction condition that the contribution to $U_{\text{c||s}}^m$ could be assumed to be zero. If $U_{\text{c||s}}^m$ is not zero, the results may be difficult to interpret. For the investigation of lattice strain changes due to cyclic loading, where the 'signal-to-noise' ratio is expected to be small, it is necessary to estimate $U_{\text{c||s}}^m$.

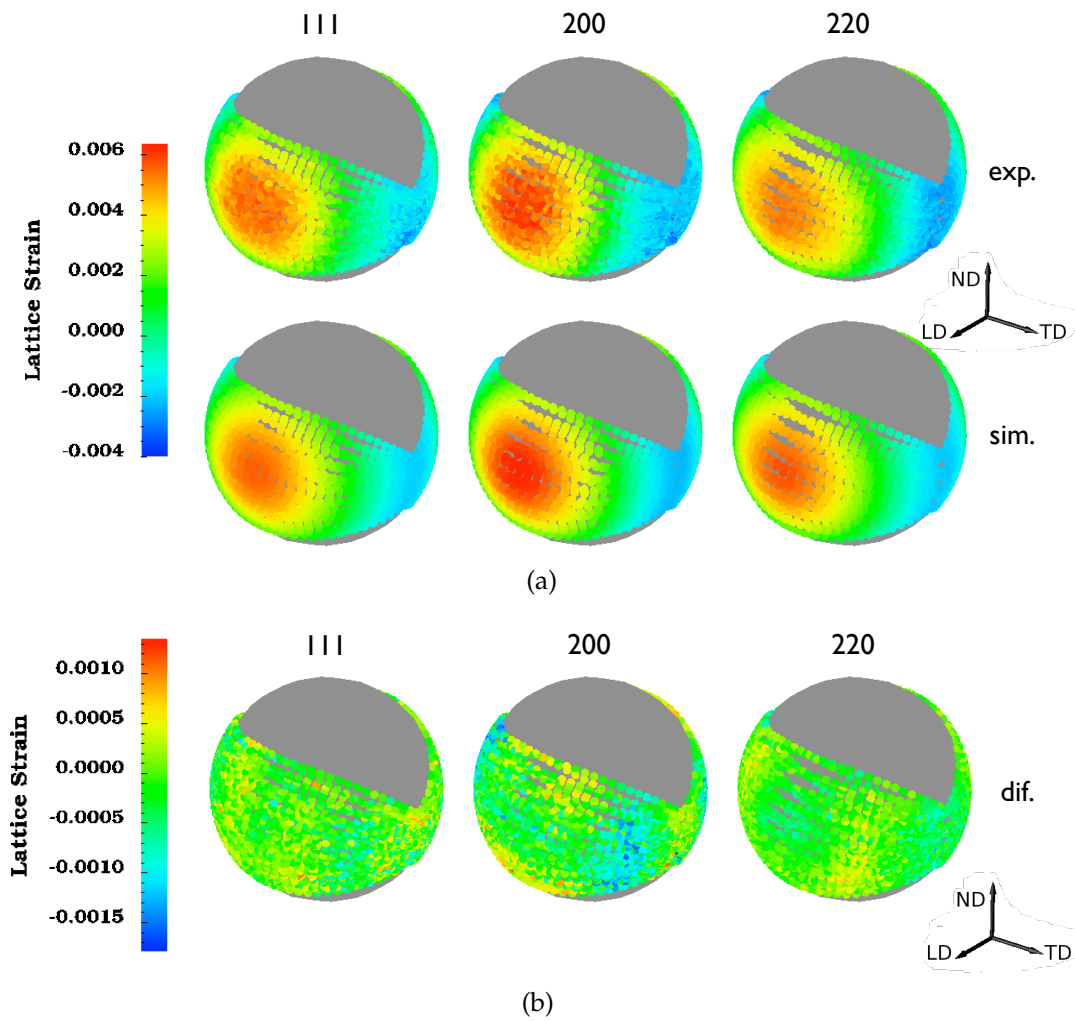


Figure 3.11: (a) The measured and the simulated SPFs at 400 MPa. The difference is provided in (b)

3.4.1 Estimating the Uncertainty Contribution from the Instru-

ment, $U_{c||s}^i$

The instrument in this case represents all aspects of the experimental configuration and data reduction software employed to determine a lattice strain value. A brief description the procedure used to quantify the instrument portion of the uncertainty for each measurement will be provided here. A more complete

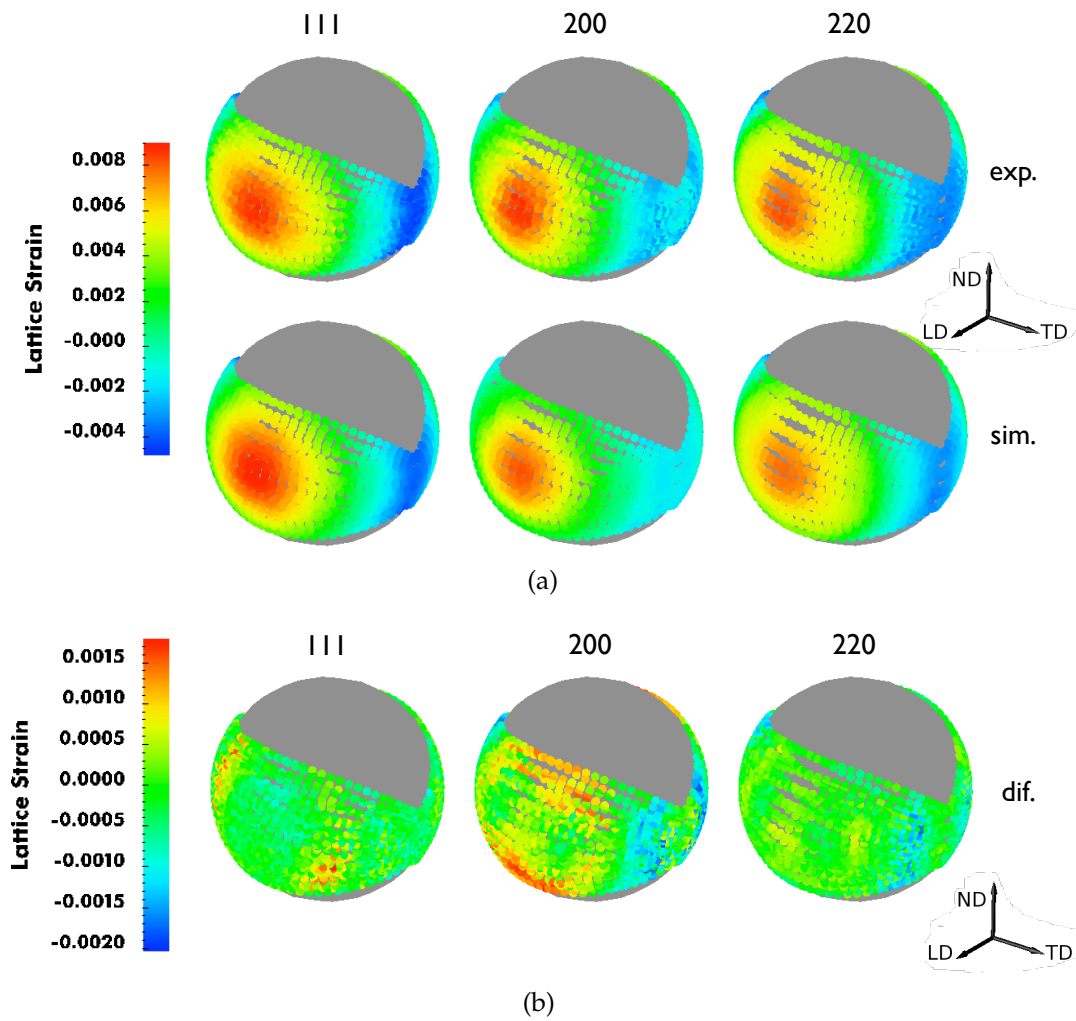


Figure 3.12: (a) The measured and the simulated SPFs at 515 MPa. (b) The difference is more pronounced than in the previous SPFS.

description of the procedure is available in [55].

The instrument portion of the uncertainty represents the limitations of the tool and is present for each measurement. The lattice strain resolution is defined by the smallest resolvable peak shift on the detector, $\delta\rho_{min}$, and the intensity (S) required to identify the position of the diffracted peaks. The model for the instrument portion of the uncertainty developed in [55], is defined to be the

superposition of separate terms for each aspect of the resolution,

$$U_{\text{cls}}^i = \left\{ \frac{\sin\left(\frac{\arctan\left(\frac{\rho}{D}\right)}{2}\right)}{\sin\left(\frac{\arctan\left(\frac{\rho - \delta\rho_{\min}}{D}\right)}{2}\right)} - 1 \right\} + S_{\alpha} \left(\frac{S_{\text{lim}}}{S} \right) \quad (3.7)$$

Here ρ and D were previously defined in Figure 3.2, S_{α} scales the intensity contribution to the instrument portion of the uncertainty, and S_{lim} is the maximum possible pixel value for the detector ($S_{\text{lim}} = 2^{16}$ for the MAR345 detector). The two model parameters, $\delta\rho_{\min}$ and S_{α} , are determined by applying the model to the unstrained calibrant material where the lattice strains are expected to be zero. A detailed development of the model for the instrument portion of the uncertainty can be found in [55].

Using the diffraction results from the CeO_2 calibrant insert, we determined the model parameters for Equation 3.7 for each load step. The mean and the standard deviation of the $\delta\rho_{\min}$ and S_{α} for all the load steps measured were found to be $2.84 \pm 0.05 \mu\text{m}$ and $(1.6 \pm .3) \times 10^{-8}$, respectively. These values for the model parameters agree well with those presented in [55]. Using Equation 3.7 the instrument portion of the uncertainty was determined for the exact position (ρ) and intensity (S) of the measured diffracted peaks.

3.4.2 Estimating the Uncertainty Contribution from the Material, U_{cls}^m , for AA7075-T6

To estimate the uncertainty associated with the material both the number of crystals interrogated by each measurement, and the variation in the stress state between these crystals must be considered. In essence, the minimum number of crystals required for each measurement to have the same lattice strain uncer-

tainty is coupled to the variability in the mechanical response. This variation in lattice strain between each crystal participating in a diffraction measurement is due to the anisotropic single crystal properties (elastic and plastic), the effect of neighboring grains, the type of loading, and the level of deformation. It is not possible to precisely discern the lattice strain variance from powder diffraction alone. The breadth of diffracted peaks contains information about the variance, but it is complicated by other sources such as the instrument broadening and the dislocation density of the material. To estimate the lattice strain variance we use the simulation for the same loading conditions.

As previously described, each diffraction measurement results in the mean lattice strain for the set of crystals crystals satisfying the diffraction condition (along a crystallographic fiber). If identical lattice strain measurements were made for different samples (same $c||s$ combination), the set of lattice strains would produce a distribution of mean values. From the central limit theorem in statistics, we expect that this set of lattice strains would approximate a normal distribution [24]. The material portion of the uncertainty is related to the standard deviation of this distribution of mean values. Using the central limit theorem, the standard deviation of the distribution of means values is defined [24],

$$\bar{\Psi}_{c||s} = \frac{\Psi_{c||s}}{\sqrt{G}} \quad (3.8)$$

Here $\Psi_{c||s}$ is the standard deviation for the set of diffracting crystals and G is the number of grains contributing to each measurement. To determine the uncertainty value for the measurement we combine $\bar{\Psi}_{c||s}$ with a confidence interval using the Student's t-distribution [25],

$$U_{c||s}^m = t\bar{\Psi}_{c||s} \quad (3.9)$$

Here t is a function of the degree of confidence and the number of crystal contributing to the lattice strain measurement (G). For our effort, the confidence level used was 95%. For G greater than 120, t approaches an asymptote at 1.96 and corresponds to 95% of the area under a standard normal curve. Values for t when G is below 120 are tabulated in [24].

Probable Number of Crystals per Measurement

The probable number of crystals that contribute to each lattice strain measurement is coupled to the set of orientations that satisfy Equation 3.2. Each point on a Debye ring (Figure 3.3(a)) corresponds to a specific point on a SPF and a fiber through orientation space. The relationship between a lattice strain measurement in LD for the $\{200\}$ SPF and the corresponding fiber is shown in Figure 3.13(a). The exact subset of orientations probed experimentally, however, is linked to a larger region in orientation space. For a 5° azimuthal (η) bin, like the one shown in Figure 3.3(b), the set of orientations that diffract correspond to a range of scattering vectors. In Figure 3.13(b) an SPF is shown with a 15° azimuthal bin on the SPF. The set of scattering vectors that contribute to a lattice strain measurement represent a region or patch on the SPF. For the SPF in Figure 3.13(b), the long dimension of the patch is defined by the η bin size and the short dimension is due to the finite range of orientations over which a single crystal diffracts. Consider a simple diffraction experiment where a single crystal is rotated at a constant speed about a fixed axis while a detector measures the intensity for each angular value. For our experimental configuration, the resulting plot of rotation angle versus intensity would show a peak with a full width half max (FWHM) of $\approx 0.3^\circ$. This 0.3° is the short dimension for the patch

shown in Figure 3.13(b). The set of orientations that contribute to a lattice strain measurement are represented by a set of fibers defined by the patch geometry and the $\{hkl\}$.

To increase the probable number of crystals that contribute to each lattice strain measurement we can change the experiment procedure such that more orientations are included. One method would be to increase the η bin size. This approach leads to the results being averaged over elongated patches on the sphere. Another option is to change the orientation of the sample during the diffraction measurement. By rotating, or rocking, the sample about a fixed (ω, χ) set, a different patch geometry can be defined. Consider three cases of sample rocking: $(\omega = \pm 10^\circ, \chi = 0^\circ)$, $(\omega = 0^\circ, \chi = \pm 10^\circ)$, and the results for the two rotations in series. The range of scattering vectors for the AA7075-T6 $\{111\}$ before azimuthal binning are shown in Figure 3.14. Rocking the sample during the diffraction measurement increases the range of scattering vectors considered for all three cases. For both Figure 3.14(a) and Figure 3.14(b), dividing the Debye rings into η bins would result in a different patch geometry for each bin. The amount of orientation space sampled would therefore be different for each measurement. This variable sampling can be minimized by rocking about two axes (ω, χ) in succession and the results are shown in Figure 3.14(c).

An example of a $\pm 2.5^\circ$ rock about both ω and χ produces a $5^\circ \times 5^\circ$ patch centered about LD for the $\{200\}$ SPF is shown in Figure 3.13(c). The corresponding group of fibers probes a larger portion of orientation space. Shifting between the configuration in Figure 3.13(b) to Figure 3.13(c) the aspect ratio (length to width) for the patch on the SPF over which the lattice strain response is averaged changes from 50:1 to 1:1. The patch geometry selected for the AA7075

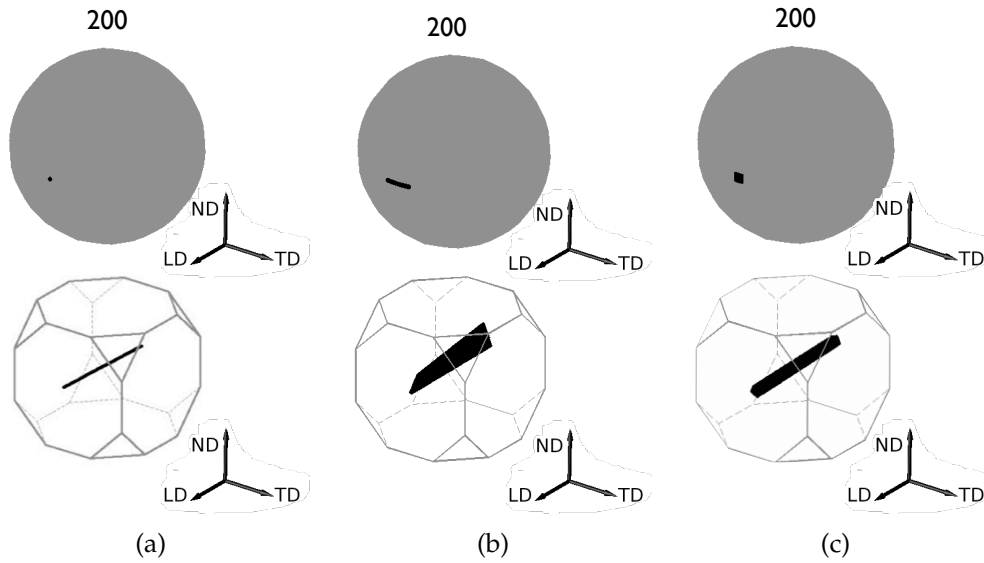


Figure 3.13: The relationship between a patch on the $\{200\}$ SPF and the corresponding region of orientation space interrogated is shown for (a) a point aligned with LD, (b) a $0.3^\circ \times 15^\circ$ patch centered about LD, and a $5^\circ \times 5^\circ$ patch centered about LD.

sample was a $5^\circ \times 5^\circ$ region on the SPF. This patch size is larger than a typical diffraction measurement (Figure 3.13(b)) to increase the number of crystals contributing to each measurement. The patch employed for the simulation was a 10° diameter circle about the center of each experimental patch. The simulation patch was selected to be larger than the patch used in the experiment to increase the number of elements within the simulation that contribute to each lattice strain measurement.

To determine the number of crystals that contributes to a patch on the SPF p , we need to account for crystal symmetries. For a cubic crystal there are 24 symmetry operators defined \mathcal{G}_i . The crystallographic multiplicity (M) is the number of unique vectors within the set defined $\mathcal{G}_i\mathbf{c}$ for all i . The multiplicity for the $\{hkl\}$ s considered are shown in Table 3.1.

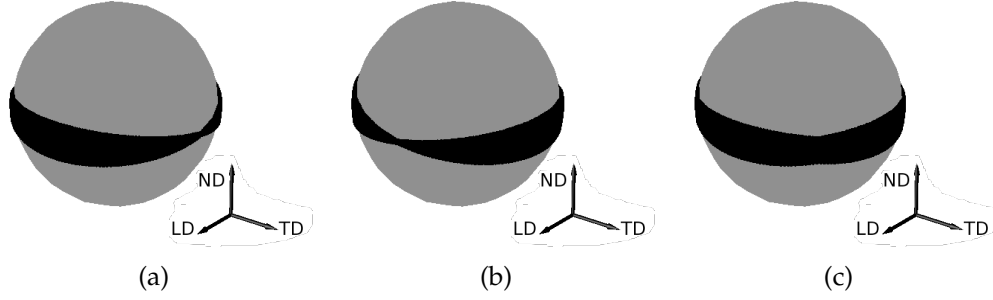


Figure 3.14: The scattering vectors for the AA7075-T6 $\{111\}$ lattice strain measurements due to rocking by (a) $\omega = \pm 10^\circ, \chi = 0^\circ$, (b) $\omega = 0^\circ, \chi = \pm 10^\circ$, and (c) the result of rocking by (a) and (b) in series.

The ODF over the fundamental zone is shown in Figure 3.5. To calculate the volume fraction of the ODF that contributes to a patch p , we must account for both the multiplicity and the antipodal symmetry on the SPF ($\pm s$ in Equation 3.2). The relationship between the volume fraction of the material interrogated within the physical sample and the volume fraction of the ODF sampled can be written as,

$$\frac{V_c G}{V_\beta} = \frac{M \int_p (\int_{c||s} f(\mathbf{R}) dR) ds}{\int_{sphere} (\int_{c||s} f(\mathbf{R}) dR) ds} \quad (3.10)$$

Here V_c is the average volume of a single crystal. Recall that V_β is the volume of irradiated material, $f(\mathbf{R})$ is the ODF, p is the patch on the sphere, and M is the multiplicity. As the sample is rotated V_β changes and the minimum value occurs when ND is aligned with the incoming x-ray. The expression can be rewritten for the probable number of crystals as,

$$G = \frac{M V_\beta \int_p (\int_{c||s} f(\mathbf{R}) dR) ds}{V_c \int_{sphere} (\int_{c||s} f(\mathbf{R}) dR) ds} \quad (3.11)$$

This expression assumes that the patch size is sufficiently small such that each crystal contributes at most one time to a patch. As the patch size increases, it is

no longer possible to scale the results by the multiplicity. Moreover, if the multiplicity for an $\{hkl\}$ does not include the antipodal symmetry, then this expression would underestimate the number of orientations that contribute to each measurement.

For the general case we define the pole projection operator \mathcal{P}_c such that,

$$\mathcal{P}_c \mathbf{R} = \mathbf{R} \mathbf{c} \quad (3.12)$$

Using the inverse of the projection operator we can represent all the orientations that when projected contribute to a patch p ,

$$\mathcal{F}_{c,p} = \mathcal{P}_c^{-1} \mathbf{s} \cup (\mathbf{s} \in p) \quad (3.13)$$

where $\mathbf{c}_i = \mathcal{G}_i \mathbf{c}$. Now the relationship between the volume fractions can be defined as,

$$\frac{V_c G}{V_\beta} = \frac{\int_{\mathcal{F}_{c,(p \cup -p)}} f(\mathbf{R}) dR}{\int_{V_\Omega} f(\mathbf{R}) dR} \quad (3.14)$$

Table 3.1: Multiplicity values for the $\{hkl\}_s$ considered.

$\{hkl\}_s$	111	200	220
Multiplicity (M)	8	6	12

Using Equation 3.11, the average grain size of $\sim 19.5 \mu m$, and the ODF presented in Figure 3.5 we find the probable number of grains contributing to each measurement and the results are shown in Figure 3.15(a). The exact number of elements within the simulation that contributes to each lattice strain value and the results are shown in Figure 3.15(b). The qualitative similarities between Figure 3.15(a) and Figure 3.15(b) are expected since the ODF is used to estimate the number of crystals and assign orientations to each element in the virtual specimen.

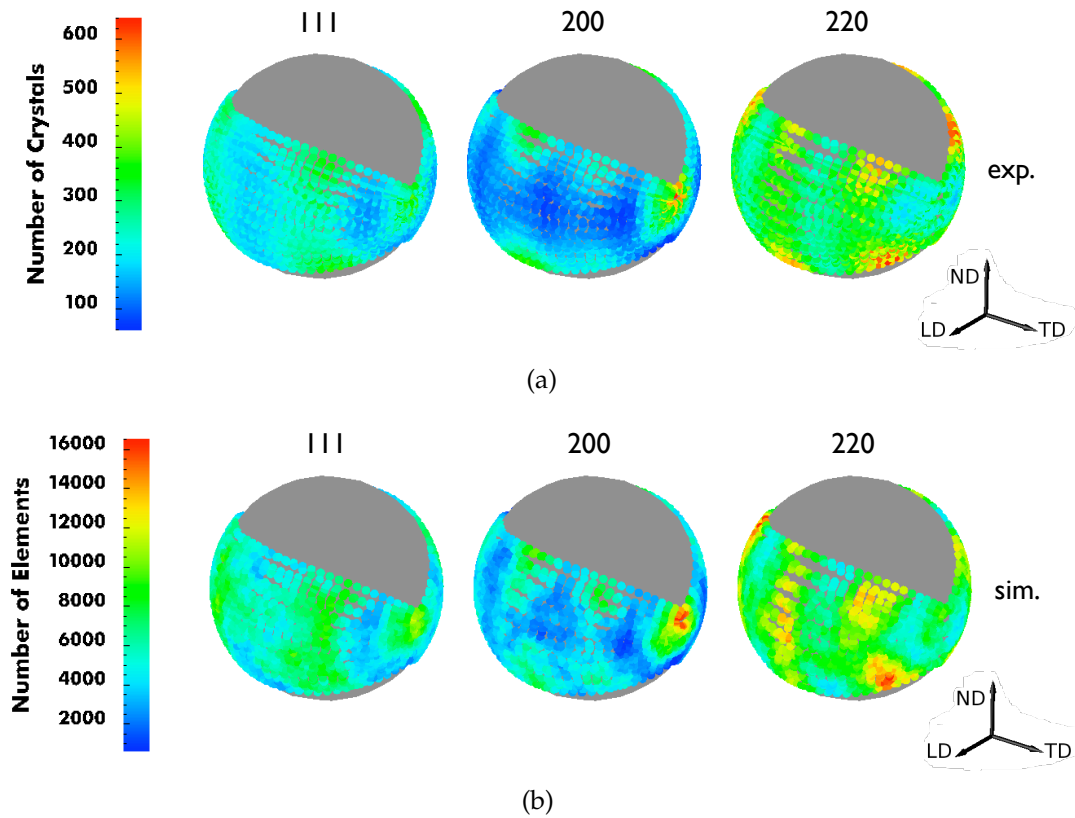


Figure 3.15: (a) The probable number of grains that contribute to each measurement and (b) the number of elements contributing to each simulated lattice strain are shown for each $\{hkl\}$.

Lattice Strain Standard Deviation, Ψ_{ells}

The standard deviation for each lattice strain measurement is coupled to the anisotropy of the single crystal properties, the deformation history, and the number of grains contributing to the measurement. Recall that the diffracting crystals satisfy Equation 3.2 and each crystal has a different set of neighboring grains. The simulated lattice strain standard deviations at 0, 135, 400, and 515 MPa are shown in Figure 3.16. Initially the lattice strain for each element is zero by definition, and standard deviation is shown in Figure 3.16(a) is zero. As expected, the standard deviation increases with increasing load in a nonuniform

manner, particular post yield and is shown in Figure 3.16(b), Figure 3.16(c), and Figure 3.16(d). This evolution impacts the interpretation of the measured lattice strains. For a fixed number of grains per measurement, the evolving standard deviation results in a variation in the lattice strain uncertainty. The patterns shown in Figure 3.16(d) are an indication of the orientation dependence of the variation in the stress states between the grains that make up each measurement. It is worth noting that the minimum lattice strain standard deviation is in the loading direction for each $\{hkl\}$.

3.4.3 Lattice Strain Uncertainty Results

Due to the complexity in the response of deforming polycrystals, the importance of separating 'signal' from 'noise' is important for investigating complex deformation phenomena. The interpretation of lattice strains as indications of meaningful material evolution is dependent on the uncertainty in each measurement. False interpretation of subtle lattice strain changes as material evolution instead of experimental fluctuations could cloud our understanding of the grain scale deformation. The lattice strain uncertainty, calculated using Equation 3.6, is shown as \pm values in Figure 3.17(a). The largest uncertainty occurs below TD on the $\{200\}$ SPF. This corresponds to a region on the SPF where both the probable number of crystals per measurement is low and the lattice strain standard deviation is high. The lowest uncertainty occurs for the $\{220\}$ SPF due to the high multiplicity resulting in more crystals contributing to each measurement.

Recall that the initialization of the orientation for each element in the virtual sample is done by randomly sampling the ODF. The simulated lattice strains

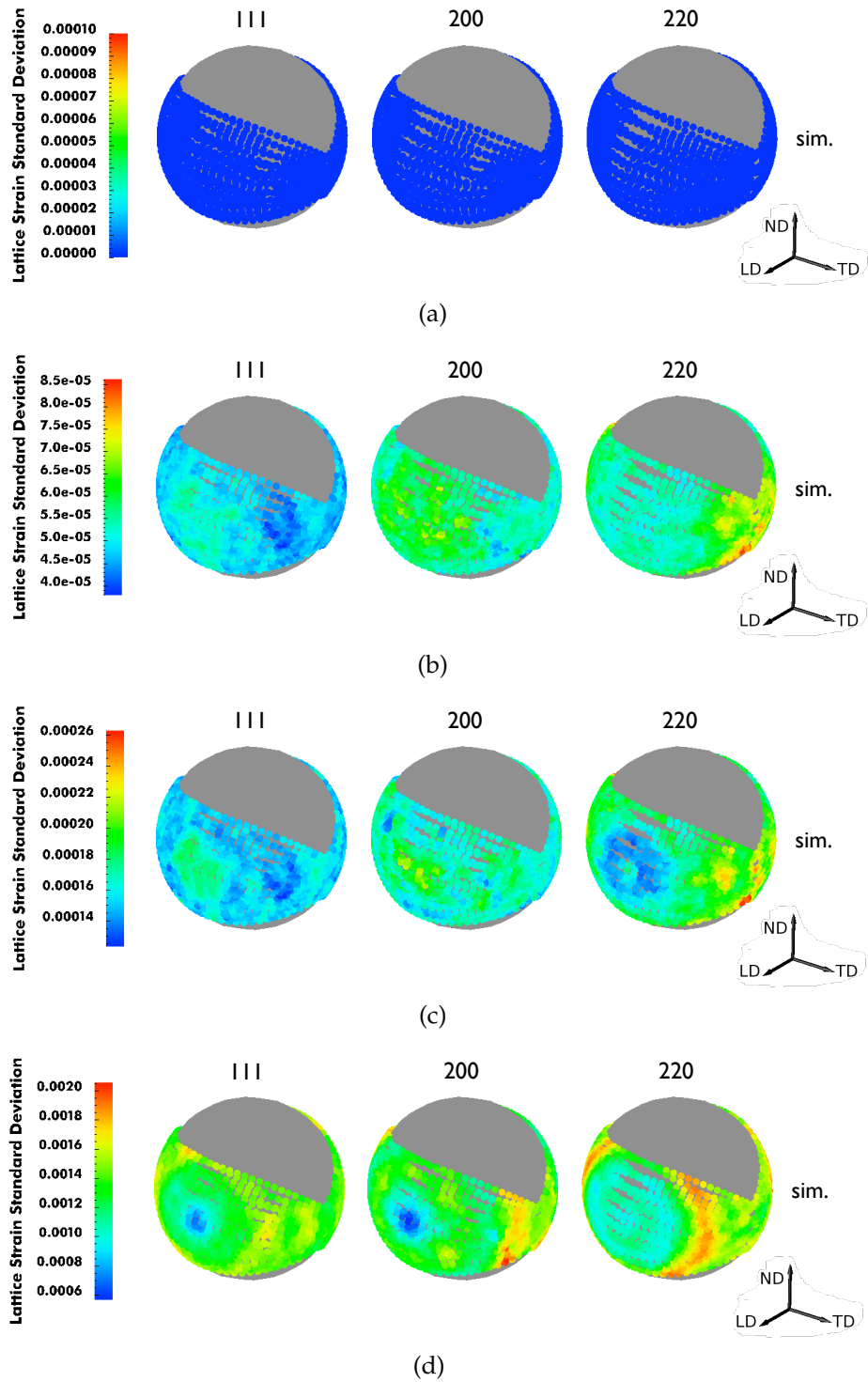


Figure 3.16: The standard deviation of the simulated lattice strains are shown at (a) 0 MPa, (b) 135 MPa, (c) 400 MPa, and (d) 515 MPa.

are the mean value for the elements that satisfy the diffraction condition. If the simulation was run again with a different random sampling of the ODF, some variation in the lattice strains is expected. In an analogous manner to the measured lattice strains, if the simulation was conducted several times with different initial orientations assigned to each element we could build a distribution of simulated lattice strain values (for the same $\mathbf{c}||\mathbf{s}$ combination). The mean of this distribution of simulated lattice strains is the true simulated lattice strain value. Using the central limit theorem, we expect that true simulated mean for the lattice strain results to be related to the number of elements sampled and the variation between the simulated lattice strains for each element [24]. To estimate the uncertainty in the simulated lattice strains we use Equation 3.9, with the number of elements instead of the number of crystals. The resulting uncertainties are shown in Figure 3.17(b). The trends in the lattice strain uncertainty between the simulation and experiment are similar, but the uncertainty in the simulated results is much lower.

Grouping Lattice Strain Results

An advantage of synchrotron x-rays and area detectors is the ability to quickly accumulate lattice strains for many scattering vectors. If we define a circular region \mathcal{B} on the SPF, we can average the measurements that fall within the region,

$$\epsilon_{\mathbf{c}||\mathcal{B}} = \frac{\sum_{j=1}^{\mathcal{N}} \epsilon_{\mathbf{c}||\mathbf{j}}}{\mathcal{N}} \quad (3.15)$$

Here j represents a measurement in \mathcal{B} and \mathcal{N} is the number of measurements included in the average. The benefit to using Equation 3.15 is that the mean lattice strain over a region \mathcal{B} will have a lower uncertainty than the contributing measurements. The underlying process by which this occurs is that the ‘signal’

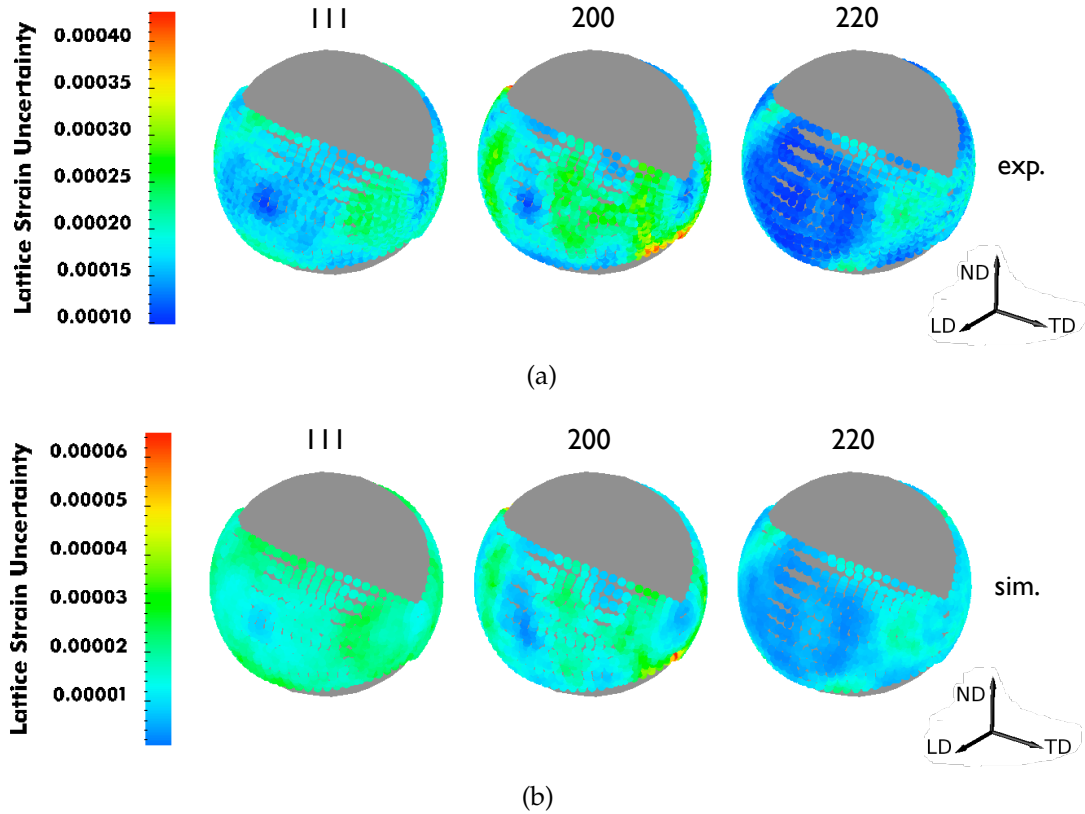


Figure 3.17: (a) The experimental lattice strain uncertainty is plotted for each measurement. The region with the highest uncertainty occurs on the $\{200\}$ SPF below TD. (b) The lattice strain uncertainty for the simulated results was determined using Equation 3.9.

adds, whereas the random error present in each measurement cancels with the addition of more independent measurements. To estimate the uncertainty for the grouped results we use the uncertainties for each measurement and common error propagation techniques. For two measurements with known uncertainties, $m_1 \pm u_1$ and $m_2 \pm u_2$, the uncertainty for $m_1 + m_2$ is defined [25],

$$u_{1+2} = \sqrt{u_1^2 + u_2^2} \quad (3.16)$$

The uncertainty for the division of the same two quantities is [25],

$$u_{1/2} = \sqrt{\left(\frac{m_1}{m_2}\right)^2 \left[\left(\frac{u_1}{m_1}\right)^2 + \left(\frac{u_2}{m_2}\right)^2 \right]} \quad (3.17)$$

Combining these expressions we estimate the uncertainty for the region \mathcal{B} on the SPF as,

$$U_{c||\mathcal{B}} = \sqrt{\left(\frac{\sum_{j=1}^{\mathcal{N}} U_{c||j}}{\sum_{j=1}^{\mathcal{N}} \epsilon_{c||j}}\right)^2} \epsilon_{c||\mathcal{B}}^2 \quad (3.18)$$

A demonstration of this process with \mathcal{B} defined to have a 5° radius is shown for the lattice strains measured at 515MPa. The mean lattice strain results are shown in Figure 3.18(a). The total number of measurements that were averaged in each \mathcal{B} are shown in Figure 3.18(b). The largest number of measurements is 29 and occurs near TD for the $\{111\}$. The uncertainties after grouping the measurements are shown in Figure 3.18(c) and are significantly lower than those in Figure 3.17(a). The tradeoff between grouping and individual lattice strain measurements is lower uncertainty values versus angular resolution on the SPF, respectively.

3.5 Cyclic Lattice Strain Results

The AA7075-T6 sample underwent zero-tension cyclic loading with a peak value of 572 MPa. The complete macroscopic stress-strain curve for the sample is shown in Figure 3.19. The SPFs were measured at 515MPa (90% of the peak load) at many points during the cyclic deformation. Since lattice strains are coupled to the crystal level stresses, the evolution of the lattice strains during fixed stress amplitude loading are expected to be small. To ensure that any cycle-by-cycle variation in the lattice strains is visible on the SPFs, we present

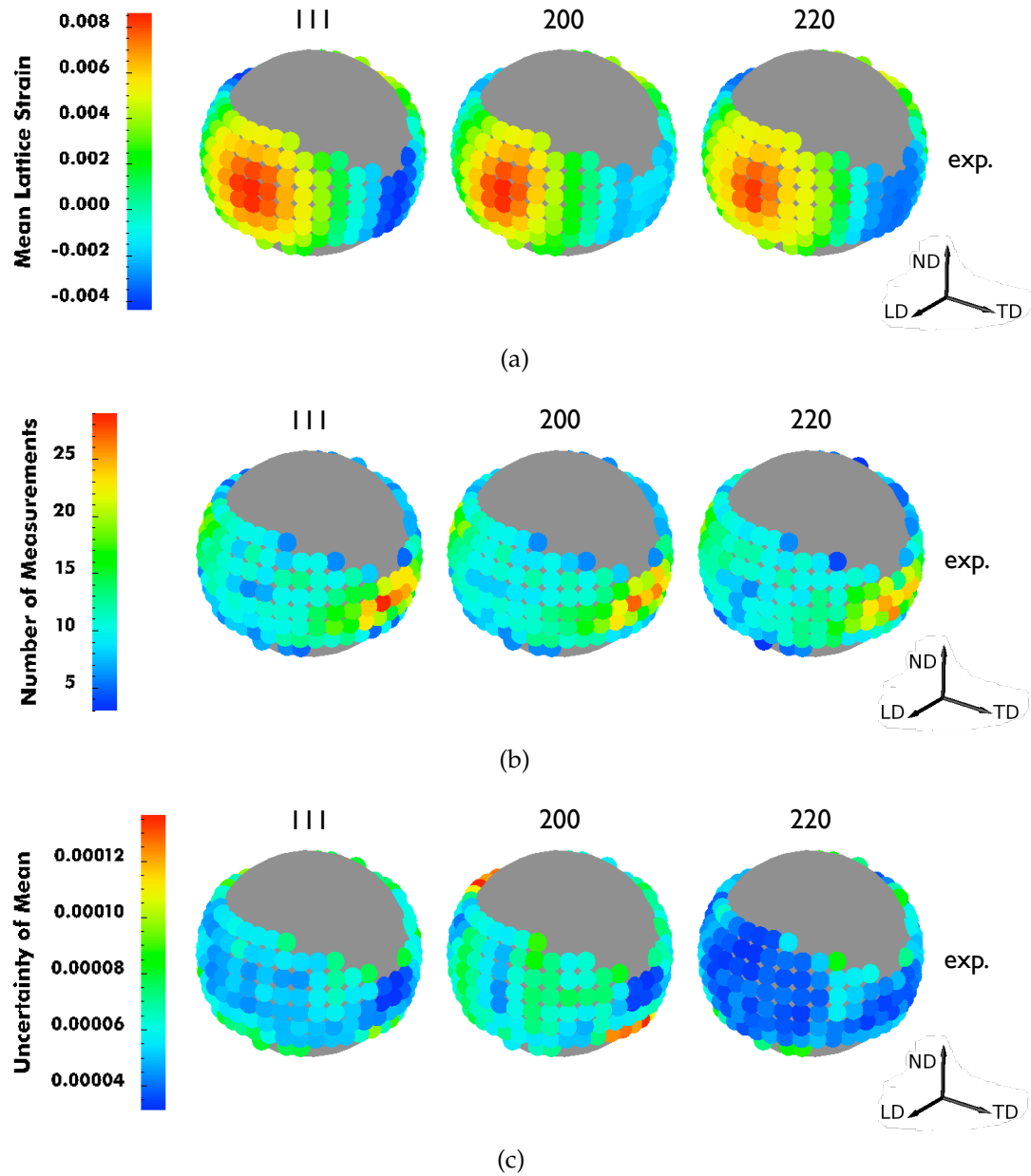


Figure 3.18: (a) The mean of the measured lattice strains at 515MPa within a 5° radius circle about each glyph. (b) The number of measurements included in each grouping is shown. (c) The uncertainties for the mean lattice strain results are shown for the same points presented in (a) and (b).

each SPF as the difference between the cycle of interest and the cycle zero results (i.e. the first cycle is identified by 1-0). The cycle zero results were shown previously in Figure 3.12(a). The results for cycle 1-0, 10-0, and 100-0 are shown in Figure 3.20. The magnitude of the lattice strains in Figure 3.20 are on the same order as the uncertainty results shown in Figure 3.17(a). There is a slight increase in the lattice strains near LD for all three $\{hkl\}$ s. The scale for the SPFs in Figure 3.20 is biased by a few scattering vectors. To improve the ‘signal-to-noise’ ratio we will group the cyclic SPF results using the 5^o region employed in Figure 3.18.

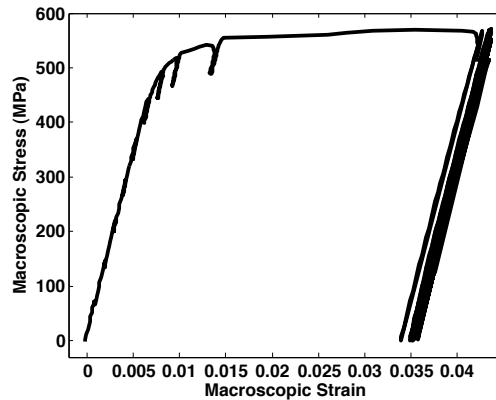


Figure 3.19: The macroscopic stress-strain curve for the AA7075-T6 sample. The sample was cycled between 0 and 572 MPa. The sample failed after 1588 cycles.

The uncertainties for the grouped lattice strains are lower than those for individual measurements. The grouped lattice strain results for the SPFs shown in Figure 3.20 are presented in Figure 3.21. The grouped results shown the lattice strains are increasing near LD for all three $\{hkl\}$ s. The $\{200\}$ SPFs also show increasingly compressive lattice strains near TD. By comparing the results in Figure 3.21 with the uncertainties in Figure 3.18(c), we find the lattice strain evolution due to cyclic loading to be above the level of the ‘noise’. In addition to

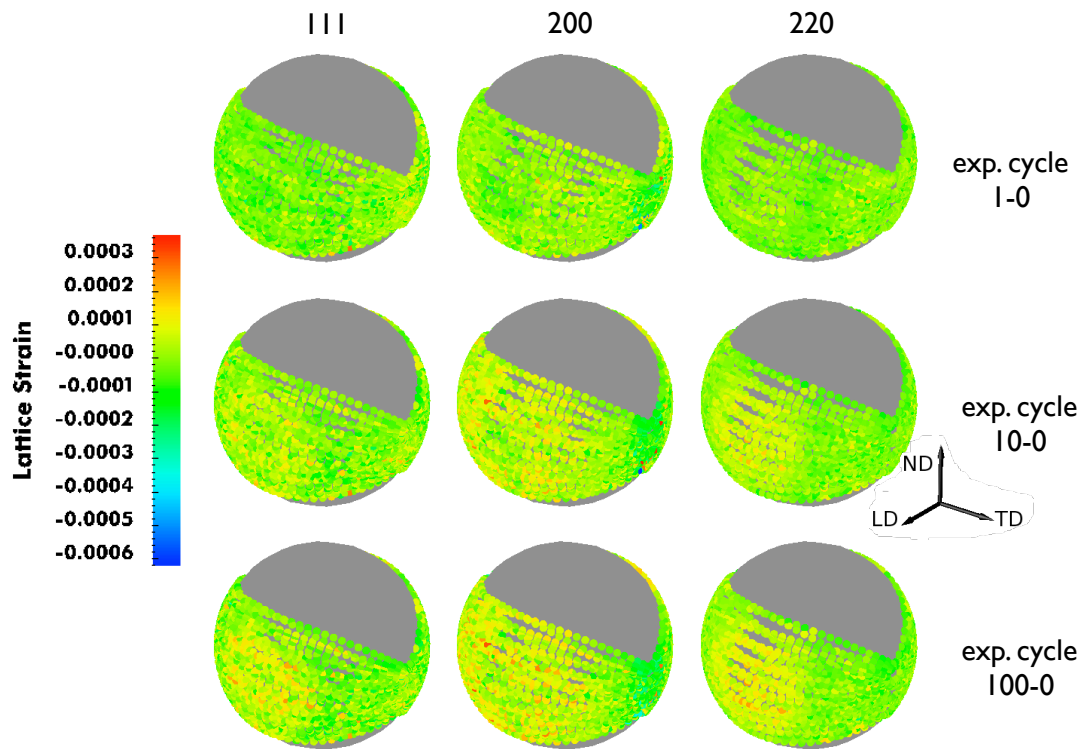


Figure 3.20: The cyclic lattice strains for each $\{hkl\}$ are shown as a difference between the cycle of interest and cycle zero at 515 MPa. The difference SPFs are shown for cycles 1-0, 10-0, and 100-0, respectively.

the increased signal, the smooth variation between neighboring measurements on the SPF lends confidence to these trends beyond that possible for a lone measurement.

From the SPFs alone it is difficult to determine whether the lattice strain evolution is constant throughout the fatigue life or whether it occurs more rapidly during a particular portion. To investigate the overall magnitude of the lattice strain evolution with increasing cyclic deformation we calculate a root mean squared (RMS) value for each cycle. We define the SPF RMS to combine lattice strains from each $\{hkl\}$ and use the uncertainty to weight the contribution of each

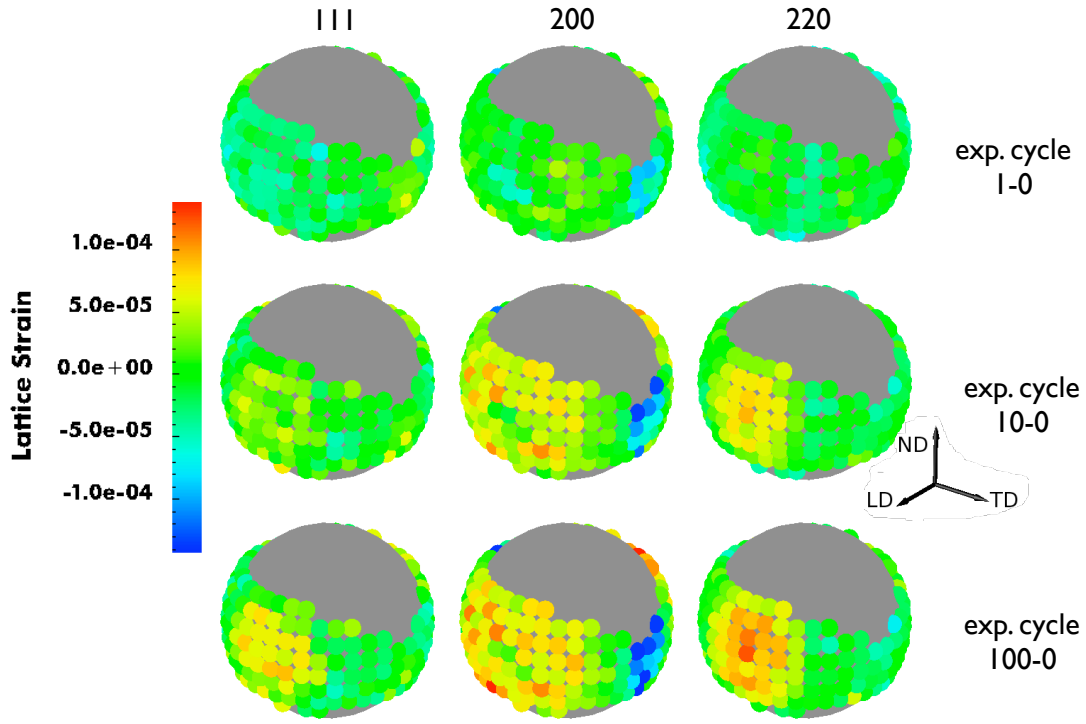


Figure 3.21: The cyclic lattice strains in Figure 3.20 are presented after grouping the results within 5° regions. The grouped difference SPFs are shown for 1-0, 10-0, and 100-0, respectively.

measurement,

$$\Delta\epsilon^{RMS} = \sqrt{\sum_{i=1}^{\mathcal{H}} \sum_{j=1}^{\mathcal{N}} w_{i||j} \Delta\epsilon_{i||j}^2} \quad (3.19)$$

Here $\Delta\epsilon_{i||j}$ is the difference values shown in Figure 3.21, \mathcal{N} is the number of measurements, \mathcal{H} is the number of $\{hkl\}$ s, and $w_{i||j}$ is a weight based on the uncertainty in each measurement defined,

$$w_{i||j} = \frac{1/U_{i||j}^2}{\sum_{l=1}^{\mathcal{H}} \sum_{k=1}^{\mathcal{N}} 1/U_{i||k}^2} \quad (3.20)$$

The SPF RMS is shown with increasing cycles in Figure 3.22. The SPF RMS, which combines information from 5184 independent lattice strain measurements, shows that the majority of the lattice strain evolution occurs during

the first portion of the samples fatigue life. The lattice strain evolution occurs rapidly for the first 50 cycles, and slow as the sample approaches failure after 1588 cycles. It is worth noting that the magnitude of $\Delta\epsilon^{RMS}$ is less than the peak values in Figure 3.21 since it incorporates many scattering vectors with little or no lattice strain evolution.

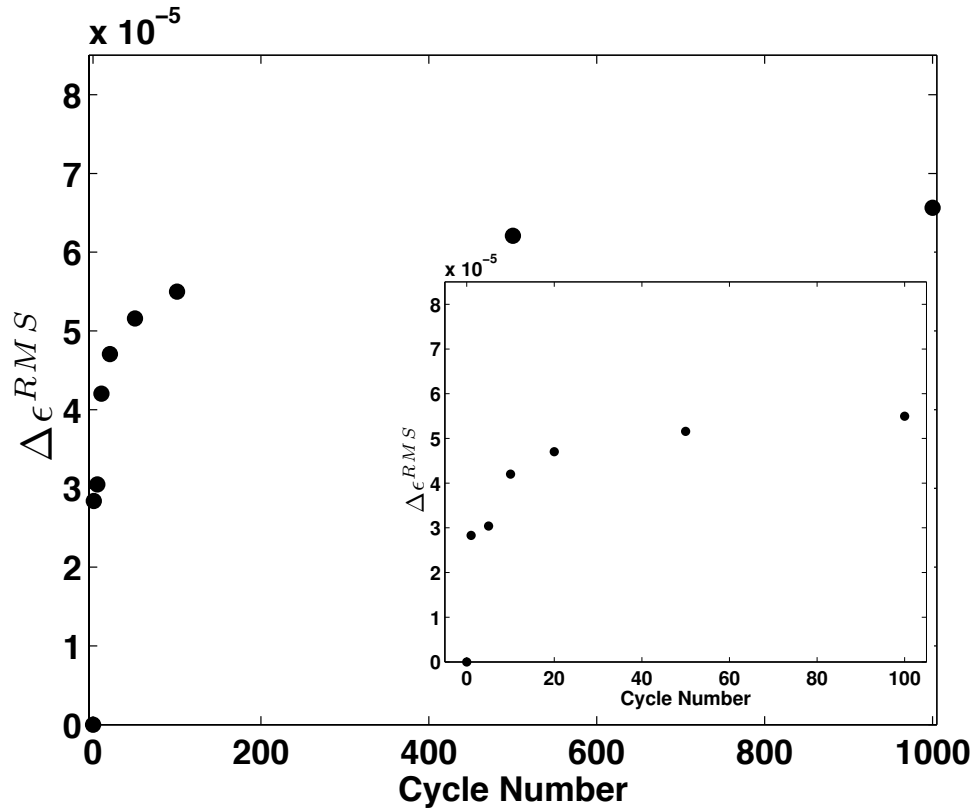


Figure 3.22: The SPF RMS is shown with increasing cycles. The sample failed after 1588 cycles. The insert shows the SPF RMS for the first 100 cycles.

3.6 Discussion

Integrating SPF data with crystal-based finite element simulations, beyond the comparison of lattice strains in a few directions, provides a new tool to study

complex phenomena like the evolution of lattice strains due to cyclic loading. Interpreting the variation in lattice strains during fixed stress amplitude cyclic loading as ‘signal’ or ‘noise’ is an important step toward understanding how the crystal level stresses evolve prior to the initiation of a fatigue life limiting defect. With a precise estimate of the ‘worth’ of each measurement we can separate experimental fluctuations from material evolution and identify lattice strain changes due to cyclic loading. The discussion will focus on the cyclic lattice strain evolution and the integration of the SPF experiment with crystal-based finite elements simulations.

3.6.1 Cyclic Lattice Strain Evolution

Recall that each lattice strain measurement is the average normal strain for the set of diffracting crystals. Cycle-by-cycle variation in the crystal level stresses is manifested on the SPFs as lattice strain evolution. For the first time, evidence that the crystal level stresses evolve rapidly during the earliest portion of the samples fatigue life during fixed amplitude cyclic loading in a polycrystal has been quantified. With this discovery comes the opportunity to develop new theories to explain the measured trends.

One such hypothesis for why the lattice strains evolve rapidly at first, and then less as the sample approaches failure is linked to the Single Crystal Yield Surface (SCYS) [36, 53]. The SCYS is a five-dimensional faced surface in deviatoric stress space. Each facet is defined by the stress state necessary to activate a particular slip system. The intersection of two facets form an edge, where two slip systems are active. The intersection of fives edges is defined as a ver-

tex. When the stress state is in a vertex of the SCYS, polyslip (accommodating general deformation) can occur. It has been shown that during large scale deformation the crystal stresses reach the SCYS, and then the stress moves toward a vertex [53].

The level of deformation experienced by the AA7075-T6 is insufficient to expect the majority of the crystal stresses to be in a vertex of the SCYS. However, it is likely that during each cycle the stress state experienced by some crystals is sufficient to cause yielding. As these crystals yield, the stress state could shift slightly along the SCYS in the direction of the nearest vertex. It may be possible that the progression toward a vertex under fixed stress amplitude loading is limited, and that with each cycle the number of crystals within the sample that yield decreases. This reduction in the number of plastically deforming crystals would correspond with less evolution of the crystal level stresses, and the leveling off of the SPF RMS value with increasing cycles. In addition, if the leveling of the SPF RMS correlates with sample failure for both other samples and different materials, it may be possible to use $\Delta\epsilon^{RMS}$ to estimate the number of cycles remaining prior to failure.

3.6.2 Integrating the Experiment and Simulation

In addition to the ability to estimate the material contribution to the lattice strain uncertainty, the connection with the simulation provides an opportunity for more in depth investigations. In a parallel effort [71], the cyclic response of the AA7075-T6 sample was simulated for the same loading condition. The simulated SPFs also shown lattice strain evolution with increasing cycles near LD,

but the magnitude of the evolution is significantly less. Going beyond direct comparison with the SPFs, the simulation can also be used to conduct parameter studies to discern the most influential material properties, investigate the role of the SCYS during cyclic loading, and use the full spatial information in the simulation to investigate the stresses at the crystal level directly. Since the orientation of each element in the simulation is known, the simulation results can also be used to determine the most likely stress for each orientation. Variation in the stress over orientation space during cyclic loading, if limited to certain orientations, may prove to be likely initiation sites for fatigue life limiting defects.

Residual Lattice Strains

Currently the integration of SPF experiments and crystal-based simulations is complicated by the presence of a residual lattice strain distribution in the material as shown by the SPFs in Figure 3.9. Incorporating a residual lattice strain distribution into the simulation is a nontrivial task. Such a procedure would require initializing the simulation with a nonzero elastic strain tensor for each element such that the simulated residual lattice strains match those measured experimentally. This initial distribution would not be unique since the SPFs do not convey spatial information. Obtaining this match while satisfying equilibrium would be difficult. Moreover, due to the presence of the residual lattice strain, it is not possible to use the simulated lattice strain standard deviation to quantify the uncertainty prior to loading. It is possible an estimate of the standard deviation based on the single crystal elastic anisotropy may be a viable alternative.

Patch Geometry and Grouping Measurements on the SPF

Lattice strain data are represented in two ways on the SPF: the patch, p , for individual measurements and the region, \mathcal{B} , over which lattice strains are grouped. Both p and \mathcal{B} are regions on the SPF, but they represent distinctly different quantities. The patch (p) on the SPF represents the set of scattering vectors that make up each measurement. Specifying a patch on the SPF fixes the set of orientations that contribute to each measurement (Figure 3.13) and is directly related to the centroid of each diffracted peak used to calculate lattice strain. Accurately representing the set of orientations contributing to each measurement is important for interpreting lattice strain results.

Typically diffraction data measured with an area detector produce elongated patches with high aspect ratios (length to width) and low surface areas (Figure 3.13(b)). By reorienting or rocking the sample during a diffraction measurement the patch size and shape can be adjusted to change the number of crystals contributing to each measurement. The use of rocking enables the application of the SPF technique to study materials with larger average grain sizes. Moreover, the patch size and shape used in the experiment should be similar to that applied to the simulation results to ensure that the measured and simulated lattice strains can be compared one-to-one.

The massive numbers of lattices represented on the SPFs in Figure 3.20 enable new approaches to interpreting the lattice strain results. Grouped lattice strain results, like those shown in Figure 3.18 and Figure 3.21, represent the mean lattice strain value for a selected region, \mathcal{B} . Since combining measurements results in the 'signal' adding and the 'noise' canceling, grouped data produces results with lower uncertainties beyond what is possible with an individ-

ual measurement.

A single region \mathcal{B} , contains lattice strain information from many different patches. The key difference between p and \mathcal{B} is that p represents the exact set of scattering vectors which contributed to the individual lattice strain measurement (diffracted peak) and \mathcal{B} is used as a post-processing tool which sacrifices angular resolution on the SPF for lower uncertainties in the grouped lattice strain results.

3.7 Summary /Conclusions

Investigations of the crystal level stresses during cyclic deformation are important for understanding the micromechanical conditions which drive the initiation of fatigue life limiting defects. Quantifying the evolution of these stresses during cyclic loading has remained a challenge within the field of mechanics of materials. Measurement of lattice strains, which are coupled to the crystal stresses, provide the means to investigate the stress state at the crystal level. The goal of this effort was to quantifying the lattice strain evolution during zero-tension fixed stress amplitude cyclic loading of an aluminum alloy 7075-T6 (AA7075-T6) sample.

During fixed stress amplitude loading, the magnitude of lattice strain evolution is expected to be small. To interpret the results as 'signal' or 'noise' a new methodology that combines x-ray diffraction with *in situ* mechanical testing and crystal-based finite element simulations was developed. Previous investigations have focused on corroborating simulated and measure lattice strains in relatively few directions. Capitalizing on the recent availability of high rate x-

ray detectors, we have generated massive amounts of lattice strain data which enabled more than corroboration, but rather the union of crystal-based finite element simulations and diffraction experiments to provide a more complete picture of the stress state at the grain scale within a deforming polycrystal. This approach enables the evolution of lattice strains due to cyclic loading to be interpreted as experimental fluctuations or material evolution. Key findings include:

- The lattice strain evolution due to fixed stress amplitude loading is small, but measurable. The lattice strains are increasing due to cyclic loading near the loading direction for the $\{111\}$, $\{200\}$, and the $\{220\}$ crystallographic families. The results also show the lattice strains are becoming more compressive near the transverse direction for the $\{200\}$.
- Investigation of the the root mean square (RMS) of the lattice strain results show most of the lattice strain evolution occurs during the earliest portion of the samples fatigue life. The RMS values appear to reach an asymptote prior to the sample failing. It may be possible to use the RMS of the lattice strains to predict the number of cycles remaining prior to fatigue failure.
- The interpretation of lattice strains is linked to an estimate of the uncertainty. Each lattice strain measurement is a statistical sampling problem. To estimate the uncertainty we combine the probable number of crystals expected for each measurement with the simulated lattice strain standard deviation. In essence, the uncertainty is not just related to the number of diffracting crystals, but the variability in the lattice strain between these crystals.
- The finite element simulation enables us to calculated the lattice strain standard deviation from the elements in the simulation oriented to satisfy

the diffraction condition. This robust estimate for the variation between the diffracting crystals enables the interpretation of subtle lattice strain evolution as ‘signal’ or ‘noise’.

- A benefit of measuring massive numbers of lattice strains is that new regions of interest can be defined on the lattice strain pole figures and the results can be averaged. This procedure trades angular resolution on the pole figures for a mean value with an uncertainty lower than the contributing measurements. This smoothing process aids in identifying subtle trends like the evolution of lattice strains during cyclic loading.

3.8 Acknowledgments

The work on was supported financially by the Air Force Office of Scientific Research under grant/contract number FA9550-06-1-0168 (Dr. Jaimie Tiley, program manager). The work is based upon research conducted at the Cornell High Energy Synchrotron Source (CHESS) which is supported by the National Science Foundation under award DMR-0225180. Dr. Alexander Kazimirov of CHESS is explicitly acknowledged for his ongoing support of our experimental effort at the A2 station. The material was provided by ALCOA.

CHAPTER 4

SUMMARY

The lattice Strain Pole Figure (SPF) experiment combines high energy x-ray diffraction with *in situ* mechanical loading to measure lattice strains within a deforming polycrystal. Such investigations into the stress driven deformation mechanisms active at the grain scale have immense potential to produce results that challenge our intuition. Interpretation of these results, particularly where the “signal-to-noise” ratio is expectedly small, requires a shift of the SPF experiment from a one-off style experiment to a measurement capability. The prominent contributions of this dissertation include:

- The interconnected nature of the SPF coverage and the regions of orientation space probed was explored and a new metric was developed for optimizing the selection of SPF measurements.
- A new framework was proposed for the lattice strain uncertainty that separates the contributions from the instrument employed and material under investigation.
- A new model for the instrument portion of the uncertainty-based on the lattice strain resolution was developed. Using this model the instrument portion of the uncertainty can be determined from the exact position and intensity values of each diffracted peak measured with the area detector.
- The integration of crystal-based finite element simulations and diffraction-based lattice strain experiments enables a more complete picture of the micromechanical response. The feedback between the experiment and simulation at the grain scale provides a new basis for investigating deformation phenomena at the grain scale.

- The interpretation of lattice strains is linked to an estimate of the uncertainty. Each diffraction measurement is a statistical sampling problem. The material contribution to the lattice strain uncertainty can be estimated using the probable number of contributing crystals and the variability in the lattice strain between these crystals. A finite element simulation can be used to approximate this variation in the lattice strains. Without an estimate of the variation between the diffracting crystals it is not possible to interpret subtle evolution as “signal or noise”.
- Lattice strains measured during fixed stress amplitude cyclic loading of an aluminum alloy 7075-T6 sample evolve with increasing cycles. The majority of the lattice strain evolution occurs during the earliest portion of the samples fatigue life and slows prior to failure.

BIBLIOGRAPHY

- [1] C. C. Aydiner, J. V. Bernier, B. Clausen, U. Lienert, C. N. Tome, and D. W. Brown. Evolution of stress in individual grains and twins in a magnesium alloy aggregate. *Physical Review B (Condensed Matter and Materials Physics)*, 80(2):024113, 2009.
- [2] N. R. Barton, D. E. Boyce, and P. R. Dawson. Pole figure inversion using finite elements over rodrigues space. *Textures and Microstructures*, 35:113–144, Jan 2002.
- [3] H. Behnken. Strain-function method for the direct evaluation of intergranular strains and stresses. *physica status solidi (a)*, 177(2):401–418, 2000.
- [4] J. V. Bernier and M. P. Miller. A direct method for the determination of the mean orientation-dependent elastic strains and stresses in polycrystalline materials from strain pole figures. *Journal of Applied Crystallography*, 39(3):358–368, Jun 2006.
- [5] J. V. Bernier, J. S. Park, A. L. Pilchak, M. G. Glavicic, and M. P. Miller. Measuring stress distributions in Ti-6Al-4V using synchrotron x-ray diffraction. *Metallurgical and Materials Transactions A*, 39(13):3120–3133, 12 2008.
- [6] Joel V. Bernier, Matthew P. Miller, Jun-Sang Park, and Ulrich Lienert. Quantitative stress analysis of recrystallized OFHC Cu subject to deformation in situ. *Journal of Engineering Materials and Technology*, 130(2):021021, 2008.
- [7] J.V. Bernier, M.P Miller, and D.E. Boyce. A novel optimization-based pole figure inversion method: Comparison with WIMV and maximum entropy methods. *Journal of Applied Crystallography*, 39:697–713, 2006.

- [8] D. E. Boyce. Odfpf software package.
<http://anisotropy.mae.cornell.edu/onr/Matlab/matlab.html>.
- [9] D. W. Brown, M. A. M. Bourke, C. N. Tomé, R. Varma, T. M. Holden, and B. Clausen. A neutron diffraction and modeling study of uniaxial deformation in polycrystalline beryllium. *Metallurgical and Materials Transactions A*, 34(7):1439–1449, 2003.
- [10] D.W. Brown, S.R. Agnew, M.A.M. Bourke, T.M. Holden, S.C. Vogel, and C.N. Tomé. Internal strain and texture evolution during deformation twinning in magnesium. *Materials Science and Engineering: A*, 399(1-2):1 – 12, 2005. Measurement and Interpretation of Internal/Residual Stresses.
- [11] H. J. Bunge. The harmonic method. In H. R. Wenk, editor, *Preferred Orientation in Deformed Metals and Rocks: An Introduction to Modern Texture Analysis*, chapter 5, pages 109–122. Academic Press, Inc., Orlando, FL, 1985.
- [12] B. Clausen, T. Lorentzen, M. A. M. Bourke, and M. R. Daymond. Lattice strain evolution during uniaxial tensile loading of stainless steel. *Materials Science and Engineering A*, 259(1):17 – 24, 1999.
- [13] B. Clausen, T. Lorentzen, and T. Leffers. Self-consistent modelling of the plastic deformation of f.c.c. polycrystals and its implications for diffraction measurements of internal stresses. *Acta Materialia*, 46(9):3087 – 3098, 1998.
- [14] Robert D. Cook, David S. Malkus, Michael E. Plesha, and Robert J. Witt. *Concepts and Applications of Finite Element Analysis*. John Wile and Sons, Inc., 4th edition, 2002.
- [15] M. Croft, I. Zakharchenko, Z. Zhong, Y. Gurlak, J. Hastings, J. Hu, R. Holtz, M. DaSilva, and T. Tsakalakos. Strain field and scattered intensity pro-

- filing with energy dispersive x-ray scattering. *Journal of Applied Physics*, 92(1):578–586, 2002.
- [16] M. Croft, Z. Zhong, N. Jisrawi, I. Zakharchenko, R.L. Holtz, J. Skaritka, T. Fast, K. Sadananda, M. Lakshmipathy, and T. Tsakalakos. Strain profiling of fatigue crack overload effects using energy dispersive x-ray diffraction. *International Journal of Fatigue*, 27(10-12):1408 – 1419, 2005. Fatigue Damage of Structural Materials V.
- [17] B.D. Cullity and S. R. Stock. *Elements of X-ray Diffraction*, page 93. Prentice Hall, USA, 3rd edition, 2001.
- [18] P. Dawson, D. Boyce, S. MacEwen, and R. Rogge. On the influence of crystal elastic moduli on computed lattice strains in AA5182 following plastic straining. *Materials Science and Engineering A*, 313(1–2):123 – 144, 2001.
- [19] P. R. Dawson, D. Boyce, S. MacEwen, and R. Rogge. Residual strains in HY100 polycrystals: Comparisons of experiments and simulations. *Metallurgical and Materials Transactions: A Physical Metallurgy and Materials Science*, 31(6), 2000.
- [20] P. R. Dawson, D. E. Boyce, S. R. MacEwen, and R. B. Rogge. On the influence of crystal elastic moduli on computed lattice strains in AA-5182 following plastic straining. *Materials Science and Engineering A*, 313(1-2):123–144, 2001.
- [21] P. R. Dawson, D. E. Boyce, and R. B. Rogge. Issues in modeling heterogeneous deformations in polycrystalline metals using multiscale approaches. *CMES*, 10(2):123–141, 2005.

- [22] Mark R. Daymond and Neil W. Bonner. Lattice strain evolution in IMI 834 under applied stress. *Materials Science and Engineering A*, 340(1-2):272 – 280, 2003.
- [23] M.R. Daymond and H.G. Priesmeyer. Elastoplastic deformation of ferritic steel and cementite studied by neutron diffraction and self-consistent modelling. *Acta Materialia*, 50:1613–1626, 2002.
- [24] Jay L. Devore. *Probability and Statistics for Engineering and the Sciences*. Duxbury, 5 edition, 2000.
- [25] Patrick F Dunn. *Measurement and Data Analysis for Engineering and Science*. CRC Press, 2 edition, 2010.
- [26] C. Efstathiou, D.E. Boyce, J.-S. Park, U. Lienert, P.R. Dawson, and M.P. Miller. A method for measuring single crystal elastic moduli using high energy x-ray diffraction and a crystal-based finite element model. *Acta Metallurgica et Materialia*, In Press, 2010.
- [27] F.C. Frank. Orientation mapping. In J.S. Kallend and G. Gottstein, editors, *Eighth International Conference on Textures of Materials*. The Metallurgical Society, 1988.
- [28] T. P. Gabb, J. Gayda, J. Telesman, P. T. Kantzos, and J. D. Miller. Versatile turbine disk alloy designed and processed for higher temperature applications. In *Research and Technology*, page 13. Glenn Research Center at Lewis Field, 2002.
- [29] A. Hammersley. The fit2d home page.
<http://www.esrf.eu/computing/scientific/FIT2D/>

- [30] Tong-Seok Han and P. R. Dawson. Lattice strain partitioning in a two-phase alloy and its redistribution upon yielding. *Materials Science and Engineering: A*, 405(1-2):18 – 33, 2005.
- [31] M. Haque and M. Saif. A review of mems-based microscale and nanoscale tensile and bending testing. *Experimental Mechanics*, 43(3):248–255, 09 2003.
- [32] A. Heinz and P. Neumann. Representation of orientation and disorientation data for cubic, hexagonal, tetragonal and orthorhombic crystals. *Acta Crystallographica Section A*, 47(6):780–789, Nov 1991.
- [33] K.J. Hemker and W.N. Sharpe. Microscale Characterization of Mechanical Properties. *Annual Review of Materials Research*, 37(1):93–126, 2007.
- [34] W. F. Hosford. *The Mechanics of Crystals and Textured Polycrystals*. Oxford Science Publications, 1993.
- [35] Charles Kittel. *Introduction to Solid State Physics*. John Wiley and Sons, Inc., 2005.
- [36] U. F. Kocks, G. R. Canova, and J. J. Jonas. Yield vectors in f.c.c. crystals. *Acta Metallurgica*, 31(8):1243–1252, 1983.
- [37] U.F. Kocks, C.N. Tome, and H.-R. Wenk. *Texture and Anisotropy*. Cambridge University Press, Cambridge, UK, 1998.
- [38] A. M. Korsunsky, K. E. James, and M. R. Daymond. Intergranular stresses in polycrystalline fatigue: diffraction measurement and self-consistent modelling. *Engineering Fracture Mechanics*, 71(4-6):805–812, 2004.
- [39] A. Kumar and P. R. Dawson. Computational modeling of f.c.c. deformation textures over rodrigues' space. *Acta Materialia*, 48(10):2719 – 2736, 2000.

- [40] John H. Lee, C. Can Aydiner, Jonathan Almer, Joel Bernier, Karena W. Chapman, Peter J. Chupas, Dean Haeffner, Ken Kump, Peter L. Lee, Ulrich Lienert, Antonino Miceli, and German Vera. Synchrotron applications of an amorphous silicon flat-panel detector. *Journal of Synchrotron Radiation*, 15(5):477–488, Sep 2008.
- [41] U. Lienert, M.C. Brandes, J.V. Bernier, J. Weiss, S.D. Shastri, M.J. Mills, and M.P. Miller. In situ single-grain peak profile measurements on ti-7al during tensile deformation. *Materials Science and Engineering: A*, 524(1-2):46 – 54, 2009.
- [42] U. Lienert, T.-S. Han, J. Almer, P.R. Dawson, T. Leffers, L. Margulies, S.F. Nielsen, H.F. Poulsen, and S. Schmidt. Investigating the effect of grain interaction during plastic deformation of copper. *Acta Materialia*, 52(15):4461 – 4467, 2004.
- [43] Ivan Lonardelli, Hans-Rudolf Wenk, Luca Lutterotti, and Mark Goodwin. Texture analysis from synchrotron diffraction images with the Rietveld method: dinosaur tendon and salmon scale. *Journal of Synchrotron Radiation*, 12(3):354–360, May 2005.
- [44] Luca Lutterotti, S Matthies, and Hans-Rudolf Wenk. Maud (material analysis using diffraction): a user friendly java program for rietveld texture analysis and more. In *Proceeding of the Twelfth International Conference on Textures of Materials (ICOTOM-12)*, volume 1, page 1599, 1999.
- [45] L. Margulies, T. Lorentzen, H. F. Poulsen, and T. Leffers. Strain tensor development in a single grain in the bulk of a polycrystal under loading. *Acta Materialia*, 50(7):1771 – 1779, 2002.

- [46] E. B. Marin and P. R. Dawson. Elastoplastic finite element analyses of metal deformations using polycrystal constitutive models. *Computer Methods in Applied Mechanics and Engineering*, 165(1-4):23–41, 1998.
- [47] E. B. Marin and P. R. Dawson. On modelling the elasto-viscoplastic response of metals using polycrystal plasticity. *Computer Methods in Applied Mechanics and Engineering*, 165(1-4):1–21, 1998.
- [48] M. P. Miller, J. V. Bernier, J.-S. Park, and A. Kazimirov. Experimental measurement of lattice strain pole figures using synchrotron x rays. *Review of Scientific Instruments*, 76(11):113903, 2005.
- [49] M.P. Miller, J.-S. Park, P. R. Dawson, and T.-S. Han. Measuring and modeling distributions of stress state in deforming polycrystals. *Acta Materialia*, 56(15):3927 – 3939, 2008.
- [50] A. Morawiec and D. P. Field. Rodrigues parameterization for orientation and misorientation distributions. *Philosophical Magazine A*, 73(4):1113–1130, 1996.
- [51] J.-S. Park, P. Revesz, A. Kazimirov, and M. P. Miller. A methodology for measuring in situ lattice strain of bulk polycrystalline material under cyclic load. *Review of Scientific Instruments*, 78(2):023910, 2007.
- [52] H. Poulsen. *Three-Dimensional X-Ray Diffraction Microscopy*. Springer, Heidelberg, U.K., 2004.
- [53] Hadas Ritz, P. R. Dawson, and Tito Marin. Analyzing the orientation dependence of stresses in polycrystals using vertices of the single crystal yield surface and crystallographic fibers of orientation space. *Journal of the Mechanics and Physics of Solids*, 2009.

- [54] J.S. Robach, I.M. Robertson, B.D. Wirth, and A. Arsenlis. In-situ transmission electron microscopy observations and molecular dynamics simulations of dislocation–defect interactions in ion-irradiated copper. *Philosophical Magazine*, 83(8):955, 2003.
- [55] J. C. Schuren and M. P. Miller. Quantifying the uncertainty of synchrotron-based lattice strain measurements. *Submitted to JSA*, 2010.
- [56] J. C. Schuren, M. P. Miller, and A. Kazimirov. A mechanical testing capability for measuring the microscale deformation behavior of structural materials. *Submitted to: Experimental Mechanics*, 2010.
- [57] J. C. Schuren, S. Watts J. S. Park, and M. P. Miller. A system for measuring crystal level stresses in deforming polycrystals. In *Proceedings of the 2007 SEM Annual Conference and Exposition on Experimental and Applied Mechanics*, volume 82, page 4, Bethel, CT, 2007.
- [58] W. Sharpe, K. Turner, and R. Edwards. Tensile testing of polysilicon. *Experimental Mechanics*, 39(3):162–170, 09 1999.
- [59] E.P.S. Tan and C.T. Lim. Mechanical characterization of nanofibers - a review. *Composites Science and Technology*, 66(9):1102 – 1111, 2006. Nanocomposites.
- [60] H. S. Turkmen, P. R. Dawson, and M. P. Miller. The evolution of crystalline stresses of a polycrystalline metal during cyclic loading. *Int. J. Plast.*, 18:941–969, 2001.
- [61] Michael Uchic, Paul Shade, and Dennis Dimiduk. Micro-compression testing of fcc metals: A selected overview of experiments and simulations.

- JOM Journal of the Minerals, Metals and Materials Society*, 61(3):36–41, 03 2009.
- [62] Michael D. Uchic, Dennis M. Dimiduk, Jeffrey N. Florando, and William D. Nix. Sample dimensions influence strength and crystal plasticity. *Science*, 305(5686):986–989, 2004.
- [63] X.-L. Wang, Y. D. Wang, and J. W. Richardson. Experimental error caused by sample displacement in time-of-flight neutron diffractometry. *Journal of Applied Crystallography*, 35(5):533–537, Oct 2002.
- [64] X.-L. Wang, Y.D. Wang, A.D. Stoica, D.J. Horton, H. Tian, P.K. Liaw, H. Choo, J.W. Richardson, and E. Maxey. Inter- and intragranular stresses in cyclically-deformed 316 stainless steel. *Materials Science and Engineering: A*, 399(1-2):114 – 119, 2005. Measurement and Interpretation of Internal/Residual Stresses.
- [65] Y. D. Wang, R. Lin Peng, and R. L. McGreevy. A novel method for constructing the mean field of grain-orientation-dependent residual stress. *Philosophical Magazine Letters*, 81(3):153 – 163, 2001.
- [66] Y. D. Wang, X.-L. Wang, A. D. Stoica, J. W. Richardson, and R. Lin Peng. Determination of the stress orientation distribution function using pulsed neutron sources. *Journal of Applied Crystallography*, 36(1):14–22, Feb 2003.
- [67] Y.D. Wang, H. Tian, A. D. Stoica, X.-L. Wang, P. K. Liaw, and J. W. Richardson. The development of grain-orientation-dependent residual stresses in a cyclically deformed alloy. *Nature Materials*, 2:101–106, 2003.
- [68] H.-R. Wenk. *Preferred orientations in deformed metals and rocks: an introduction to modern texture analysis*. Academic Press, Orlando, 1985.

- [69] Herman Winick, editor. *Synchrotron Radiation Sources. A Primer*, volume 1 of *Synchrotron Radiation Techniques and Applications*. World Scientific, 1994.
- [70] S.L. Wong and P.R. Dawson. Influence of directional strength-to-stiffness on the elastic-plastic transition of fcc polycrystals under uniaxial tensile loading. *Acta Materialia*, 58(5):1658 – 1678, 2010.
- [71] S.L. Wong, J.C. Schuren, M.P. Miller, and P.R. Dawson. *Quantifying the evolution of crystal stresses during cyclic loading*. To be submitted, 2010.
- [72] R.A. Young, editor. *The Rietveld Method*, volume 5 of *International Union of Crystallography Monographs on Crystallography*. Oxford University Press, 1995.
- [73] Y. H. Zhao, X. Z. Liao, Z. Jin, R. Z. Valiev, and Y. T. Zhu. Microstructures and mechanical properties of ultrafine grained 7075 Al alloy processed by ecap and their evolutions during annealing. *Acta Materialia*, 52(15):4589 – 4599, 2004.